

DISS. ETH No. 17,460

High-Density Neural Interface and Microhotplate Gas Sensor in CMOS Technology

A dissertation submitted to

ETH ZURICH

for the degree of

DOCTOR OF SCIENCES

presented by

Urs Frey

Dipl. El.-Ing. ETH Zurich, Switzerland

Born May 27th, 1977

Citizen of Basel, Switzerland

accepted on the recommendation of

Prof. Dr. Andreas Hierlemann

Prof. Dr. Ulrich Egert

Prof. Dr. Khalil Najafi

Prof. Dr. Henry Baltes

2007

Copyright ©2007 by Urs Frey, Physical Electronics Laboratory

All rights reserved. No part of this book may be reproduced, stored in a retrieval system, or transmitted, in any form or by any means, electronic, mechanical, photocopying, recording or otherwise, without the prior written permission of the copyright holder.

Cover page: The background image shows a colored SEM of chicken dorsal root ganglion neurons cultured for 2 DIV on the CMOS-based MEA, see also Figure 4.1c on page 31 (photo credit: Klaus Marquardt, EMZ, University of Zurich). The images on the back page are taken from the Major Results Section 1.2 on page 2.

Printed and bound by Reprozentrale Honggerberg, ETH Zurich.

Published by:
Physical Electronics Laboratory, PEL
ETH Zurich
Wolfgang-Pauli-Strasse 16
8093 Zurich
Switzerland

Contents

1	Introduction	1
1.1	Structure of the Dissertation	1
1.2	Major Results	2
I	CMOS-based High-Density Microelectrode Array	5
2	Introduction	7
2.1	Structure	9
3	CMOS High-Density Microelectrode Array	11
3.1	Introduction	12
3.2	System Description	12
3.3	Measurement Setup	22
3.4	Experimental Results	23
3.5	Conclusion	28
4	Recordings from Acute Cerebellar Slices Using a CMOS-based High-density Microelectrode Array	29
4.1	Introduction	30
4.2	Results	32
4.3	Discussion	43
4.4	Methods	45
5	Electrical Properties of Cardiomyocytes	51
5.1	Introduction	52
5.2	Material and methods	54
5.3	Results	59
5.4	Discussion	65

6 Conclusion & Outlook	69
7 HD-MEA Bibliography	71
II Microhotplate Gas Sensor	81
8 Introduction	83
9 A Digital CMOS Architecture for a Microhotplate Array	85
9.1 Introduction	86
9.2 Microhotplate Design	88
9.3 Integrated Gas Sensor System	89
9.4 Measurement Results	95
9.5 Conclusion	104
10 Outlook	105
11 Microhotplate Bibliography	107
Appendix	109
A Glossary	109
B Publications	111
C Acknowledgements	115
D Curriculum Vitae	118

Abstract

This thesis presents mixed-signal circuit design, system integration and experimental results of two complementary-metal-oxide-semiconductor (CMOS)-based microsensor arrays: a high-density (HD) microelectrode array (MEA), used to interface with neuronal cells, and a microhotplate-based gas sensor system.

The CMOS-based HD-MEA for bidirectional interaction with neuronal cells was designed with the aim to achieve a high spatial resolution while maintaining a high signal-to-noise ratio (SNR). To this end, a reconfigurable analog switch-matrix was implemented that allows for simultaneous recording from an almost arbitrary subset of 126 electrodes out of 11,011 electrodes in an array with an electrode density of 3,150 electrodes/mm². In contrast to other approaches, that scan the entire array, this approach enables low-noise signal amplification and filtering with the front-end circuitry placed outside the array. The readout channels with two amplification stages limit the bandwidth to between 0.3 Hz and 4 kHz and achieve a noise level of 2.4 μV_{rms} (1 Hz-100 kHz). The data are sampled by on-chip analog-to-digital converters with 20 kSamples/s per channels and transmitted off chip through a digital interface, which was designed to reduce the complexity at the board level while providing a reliable communication.

A custom-designed printed-circuit board (PCB) was built that provides sockets for five HD-MEAs that can be operated simultaneously. The data from the five devices are multiplexed to a single LVDS twisted-pair cable and sent to a field-programmable gate array (FPGA) board at a rate of 16 MB/s. The FPGA provides data processing features, such as CRC error detection, digital filtering, event detection and data reduction/compression before the data are sent to a PC for visualization, analysis and storage.

The software to handle the switch matrix and the large amount of data recorded was developed. A spike-sorting algorithm was implemented that exploits the high spatial density of the electrodes relying on independent-component-analysis (ICA) techniques.

Data recorded with the HD-MEA from more than 100 cultures with rat cardiomyocytes have been analyzed to conduct a study on pharmacological effects on the electrical properties of these cells.

The HD-MEA has been used to record activity from neuronal cells in acute rat cerebellum slices. The shape of the extracellular action potentials was revealed by applying the developed spike sorter. The action potential distribution was in good correlation with the anatomical arrangement of Purkinje cells in the cerebellum. The recorded extracellular action potentials included a wealth of information on subcellular dynamics. To better understand the recorded data, biophysically realistic compartment-model simulations of Purkinje cells have been carried out, which were in good agreement with the recorded data.

The CMOS-based microhotplate gas sensor system comprised an array of three metal-oxide-coated microhotplates with integrated MOS transistor heaters and the needed driving and signal-conditioning circuitry. Three digital PID controllers enabled individual temperature regulation for each hotplate. The operating temperature of the SnO₂ metal-oxide sensors may amount up to 350°C. A serial interface and the temperature control units have been digitally implemented. With its small overall size of 5.5×4.5 mm², its digital interface and its good hotplate thermal efficiency of 6°C/mW, the system represents a significant development on the way to low-cost mobile gas sensor systems. The limit of detection at constant temperature has been assessed to be below 1 ppm for CO and approximately 100 ppm for CH₄. The mainly digital implementation offers the advantage to apply temperature modulation techniques to enhance the analyte discrimination capability.

Zusammenfassung

Die vorliegende Arbeit enthält analogen und digitalen Schaltungsentwurf, Systemintegration und experimentelle Resultate zweier CMOS-Mikrosensorsysteme: (a) einer Mikroelektrodenanordnung mit hoher räumlicher Auflösung zur Kommunikation mit Nervenzellen und (b) eines Gassensorsystems.

Das CMOS basierte Mikroelektrodenarray (CMOS-MEA) ist geeignet für eine bidirektionale Kommunikation mit Nervenzellen und wurde mit dem Ziel entwickelt, einerseits eine hohe räumliche Auslösung zu erreichen und gleichzeitig Messungen mit hohem Rauschabstand durchzuführen zu können. Deshalb wurde eine konfigurierbare Schaltermatrix entworfen, mithilfe derer sich 126 frei wählbare Elektroden aus insgesamt 11 011 Elektroden in einer Anordnung mit einer Dichte von 3 150 Elektroden/mm² gleichzeitig ansteuern lassen. Im Gegensatz zu anderen Ansätzen, bei denen alle Elektroden des Arrays gleichzeitig ausgelesen werden, erlaubt der hier gewählte Ansatz, auch grossere Eingangsstufen mit tiefem Rauschen zu implementieren, da diese ausserhalb der Elektrodenanordnung platziert werden können. Die eingesetzten Ausleseverstärker begrenzen die Bandbreite der Signale zwischen 0.3 Hz und 4 kHz und erreichen einen Eingangsräuschpegel von 2.4 μV_{rms} (Bandbreite: 1 Hz-100 kHz). Die Signale werden auf dem Chip mit 20 kHz/Kanal abgetastet und digitalisiert. Die digitale Schnittstelle, die die Daten weiterleitet, wurde darauf ausgelegt eine möglichst einfache Anbindung des Chips an externe Komponenten zu ermöglichen, und gleichzeitig die Integrität der Daten zu gewährleisten.

Ausserdem wurde ein Messsystem entwickelt, das gleichzeitig fünf CMOS-MEAs ansteuern kann. Die Daten von allen fünf CMOS-MEAs werden auf einer einzigen LVDS Leitung gebündelt und mit einer Datenrate von 16 MB/s an ein FPGA geschickt. Auf dem FPGA werden die Daten dann weiter prozessiert, Übertragungsfehler werden ermittelt, Ereignisse in den Signalen gesucht, und die Datenmenge wird reduziert und komprimiert. Zur weiteren Verarbeitung, Visualisierung, und Speicherung werden die Daten zu einem PC übertragen.

Zur Ansteuerung der konfigurierbaren Schaltermatrix und zur Verarbeitung der grossen Datenmenge wurde spezielle Software entwickelt. Zudem wurde Software zur Klassifizierung der extrazellulär gemessenen neuronalen Aktionspotentiale, die auf der Methode der Independent Component Analysis (ICA) basiert, entwickelt.

In einer ersten Anwendung wurden die elektrischen Eigenschaften von Herzmuskelzellen von Ratten in über hundert Zellkulturen analysiert, um die Effekte diverser, pharmakologisch aktiver Substanzen zu untersuchen.

Zudem wurden die CMOS-MEAs dazu eingesetzt, die Aktivität von Nervenzellen in akuten Schnitten des Kleinhirns von Ratten zu messen. Mit der entwickelten Software zur Klassifizierung der entsprechenden Signale konnte die Verteilung und Form der extrazellulären Aktionspotentiale hochaufgelöst dargestellt werden. Die Resultate spiegelten die anatomische Anordnung der Purkinjezellen im

Kleinhirn wider. Die Details und Auflösung der aufgezeichneten Daten beinhalten umfassende Information über subzelluläre Abläufe in den Purkinjezellen. Um die Daten besser verstehen zu können, wurden Simulationen mit einem biophysikalisch realistischen Kompartimentmodell durchgeführt. Es ergab sich eine sehr gute Übereinstimmung zwischen gemessenen Daten und Simulation.

Das Gassensorsystem basiert auf einem Array von drei mit Metalloxid beschichteten Mikroheizplatten und wurde in CMOS Technologie gefertigt. Die Temperatur auf den Mikroheizplatten wird mit Hilfe von Temperatursensoren, drei PID Reglern und drei transistorbasierten Heizern kontrolliert. Die mögliche Betriebstemperatur der sensitiven SnO_2 Schichten reicht von Raumtemperatur bis 350C. Die Temperaturregler und die serielle Schnittstelle zum Mikrochip wurden in digitaler Schaltungstechnik realisiert. Durch die kleine Systemgröße, die digitale Ansteuerung und den guten thermischen Wirkungsgrad der Heizplatten von 6C/mW kann das Sensorsystem auch in mobilen oder batteriebetriebenen Geräten eingesetzt werden. Die Nachweisgrenze beträgt 1 ppm für Kohlenmonoxid und rund 100 ppm für Methan, wenn das System bei konstanter Temperatur betrieben wird. Zur Verbesserung der Diskriminierung verschiedener Analyten erlaubt die grösstenteils digitale Systemimplementierung eine individuelle Temperaturmodulation auf jeder Heizplatte.

Chapter 1

Introduction

This thesis describes two sensor array systems co-integrated with dedicated circuitry in CMOS-technology. Both systems feature highly specialized circuitry to drive and readout the sensors, together with elaborate post-CMOS processing to fabricate the sensors.

The microhotplate-based gas sensor array requires sophisticated micromachining in order to realize the membrane structures including the transistor-based heaters, temperature sensors and interface contacts to the sensing material. Co-integration with driving and sensing circuitry leads to a very compact system.

The post-CMOS processing for the microelectrode array requires fewer steps, however, achieving long-term biocompatibility is none-the less challenging. For this device, co-integration has the immediate advantage that it allows to overcome the interconnection limitation found in passive devices, and therefore allows for sensor arrays with performances not otherwise possible.

1.1 Structure of the Dissertation

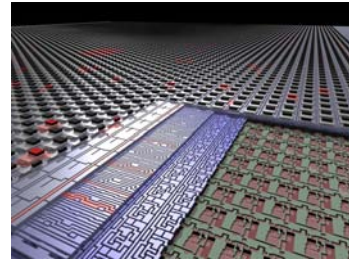
The core of this *paper dissertation* consists of a selection of four publications, three of which are related to the CMOS-based microelectrode array, and one of which describe the CMOS-based microhotplate gas sensor device. Therefore, the thesis is structured into two parts:

- High-Density Microelectrode Array, Part I
- Microhotplate Gas Sensor, Part II

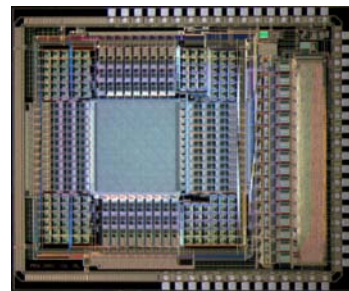
The major fraction of the thesis is on the CMOS microelectrode array, in accordance with the time and efforts spent on the projects. Both parts feature separate introductions, conclusions, and bibliographies.

1.2 Major Results

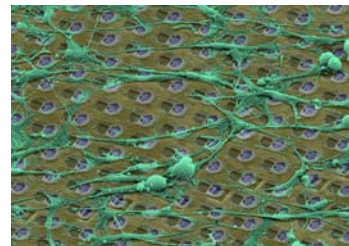
Analog Switch Matrix for Sensor Readout. Achieving, at the same time, a high spatial and temporal resolution in recording from large sensor arrays is a major challenge. The approach selected here includes to readout a subset of electrodes with low-noise amplifiers placed outside the array and to provide a highly flexible routing with a reconfigurable switch matrix (Chapter 3.2.1 on page 14).



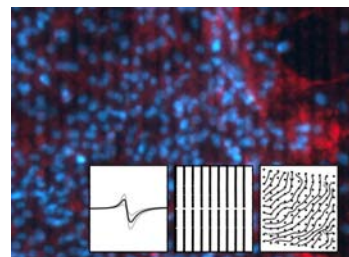
CMOS-based HD-MEA. The high-density microelectrode array was integrated with recording and stimulation circuitry, AD converters and a digital interface fabricated in industrial 0.6 μm CMOS-technology with additional post-CMOS processing steps to achieve biocompatibility (Chapter 3 on page 11).

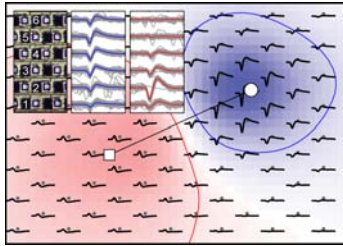


Dissociated Neuronal Cultures. Dissociated chicken and rat neuronal cells have been successfully cultured. Measurements after 16 DIV from hippocampal rat neurons have been successfully conducted (Figure 4.10 on page 44).

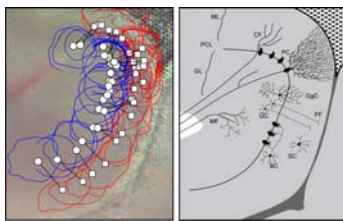


Neonatal Rat Cardiomyocytes. Data analysis for recordings from NRCs was fully automated to enable experiments for targetting the modulation of electrical properties of cultured NRCs. Results from more than 100 cultures demonstrate the reliability and usability of the technology in conducting biological, and pharmacological experiments (Chapter 5 on page 51).

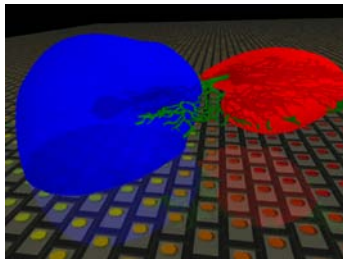




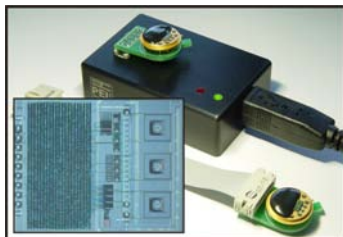
ICA-based Spike Sorter. Neural recordings at high spatiotemporal resolution open new possibilities for spike sorting. An ICA-based spike sorter has been developed and tested using artificially generated data. The algorithm has also been applied to real data and helped to reveal distinct features of extracellular action potentials (Section 4.4.4 on page 46).



Recordings from Acute Brain Slices. Signals from acute cerebellar slice preparations have been recorded. Single units could be separated from the multiunit recordings. The shape and distribution of the recorded extracellular fields could be correlated to the orientation of Purkinje cells in the cerebellum (Chapter 4 on page 29).



Validation against a Purkinje Cell Compartment Model. The recorded data have been compared to simulation results of a detailed, biophysically realistic compartment model. The results show a good agreement between experimental and modeling results. The device offers the potential to record neuronal dynamics at a subcellular level (Section 4.2.2 on page 38).



CMOS-based Microhotplate-based Gas Sensors. A monolithically integrated microhotplate gas sensor array with transistor heaters, and interface electronics has been developed. Measurements of CO and CH₄ have been conducted using temperature modulation techniques (Chapter 9 on page 85).

Part I

CMOS-based High-Density Microelectrode Array

Chapter 2

Introduction

This part of the thesis includes the design, fabrication and application of a high-density (HD) microelectrode array (MEA) implemented in complementary metal-oxide semiconductor (CMOS) technology. MEAs are arrangements of usually 60 electrodes that are used for multisite extracellular recordings from electrogenic cells such as neurons, heart cells, retinal cells or muscle cells. They are used in the fields of neuroscience and biosensing to study fundamentals of learning processes, aging and mental diseases, or to assess the behavior of electrogenic cells *in vitro*¹ [Marom and Shahaf, 2002, Jimbo and Robinson, 2000, Wagenaar et al., 2006a], for screening of pharmacological agents [Gross et al., 1995, Fennrich et al., 1996, Stenger et al., 2001, Meyer et al., 2004], or for the detection of hazardous substances [Kovacs, 2003].

Even though early publications on MEAs date back already several decades [Thomas et al., 1972], the field of MEAs is still growing and new applications are emerging. MEAs have become commercially available just within the last decade². However, software tools that are able to handle the vast amount of data obtained from such devices and that are easy to use and can be customized for different experiments are still largely lacking. For a summary of *in vitro* and *in situ*³ applications of MEAs, see Stett et al. [Stett et al., 2003b].

The use of CMOS-based devices can overcome some limitations of passive MEAs, such as performing measurements at a high spatial and temporal resolution, as will be shown in Chapter 3.

Developing a CMOS-based MEA also means developing a complete system in an interdisciplinary field. It is not about obtaining another incremental improvement of an already highly optimized system, it is more about realizing novel

¹*In vitro* (Latin: within glass), means outside a living organism, as opposed to *in vivo* (Latin: within the living).

²For example: multichannelsystems GmbH, Germany, www.multichannelsystems.com; Panasonic, Japan, www.med64.com; Plexon Inc., USA, www.plexoninc.com.

³*In situ* (Latin: in the place), which in biology usually means somewhere between *in vivo* and *in vitro*.

complex systems. The major challenge is to combine knowledge from different fields such as mixed-signal circuit design, software engineering, micromachining and packaging while keeping the biological application in mind.

A large fraction of this part of the thesis (and the efforts during the dissertation) is focused on applications of the HD-MEA. The power of the technology and its advantages for measuring biologically relevant data that are difficult (or impossible) to obtain otherwise are demonstrated (Chapter 4). Moreover, by showing a larger study with more than 100 cultures of cardiomyocytes the reliability, applicability and usability of the developed technology for biological experiments is demonstrated (Chapter 5).

The core team in the project, which was partially founded by an ETH-internal grant⁴, included:

- Frauke Greve and Donat Scheiwiler: post-CMOS processing.
- Jan Šedivý: Measurement setup.
- Carlota Diaz Sanchez-Bustamante: NRC experiments.
- Urs Frey: Device concept, design, testing, software, measurements and data analysis.

The project was started on the basis of the already very evolved INPRO⁵ project, the major contributors of which include Flavio Heer, Sadik Hafizović and Wendy Franks. For more details, refer to their dissertations [[Heer, 2005](#), [Hafizovic, 2006a](#), [Franks, 2005](#)].

⁴ETH-internal grant TH-1-03-1

⁵European IST-FET program, contract number IST-2000-26463.

2.1 Structure

The following part consists of three papers:

1. *CMOS High-Density Microelectrode Array*
U. Frey, F. Heer, J. Sedivy, S. Hafizovic, K.-U. Kirstein, and A. Hierlemann
in preparation, (Chapter 3)
2. *Recordings from Acute Cerebellar Slices with a CMOS-based Microelectrode Array*
U. Frey, U. Egert, F. Heer, S. Hafizovic, and A. Hierlemann
in preparation, (Chapter 4)
3. *Modulation of Electrical Properties of Cardiomyocytes by Regulated BMP-2 Expression*
C.D. Sanchez-Bustamante, U. Frey, J.M. Kelm, A. Hierlemann, and M. Fussenegger
Tissue Engineering, 2008, in publication, (Chapter 5)

The first paper focuses on the CMOS-based microelectrode array. It introduces the reconfigurable switch matrix implemented on the device, which is crucial for enabling low-noise recordings while ensuring a high spatial and temporal resolution. The paper then describes the circuitry implemented on the device, and shows the measurement setup used to interface with the device. The second paper shows recordings from acute cerebellar slices. It highlights the possibilities that the device offers in, e.g., observing subcellular dynamics of Purkinje cells. The recorded data are compared to a compartment model and demonstrates the spatial resolution that is required to sample the full signal dynamics. The third section presents a short version of a paper originating from a collaboration with C.D. Sanchez-Bustamante⁶. It is a study about using lentivirus-derived particles to regulate the gene expression to modulate the electrophysiological characteristics of cardiomyocytes. The contribution of the Physical Electronics Laboratory in this study included rendering the devices available, performing the data analysis and preparing most of the figures. Additional methods and results can be found in the original paper [Sanchez-Bustamante et al., 2008], which also describes a gaseous acetaldehyde-inducible system and co-cultures of microtissues and monolayer of cardiomyocytes that have been omitted here. Chapter 6 then concludes the CMOS MEA part of the dissertation.

⁶Institute for Chemical and Bio-Engineering, ETH Zurich, Switzerland.

Chapter 3

CMOS High-Density Microelectrode Array

Urs Frey, Jan Sedivy, Flavio Heer, Sadik Hafizovic,
Kay-Uwe Kirstein, and Andreas Hierlemann

in preparation

Physical Electronics Laboratory, ETH Zurich, Switzerland

Abstract We report on a CMOS-based microelectrode array (MEA) featuring 11,011 metal electrodes and 126 channels, each of which comprises recording and stimulation electronics, for extracellular bidirectional communication with electrogenic cells, such as neurons or cardiomyocytes. The important features include: (i) high spatial resolution at (sub)cellular level with 3,150 electrodes per mm² (electrode diameter 7 μm, electrode pitch 18 μm); (ii) a reconfigurable routing of the recording sites to the 126 channels; and (iii) low noise levels.

3.1 Introduction

Microelectrode arrays (MEA) are an important tool for multisite extracellular recording in the fields of neuroscience and biosensing [Gross et al., 1995, Pine, 1980, Najafi and Wise, 1986]. Conventional and commercially available MEAs are arrangements of usually 60 electrodes with diameters ranging between 10 μm and 30 μm and densities of up to 100 electrodes per mm^2 . It is very appealing to conduct biological or electrophysiological experiments at cellular or subcellular resolution. Neuronal cells range between below 10 μm diameter for vertebrates and up to 100 μm for invertebrates in size. Three different approaches to achieve cellular resolution have been realized so far: (i) constraining the cells with regard to the electrode positions [Rutten, 2002, Zeck and Fromherz, 2001], (ii) adapting the electrode layout to the biological structure [Gholmieh et al., 2006] or (iii) using high-density arrays that record from all electrodes simultaneously [Eversmann et al., 2003a, Berdondini et al., 2005]. The high-density arrays are usually CMOS-based devices that overcome the interconnect limitation by making use of on-chip signal multiplexing. The simultaneous recording from all electrodes requires the front-end amplifiers to be placed in each pixel (recording site), which, due to area constraints, entails rather high noise levels. Instead of scanning the entire electrode array, the approach presented here provides a reconfigurable electrode/readout-channel routing to select an arbitrary subset of electrodes for recording and stimulation. This enables both, low-noise signal recording, and cellular or subcellular resolution, since the front-end circuitry can be placed outside the array (Figure 3.1), where sufficient area for a low-noise circuit implementation is available.

The paper is organized as follows: Section 3.2 describes the implementation of the microsensor, Section 3.3 details the measurement setup to operate the chip, Section 3.4 includes experimental results, and Section 3.5 concludes the paper.

3.2 System Description

The 126 channels providing signal amplification and stimulation are located outside the reconfigurable electrode array, as depicted in the block diagram in Figure 3.2. The electrode array with the implemented switch matrix is described in Section 3.2.1. The block of the readout and stimulation channels includes two amplification and filter stages. They are implemented with Miller-compensated 2-stage amplifiers, which are detailed in Section 3.2.2 and Section 3.2.3. Both stages feature digitally configurable gain and filter settings. The first stage provides a high-pass filter (HPF), a low-pass filter (LPF) and a gain of 30 dB. The second stage provides additional gain of either 0 dB, 20 dB or 30 dB with a second LPF. An offset compensation scheme as described in Section 3.2.3 was implemented in this stage. Amplifier settings, such as gain and LPF cut-off, are set to the same values for all channels. Eight channels are then multiplexed and

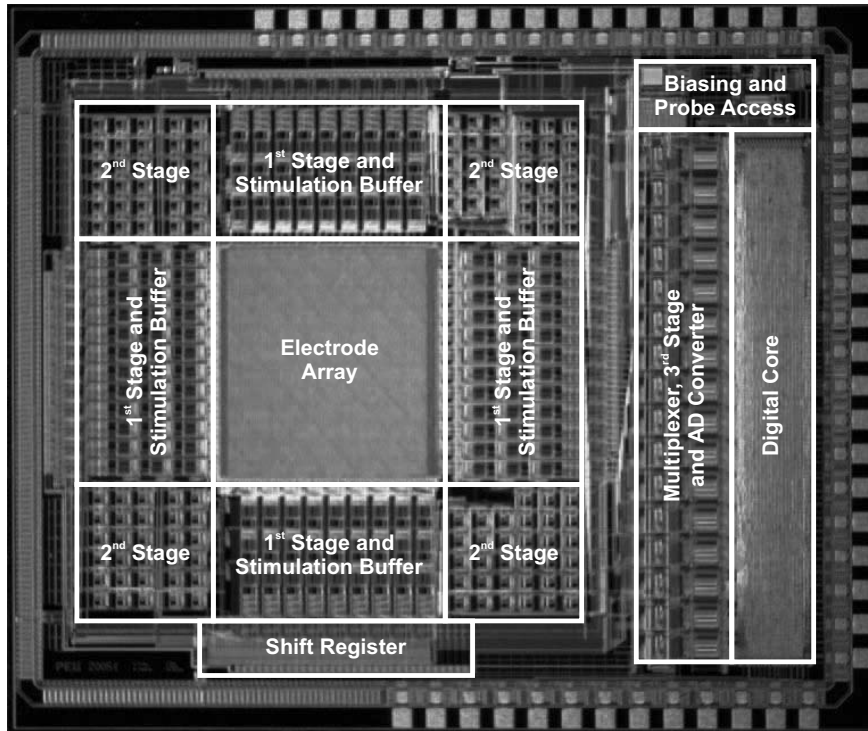


Figure 3.1: Micrograph of the fabricated device.

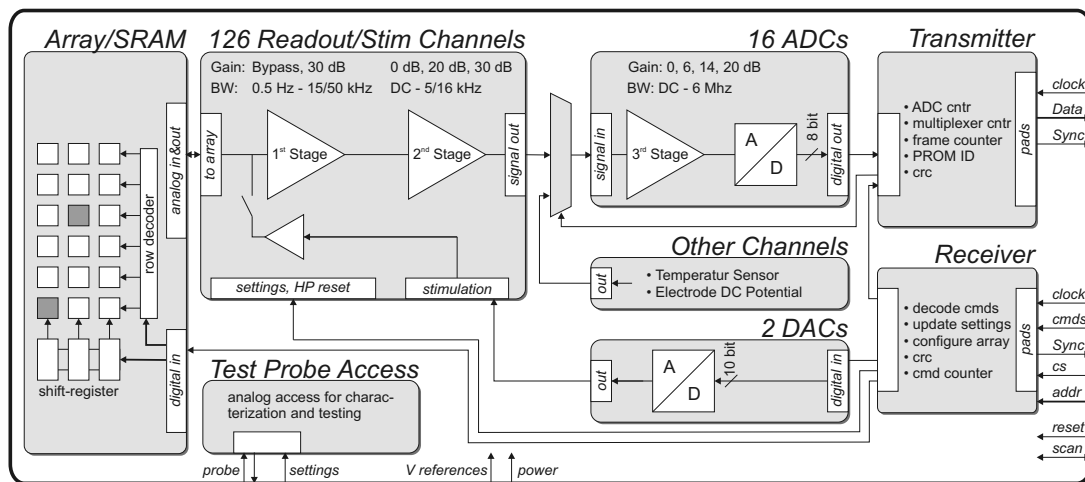


Figure 3.2: Block diagram of the chip architecture and the on-chip electronics.

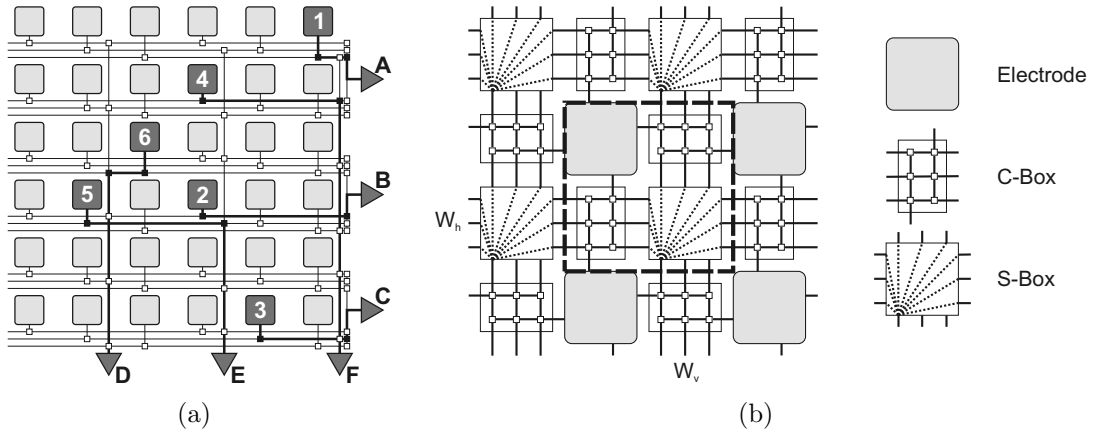


Figure 3.3: Sketch of a reconfigurable switch matrix enabling a flexible subset selection for readout and stimulation. (a) Illustrates the principle of routing a subset of electrodes (1-6) to channels (A-F) for readout and stimulation. (b) Shows a general implementation of a pixel (illustrated with the dashed line) within such an array (the implemented switch matrix is drastically simplified, see Figure 3.4).

buffered by a third stage with an additional gain of 0 dB, 6 dB, 14 dB or 20 dB, and finally digitized at 20 kHz using successive-approximation (SAR) analog-to-digital converters (ADCs) with a resolution of 8-bit. The digital transmitter then transfers the data off chip on a 9-bit bus together with chip-status information and a CRC (cyclic redundancy check) for error detection, as described in Section 3.2.4. The transmitter also controls the ADCs and the multiplexers. A one-time programmable 16-bit ID was included on the device, that allows for keeping track of the devices and enables automated database access for retrieving device-specific calibrations (such as electrode impedance data), and storing recording protocols. Two additional channels are used to monitor the temperature and the DC potential on a separate electrode.

The receiver and transmitter are implemented in their own clock domains, which allows for a simple interfacing circuitry on the PCB level. The receiver decodes commands that are used to configure the array, to define the amplifier and bias settings, and for stimulation.

The stimulation capability is provided through two 10-bit flash DACs and stimulation buffers, operable in both, voltage and current stimulation mode. Each stimulation buffer can be connected to the two DAC outputs, so that two stimulation patterns can be simultaneously applied on two selectable subsets of electrodes.

3.2.1 Switch Matrix

The flexibility in electrode selection is attained by the use of an analog switch matrix integrated underneath the electrode array. The switch matrix consists of

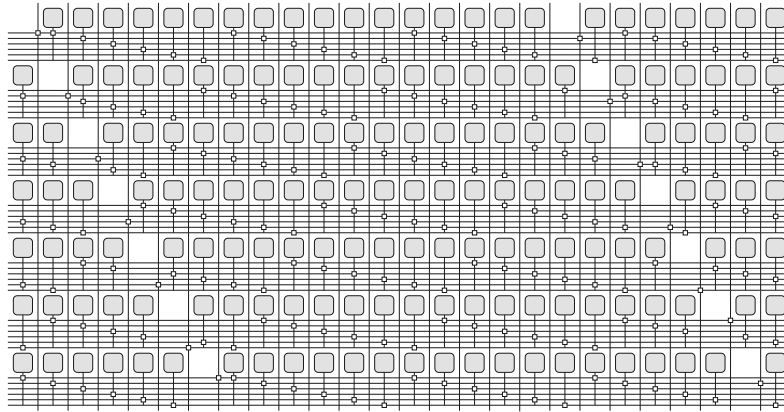


Figure 3.4: Subset of the implemented switch matrix.

13k SRAM cells and analog switches (PMOS, $W/L = 4/0.6$) to define the routing from the electrodes to the amplifiers as illustrated in Figure 3.3a. Figure 3.3b shows a general form of such a switch matrix, which resembles routing schemes of field-programmable gate arrays (FPGAs). The small squares in this figure represent the switches required to connect the electrodes to the wires. Each electrode is connected through connection boxes (C-Boxes) to horizontal (W_h) and vertical (W_v) readout wires. The readout wires are then interconnected by switch boxes (S-Boxes) that contain switches to connect two wires, either a horizontal to a horizontal, a vertical to a vertical or a horizontal to a vertical wire. Wires can also go through the S-Box without being interrupted by a switch.

The memory bits that drive the switches are located within the array and are implemented as standard 6T-SRAM cells, made of minimum-size transistors. An SRAM cell has the advantage of very small power consumption in static mode, thereby reducing the power dissipation within the array to a minimum. The feature size of the CMOS technology used for the fabrication of the device ($0.6 \mu\text{m}$) and the constraints on the pixel area limited the number of switches within each pixel to one. As at least one C-Box with at least one switch is required for each electrode, some electrodes need to be sacrificed for pixels that contain a minimal version of an S-Box without any electrode. However, the resulting holes are covered up by slightly shifting the other electrodes, so that finally the electrodes are evenly distributed (Figure 3.11). The actual wiring is implemented as illustrated in Figure 3.4.

To obtain the configuration for the switches, the switch matrix is represented as a graph, as illustrated in Figure 3.5, and the routing problem is solved. The problem resembles a binary max-flow, min-cost problem, with the interesting spots being the sources and the channels being the sinks. The switch configuration should provide a maximum flow with a minimum cost. However, there are some constraints that set the problem apart from the standard max-flow, min-cost problem and also from constraints normally used in FPGA routing algorithms: one electrode can, e.g., pick up the signal from two (or more) neurons.

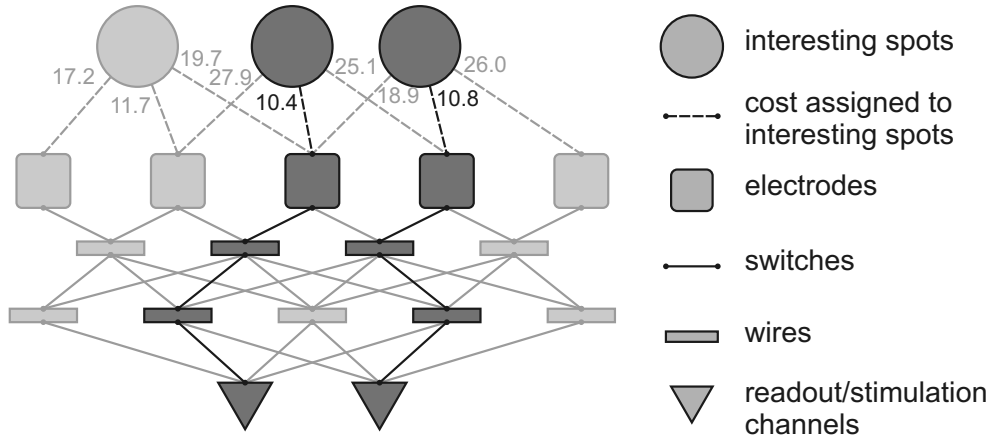


Figure 3.5: Representation as a graph to solve the routing problem.

This means that we have a larger inflow into a node than outflow. To deal with this issue and with other special routing constraints, the optimization problem is solved with a general integer linear program (ILP) solver that permits any linear constraints. The ILP can be written as:

Minimize

$$\mathbf{c}^T \mathbf{x}$$

subject to

$$\mathbf{l} \leq \mathbf{x} \leq \mathbf{u},$$

where \mathbf{x} is a vector of integers to be sought for, \mathbf{c} is the cost vector and \mathbf{l} and \mathbf{u} are vectors of defined lower and upper bounds. For our routing problem, \mathbf{x} represents the state of the switches, i.e., arcs in the graph. The constraint that renders them either open or closed, i.e., binary, is

$$0 \leq x_i \leq 1$$

The constraints for all the different node types shown in Figure 3.5, are:

$$\begin{array}{llll}
 \text{For each neuron :} & \sum \text{outflow} & = & 1 \\
 \text{For each electrode :} & \sum \text{inflow} - \# \text{in arcs} * \sum \text{outflow} & \leq & 0 \\
 & \sum \text{outflow} & \leq & 1 \\
 \text{For each wire :} & \sum \text{inflow} - \sum \text{outflow} & = & 0 \\
 & \sum \text{inflow} & \leq & 1 \\
 & \sum \text{outflow} & \leq & 1 \\
 \text{For each channel :} & 0 \leq \sum \text{inflow} & \leq & 1
 \end{array}$$

Additionally, an excess node is added with arcs from all neurons. Those arcs are assigned a high penalty cost to allow for convergence in the case that a neuron cannot be connected.

The solution of the ILP provides the state of all the switches within the array. The array is programmed row-by-row by serially shifting bits into a shift register located below the electrode array and by then transferring the content to one row of SRAM cells. Some optimizations on the configuration stream are performed in software to reduce its length and thereby the necessary configuration time.

An example of the routing performance is given here. The cost of the first arcs is given as the Euclidian distance from the electrodes to the center of the spots of interest. Simulations have been carried out for routing 126 randomly distributed spots of interest to the 126 channels. The average distance from any spot of interest to the closest electrode was found to be 6.75 μm for the used set (number of simulated experiments: 2000) and provides the lower bound of the achievable routing performance. The implemented routing scheme provides an average distance to the connected electrode of 7.1 μm , whereat 114.6 out of the 126 spots of interest are read out via the closest electrode, 10.1 through the second closest and the remaining 1.3 via the third or fourth closest electrodes. 102 electrodes in a 6×17 rectangular configuration constitute the largest obtainable coherent electrode block.

3.2.2 Front-end Amplifier

Offset and drift that occur at the electrode can significantly exceed the signal amplitude. Offsets of up to 1 V and drifts in the electrode potential of 100 mV within a few seconds have been measured [Heer et al., 2006a]. For this reason, a HPF, with a cut-off frequency below 1 Hz has been used in the first stage, as shown in Figure 3.6. As the wiring within the electrode array is single-ended, the amplifier was also implemented in a single-ended way with a pseudo-differential input stage.

The gain of the first stage is 30 dB and is defined by the capacitance ratio C_1/C_2 . The value of C_2 represents a tradeoff between gain accuracy, corner frequency and area. A value for C_2 of 150 fF was chosen, leading to a total area of $150 \times 280 \mu\text{m}^2$ for the first stage. The cut-off frequency of the first-order HPF is given by the capacitance C_2 and the resistive part of the feedback, which is implemented with two diode-connected transistors D_1 and D_2 [Najafi and Wise, 1986, Delbruck and Mead, 1994, Harrison and Charles, 2003]. To achieve a low cut-off frequency, the resistance must be large; therefore, the transistor is of minimum width. In order to reduce substrate leakage currents, the length was also kept small (1 μm). To improve the symmetry of the structure and to get a more linear behavior for small values of V_D , a second diode was added in reverse direction yielding better defined values of R even for $V_D < 0$. This structure results in a cut-off frequency of below 1 Hz.

The opamp used in the first stage was implemented with a two-stage amplifier with a differential input stage and a common-source output stage. M_1 and M_2 are operated in weak inversion:

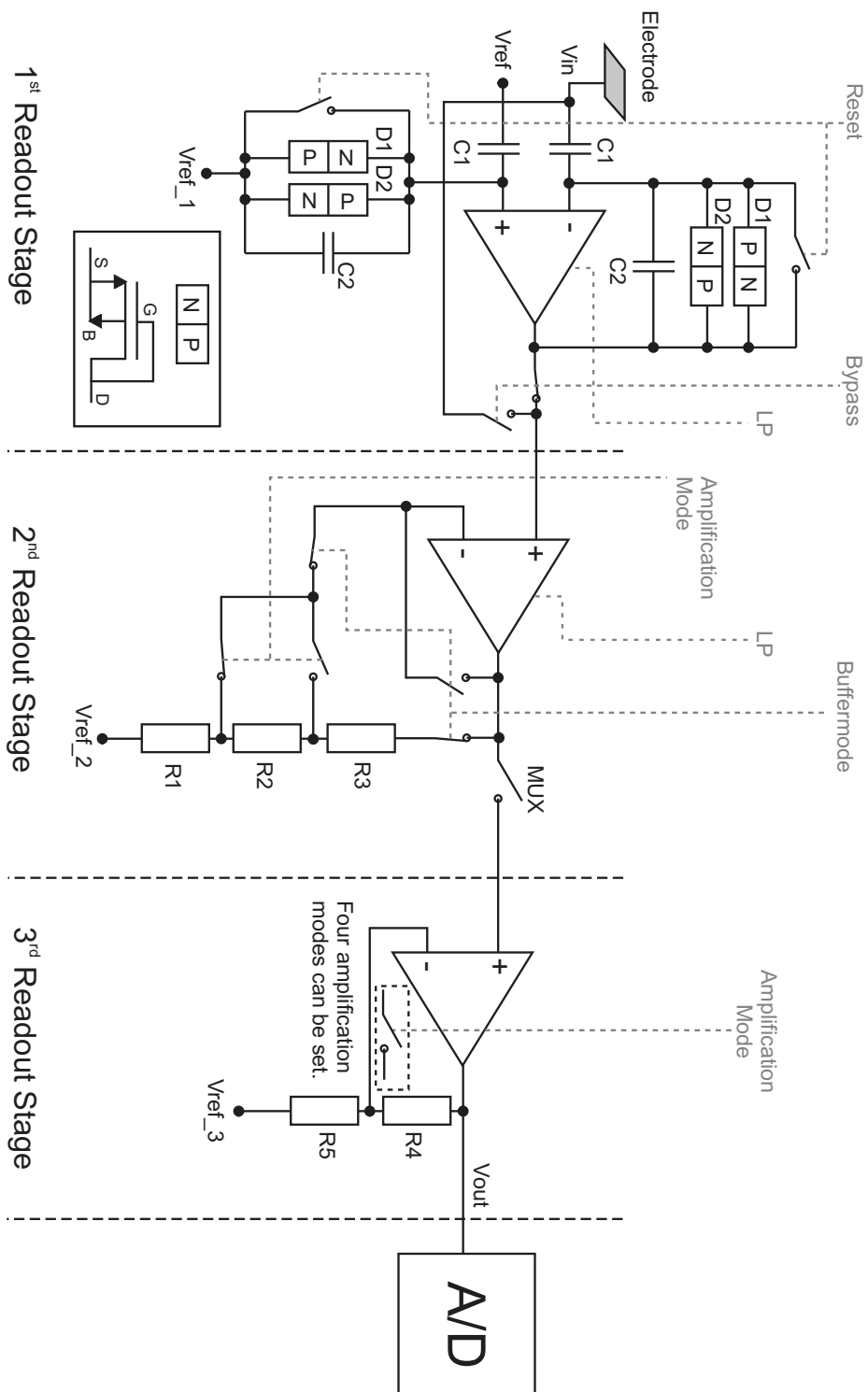


Figure 3.6: Amplification stages of the readout channels, with the first stage featuring a low HPF cut-off frequency.

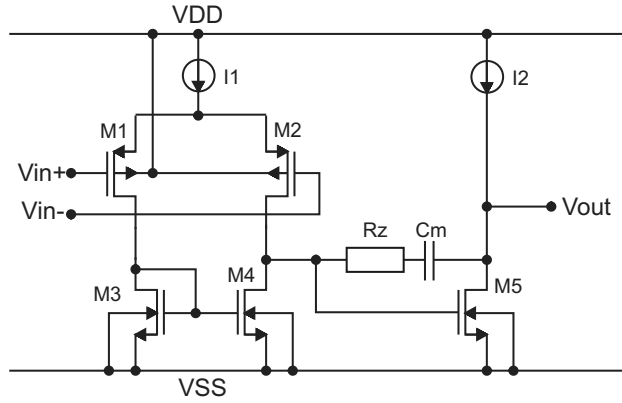


Figure 3.7: Miller-compensated two-stage opamp used in the first stage.

$$g_m = \frac{I_D}{nV_{th}}.$$

The other transistors are operated with $V_{DSAT} = V_{GS} - V_{th} > 200$ mV and therefore:

$$g_m = \sqrt{2k' \frac{W}{L} I_D}.$$

For noise considerations, the transistors $M_{1..4}$ have to be considered. The equivalent input noise of a differential input stage is

$$\overline{v_{eqT}^2} = \overline{v_{eq1}^2} + \overline{v_{eq2}^2} + \left(\frac{g_{m3}}{g_{m1}}\right)^2 (\overline{v_{eq3}^2} + \overline{v_{eq4}^2}),$$

which shows that the influence of M_3 and M_4 is smaller, if the ratio of $\frac{g_{m3}}{g_{m1}}$ is small. For a good tradeoff between low noise and small area the terms $\overline{v_{eq1}^2}$, $\overline{v_{eq2}^2}$ should be roughly equal to the term $\left(\frac{g_{m3}}{g_{m1}}\right)^2 (\overline{v_{eq3}^2} + \overline{v_{eq4}^2})$. Additionally, a tradeoff between the thermal- and the $1/f$ -noise must be made. The $1/f$ -noise depends on the area of the transistor

$$\overline{v_{1/f}^2} = \frac{K_f \Delta f}{C_{ox} W L f},$$

and does not depend on the bias current. A larger area of the transistor cannot be achieved by increasing L , as this would lower $g_m \sim \sqrt{W/L}$, which results in larger thermal noise. The thermal noise is given by

$$\overline{v_{th}^2} = 4kT \left(\frac{2}{3g_m}\right)^2 \Delta f.$$

The thermal noise is dominant in the 5-kHz signal band. A larger bias current will decrease the thermal noise, as $g_m \sim \sqrt{I_D}$, but it will also increase the power

consumption and compromise stability. The transistor size of M_1 , M_2 was chosen as 360/2 and that of M_3 , M_4 as 10/30, with a bias current of $I_1=2.7 \mu\text{A}$ and $I_2=16.4 \mu\text{A}$. The simulated noise level then results in $3.2 \mu\text{V}_{rms}$ (output noise divided by the midband gain).

The LPF cut-off, f_{LP} , is realized using the Miller capacitance C_M . The gain-bandwidth product of the opamp is

$$GBW = \frac{g_m}{C_M} = A \cdot f_{LP},$$

with g_m being the transconductance of the first stage and A the gain. The Miller capacitance is implemented as a 1.8 pF capacitor and a second capacitor (4.8 pF) that can be switched on and off, which produces an LPF cut-off frequency of ~ 15 kHz or ~ 50 kHz. The exact value depends on the bias current, which, in turn, can be digitally adjusted at the chip level. A zeroing resistor was included to improve the stability, with a value of $R_z = \frac{1}{g_{m5}}=7.7$ k Ω . Additionally, the first stage can be bypassed, which provides a useful means to test features in DC mode, such as the array routing wires, the DACs and the ADCs.

3.2.3 Second Stage and Offset Compensation

The second amplification stage is a non-inverting amplifier also implemented as a two-stage Miller compensated opamp. The adjustable gain of either 0 dB, 20 dB or 30 dB is achieved by switching between different resistors R_1 , R_2 and R_3 in the feedback, as shown in Figure 3.6. An LPF with a cut-off of ~ 5 kHz or ~ 16 kHz is implemented in the same way as in the first stage. This stage also contains an offset compensation mechanism. It is implemented by making the width of the current mirror transistor M_4 digitally adjustable (5 bits), as shown in Figure 3.8. The length of the current mirror transistors M_3 , M_4 and $MS_{4..0}$ is 12 μm , M_3 has a width of 28.8 μm , M_4 of 19.2 μm and $MS_{4..0}$ feature values of 12.8 μm , 6.4 μm , 3.2 μm , 1.6 μm and 0.8 μm . An input offset of ± 55 mV can be compensated in steps of 5 mV or less.

3.2.4 Digital Part

The digital part is split into two clock domains, one for the transmitter side, which also controls the ADCs and the multiplexers, and another one for the receiver side, which decodes and executes configuration commands.

The 16 ADCs in the transmitter part run at a clock frequency of 3.2 MHz, and need 10 clock cycles for one conversion at an 8-bit resolution. One frame of output data consists of 160 bytes, 128 of which are used for the ADC data. The additional frames are used to transmit status information about the device,

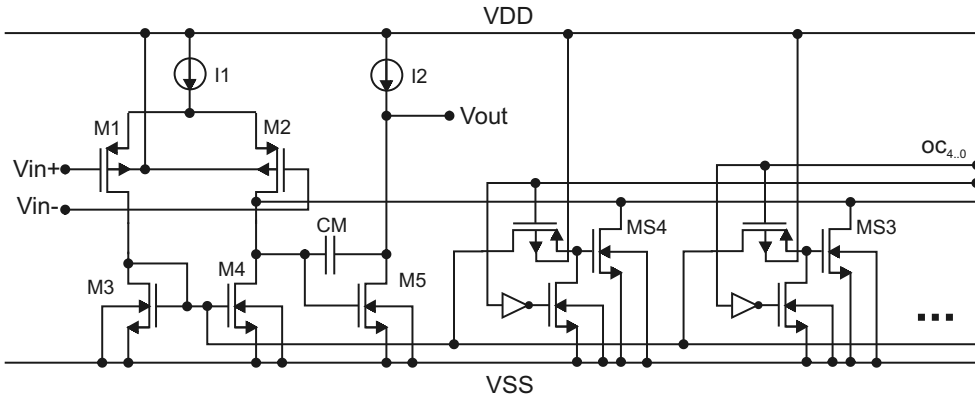


Figure 3.8: Second amplifier stage with offset compensation.

such as the multiplexer settings, the DAC values and amplifier settings. Additionally, the chip address, a 16-bit frame counter and the command counter are inserted. A CRC (CRC-16/CITT) used for error detection concludes the frame. For convenience, an additional pad is used to send frame synchronization pulses.

On the receiver side, the commands are received as a bitstream, clocked in by the separate receiver clock. The commands are in the following format:

	Chip Address				Cmd Length				Cmd			Data			CRC			
1	a_3	a_2	a_1	a_0	l_3	l_2	l_1	l_0	c_2	c_1	c_0	d_{n-1}	...	d_0	r_3	r_2	r_1	r_0

A command starts with a start-bit, followed by the chip address, the length of the command in nibbles, the command, the command arguments and it ends with a CRC (CCITT-4). A command is only executed, if the chip address is matched or if the chip address is the broadcast address 0xF and when no CRC error is detected. Upon each successful command execution, the command counter is incremented. The command counter is implemented as a Gray counter, which simplifies the synchronization between the receiver and transmitter clock domain. Commands are used to program the on-chip PROM ID, to configure the switch matrix, to define the amplifier settings (gain, LPF, biasing), to set the multiplexer switching scheme, to set the stimulation DACs, to adjust the DC-offset compensation FFs, to configure the stimulation buffers, and to execute the HPF reset.

Before executing any commands, the receiver checks the integrity of the received commands by means of the CRC. It also increments a command counter on successful execution of commands. The command counter is then transmitted off chip, providing a means to track the chip status.

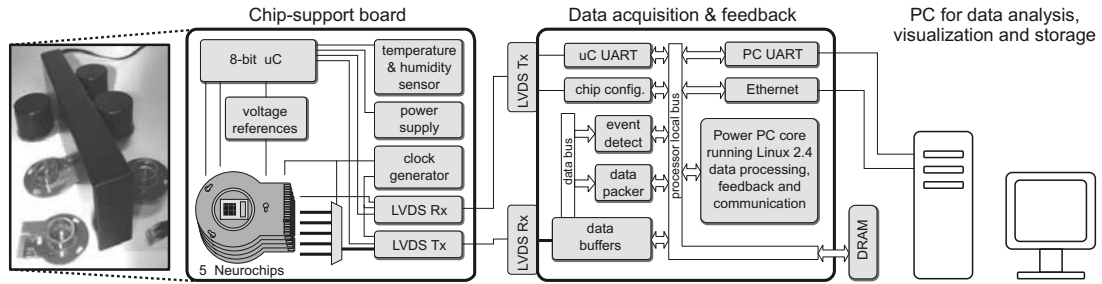


Figure 3.9: Block diagram of the system. On the left side a photograph of the support board with plugged-in chips is shown.

3.3 Measurement Setup

The system as depicted in Figure 3.9 consists of three main blocks. A custom-designed PCB was built that provides sockets for five HD-MEAs that can be operated simultaneously. It is essential to avoid mechanical perturbation by handling devices with plated cells prior to measurements so that a multichip setup has been developed [Wagenaar et al., 2006a]. The board provides all necessary clock and digital control signals, as well as all required analog references to the chips. The value of the references can be programmed using the on-board microprocessor. This processor also monitors the environmental conditions (temperature and humidity). To minimize the amount of required connections, the data are serialized on the board and sent via two twisted-pair links at 16 MB/s. By using a serial LVDS protocol, a 6-wire ribbon cable is sufficient to connect the board with the rest of the system.

The main data acquisition and feedback control unit is realized using the platform Xilinx Virtex II Pro FPGA. This component features fast data-processing algorithms implemented on the programmable logic and also hosts two PowerPC cores, both capable of running a Linux operating system with clock frequencies up to 300 MHz. The data are converted back to a parallel representation, the data streams from the different chips are separated, and a CRC check is performed. The extracted data are then distributed via an internal data bus to the data processing units, e.g., compression and spike-detection units. These units use direct memory access (DMA) to write the results into the system memory DRAM, where they can be accessed from applications running on the PowerPC. As the chips produce large amounts of data, which need to be stored for later processing, a compression block was designed. It is a lossless compression that encodes the difference between two data points in time using Rice coding [Rice, 1979] with an adaptive algorithm to update the compression parameters depending on the measured signal properties. The application program running on the PowerPC core is responsible for the data transport between the FPGA core and the supervising computer.

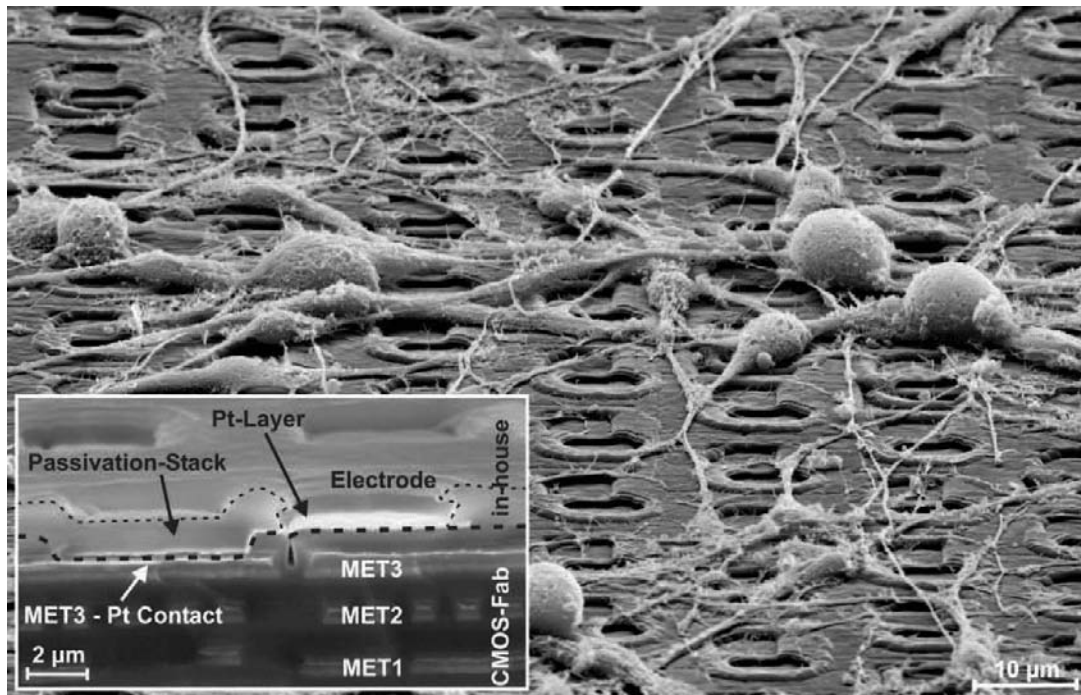


Figure 3.10: Chicken dorsal root ganglion neurons on a high-density microelectrode array and chip cross section.

The third component is the software running on the PC. It consists of a server application and several clients connected to the server. As HD-MEAs have a complex structure with an electrode routing matrix and a programmable gain, the server implements five chip-emulator modules. Every time the real chip configuration is changed, the same changes are applied to the corresponding emulators. The client applications can then retrieve the currently connected electrodes, gain and filter settings from the emulators.

All communication links from the chip to the PC are protected by CRCs in either direction, allowing for error detection and thereby ensuring data integrity.

3.4 Experimental Results

3.4.1 Fabrication

The chip was fabricated in an industrial $0.6\ \mu\text{m}$ 3-metal, 2-polysilicon CMOS-process. A micrograph of the device is shown in Figure 3.1. The total device size is $7.5 \times 6.1\ \text{mm}^2$, and the electrode array covers an area of $2.0 \times 1.75\ \text{mm}^2$. Special post-CMOS processing and packaging steps are required to render the chip capable of operating in physiological solution with cell cultures on top. The 2-mask post-processing step includes sputtering Ti:W (20 nm) and platinum (200 nm) as electrode materials and patterning of the metals with the help of a lift-off process.

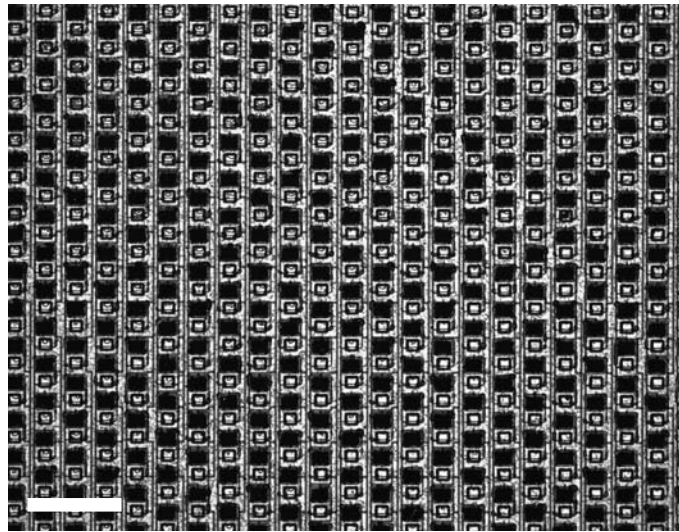


Figure 3.11: Uniform electrochemically grown Pt-Black. Scale bar: 50 μm

Thereafter a 1.6- μm -thick passivation layer stack (SiO_2 and Si_3N_4) is deposited for corrosion protection [Heer et al., 2006a]. The Pt electrode openings are shifted away from the locations of the original CMOS aluminum contacts to ensure long-term stability. Together with the electrodes an integrated on-chip Pt-electrode is fabricated that can be used as a reference in measurements. It is placed around the electrode array and has a total area of roughly 0.6 mm^2 . Figure 3.10 shows the fabricated chip, on which chicken dorsal root ganglion neurons have been cultured for 2 days *in vitro* (DIV). The inset illustrates the post-processing steps with the shifted-electrode design. This 2-mask post-CMOS processing sequence yielded good results and chips being operable for several weeks. During long term culturing of several months, however, it was found that the areas, where the thick insulating passivation stack has been opened to access the Pt electrodes are the weak spots in the overall protection, since the CMOS foundry passivation is the only protection there. Therefore the post-processing was changed to a 3-mask sequence with the first and additional step being a deposition of 500 nm Si_3N_4 to increase the thickness of the bottom passivation (not shown in Figure 3.10).

To reduce the electrode impedance, Pt-black can be electrochemically deposited on the electrodes, using 1.0 nA/m^2 current density in a solution containing 7 mM hexachloroplatinic acid, 0.3 mM lead acetate, and hydrochloric acid to adjust the solution pH to 1. A platinum wire was used as a counter electrode, connected to an external current source, and the on-chip stimulation circuitry was used to set the electrode to a defined potential. A uniform platinization could be obtained as it is shown in Figure 3.11.

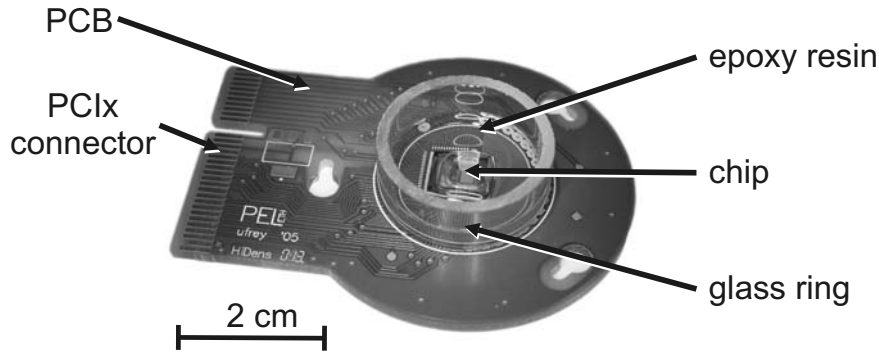


Figure 3.12: Packaged device.

3.4.2 Packaging

To allow for culturing of cells, the chips have been packaged as illustrated in Figure 3.12. The processed chip is mounted and wire-bonded on a custom-designed printed-circuit board (PCB) with an electroplated nickel/gold edge-connector. A glass ring is then glued on the PCB, and a water-resistant medical epoxy (EPOTEK 302-3M), is used to encapsulate the bond wires and the pads.

3.4.3 Electrical Characterization

The measured transfer function of the readout channels is shown in Figure 3.13, measured for a gain of 1,000 and the lowest possible LPF cut-off frequency. The bottom part shows the noise spectrum using the same settings for three different cases: (i) the amplifiers with shorted inputs ($2.4 \mu\text{V}_{rms}$ output noise from 1 Hz to 100 kHz, divided by the midband gain), (ii) use of bare Pt-electrodes ($3.9 \mu\text{V}_{rms}$) and (iii) use of dendritic Pt-black electrodes ($3.0 \mu\text{V}_{rms}$) in saline solution. Compared to [Heer et al., 2006a], the noise has been reduced by 10 dB, which is mainly due to the use of the diodes, $D_{1,2}$, and the relaxed area constraints (i.e., larger input transistors). The ADC contributes 0.5 LSB quantization noise. Worst-case signal crosstalk within the array (2 mm long, parallel readout wires with minimum spacing) was assessed to be 67 dB in a saline solution using Pt-black electrodes. The standard deviation of the input-referred offset is 0.7 mV (version 1). The overall chip power consumption is 135 mW, 115 mW of which are consumed by the third stage, the ADCs and the digital core located more than 2 mm away from the array (Figure 3.1). The power dissipation within the array itself is negligible. One readout channel (stage 1, 2) consumes $160 \mu\text{W}$ in an area of 0.07 mm^2 .

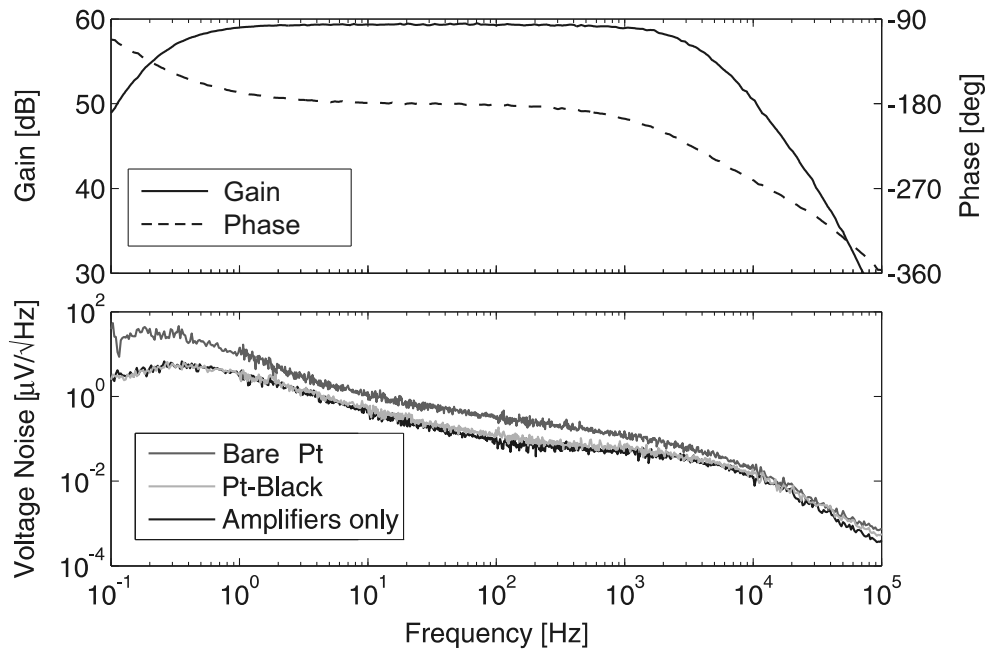


Figure 3.13: Measured transfer function of the three amplifier stages for a gain of 1,000 and the lowest possible LPF cut-off settings. The bottom part shows the input-referred noise spectrum for the same settings.

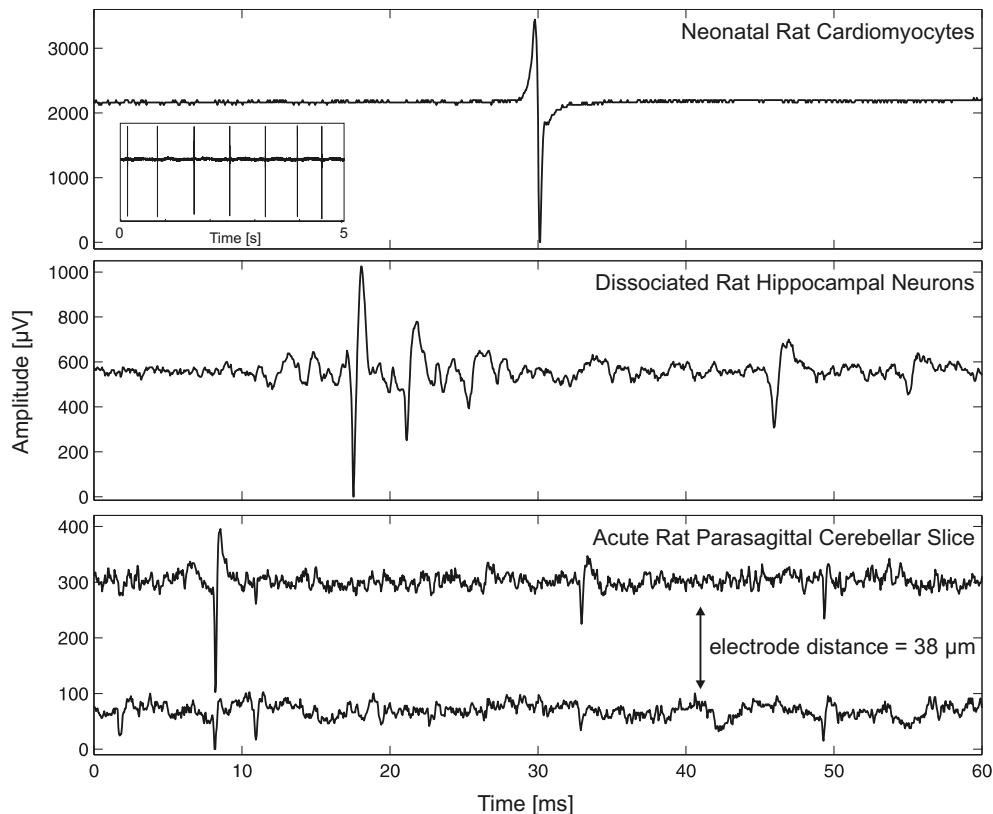


Figure 3.14: Electrophysiological signals obtained from different biological preparations.

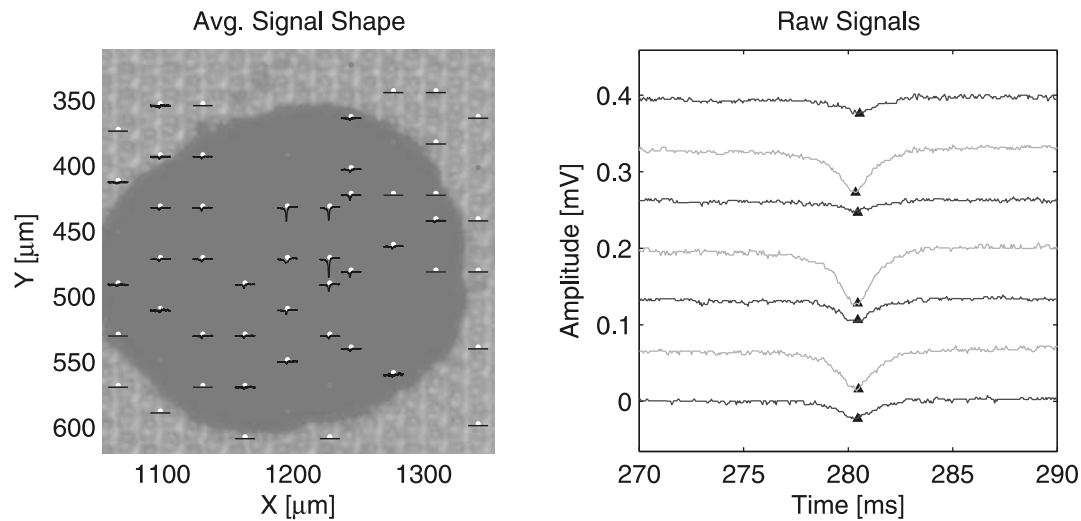


Figure 3.15: The left panel shows a microtissue that was derived from neonatal rat cardiomyocytes placed on the HD-MEA. Overlaid are the measured signal shapes. In the right panel, the raw signal traces are shown for seven selected electrodes. The triangles mark the detected peaks.

3.4.4 Electrophysiological Measurements

Figure 3.14 shows spontaneous electrical activity in several biological preparations as recorded using the HD-MEA to illustrate the broad applicability of the microsystem. The top trace was obtained from neonatal rat cardiomyocytes (3 DIV). The middle trace stems from dissociated rat hippocampal neurons cultured for 16 DIV. The two traces at the bottom show recordings with spike activity from acute brain slices (parasagittal slice of the cerebellum of a Long-Evans rat). The preparation was performed at room temperature, as described in [Egert et al., 2002]. Oxygen was supplied through a perfusion system containing artificial cerebrospinal fluid. The on-chip counter electrode was used as a reference for recording. The two exemplary recordings shown here are from electrodes located at a distance of $38\ \mu\text{m}$. Action potentials of single cells are visible on several neighboring electrodes.

Figure 3.15 shows neonatal rat cardiomyocyte (NRC)-derived microtissues. In order to enable gravity-mediated microtissue production in hanging drops [Kelm et al., 2003, 2004c], isolated monodispersed NRCs were seeded at 2,500 cells/well into 60-well plates and cultivated with plating media (67% DMEM, 17% M199, 10% horse serum, 5% fetal bovine serum and 1% penicillin/streptomycin solution) for 4 days. After four days, the resulting myocardial microtissues were placed onto the microelectrode array previously coated with $20\ \mu\text{g}/\text{mL}$ laminin. Within six hours, the NRC microtissues attached to the surface of the chip, and recordings from the NRCs embedded in a three-dimensional artificial tissue were performed after the addition of $10^{-2}\ \text{mM}$ phenylephrine. The microtissues did not need to be precisely positioned, as there is a large area covered with elec-

Table 3.1: Performance summary

Technology	0.6 μm 3M2P CMOS
Area	$7.5 \times 6.1 \text{ mm}^2$
Supply voltage analog	5.0 V
Supply voltage digital	3.3 V
Clock frequency transmitter	3.2 MHz
Clock frequency receiver	8 MHz
Number of electrodes	11,011
Sensor area	$2.0 \times 1.75 \text{ mm}^2$
Electrode density	3,150 1/ mm^2
Power consumption overall	135 mW
Power consumption front-end (stage 1&2)	160 μW /channel
Front-end input-referred noise (1 Hz to 100 kHz)	2.4 μV_{rms}
Amplification	0-80 dB (18 steps)

trodes. The signal quality is very good, and the output noise divided by the midband gain in this measurement is 2.3 μV_{rms} (incl. quantization noise, digital HP at 10 Hz). Such low noise levels are only achievable, if there is no significant background activity. Signals around 10 μV are detectable.

3.5 Conclusion

A system to record extracellular activity from electrogenic cells in culture or tissue at high spatial and temporal resolution has been presented. The high-density microelectrode array has been fabricated in CMOS technology combined with additional post-CMOS processing steps. The device enables the simultaneous recording from and stimulation of 126 electrodes selected out of 11k electrodes. The implemented reconfigurable switch matrix provides a high degree of flexibility in the electrode selection and allows for low-noise amplifier implementations outside the array. A system for data acquisition has been developed. The functionality of the overall system has been verified with electrical tests and measurements in biological preparations. A summary of the main parameters of the microsystem is given in Table 3.1.

Acknowledgment

The authors would like to thank R. Pedron, M. Ballini, S. Senn and S. Berg for contributing to the circuit and system design. F. Greve and D. Scheiwiller for help with the post processing, Dr. U. Egert, C. D. Sanchez-Bustamante, E. Perriard, T. Neumann, Dr. A. Blau, Dr. B. Roscic for help with the biological measurements, the EMZ at the University Zurich for providing Figure 3.10.

Chapter 4

Recordings from Acute Cerebellar Slices Using a CMOS-based High-density Microelectrode Array

Urs Frey¹, Ulrich Egert^{2,3}, Flavio Heer¹, Sadik Hafizovic¹,
and Andreas Hierlemann¹

*in preparation*¹

¹ETH Zurich, Department of Biosystems, Science and Engineering,
Mattenstrasse 26, 4058 Basel, Switzerland

²Bernstein Center for Computational Neuroscience Freiburg,
Neurobiology & Biophysics, Faculty of Biology,

Albert-Ludwigs-University, Hansastr. 9a, 79104 Freiburg, Germany

³current address: Biomicrotechnology, Faculty of Applied Sciences,
Albert-Ludwigs-University, Hansastr. 9a, 79104 Freiburg, Germany

¹*Correspondence:* should be addressed to U.F. (ufrey@phys.ethz.ch) and U.E. (egert@biologie.uni-freiburg.de).

Author Contributions: U.F. and A.H. developed the device idea. U.F. designed and tested the device, did the measurements and the data analysis, including the modeling. U.E. designed the experiments, performed the slice preparation and contributed to the measurements. F.H. and S.H. contributed to the device. U.F., U.E. and A.H. wrote the manuscript.

Competing interests statement: The authors filed a patent application covering parts of the implemented interface circuitry.

Abstract Simultaneously recorded multiple-neuron action potentials (AP) contain a wealth of information on the dynamics in neuronal networks and on the properties of individual neurons that is difficult to obtain with intracellular recordings. Here, we present a high-density planar microelectrode system (HD-MEA), based on complementary metal-oxidesemiconductor (CMOS) microelectronics technology for in vitro recordings of extracellular potentials at subcellular resolution. From an array of 11,011 microelectrodes (3,150 electrodes per mm^2), 126 electrodes can be arbitrarily selected and can, via a reconfigurable routing scheme, be connected to on-chip recording and stimulation circuits featuring noise-levels of 7-9 $\mu\text{V}_{r.m.s.}$. With this HD-MEA we analyzed the distribution and dynamics of extracellular potentials in the somatic and dendritic compartments of Purkinje Cells (PCs) in acute cerebellar slices. The field structures match those generated by compartmental models of PCs in the recording situation, revealing local current densities and backpropagation of APs into the proximal dendrites.

4.1 Introduction

Mapping the extracellular, spatio-temporal dynamics of neuronal activity in vivo and in vitro has gained considerable interest as new methods for the extraction of information from electrophysiological microelectrode array data become available, e.g., in the context of the development of implanted neuroprosthetic devices. Information acquired through extracellular recordings has enabled the reconstruction of activation sequences in cultured networks, slice preparations and intact brains [Buzsaki, 2004], and it potentially enables the characterization of ion channel properties and ion channel distributions in single cells.

The detailed structure of the extracellular-potential landscape of a neuron, however, is mostly unknown. This prevents an unambiguous reconstruction of neuronal networks as a consequence of the low signal-to-noise ratio and the low spatial resolution in the respective electrical measurements. In particular, spatial undersampling prevents a complete reconstruction of current sink/source distributions. Commercially available planar microelectrode arrays for in vitro experiments [Pine, 1980, Gross et al., 1995] usually comprise ~ 60 electrodes, with diameters up to 30 μm and feature up to 100 electrodes per mm^2 . Optical methods, such as 2-photon microscopy and calcium imaging, provide high spatial resolution (even in 3 dimensions) [Gobel et al., 2007], however, suffer from poor temporal resolution or low signal-to-noise ratio.

HD-MEAs potentially increase the information content of extracellular recordings. HD-MEAs presented so far [Eversmann et al., 2003a, Berdondini et al., 2005], however, suffer from a low signal-to-noise ratio that renders the extracellular detection of spike activity and the decomposition into single-unit signals difficult. These devices record simultaneously from all electrodes, which requires the front-end amplifiers to be located directly at each recording electrode. To achieve high spatial resolution, the space at each electrode is severely constrained, so that high-end signal conditioning units cannot be effectively realized. Instead of scanning the entire 11,011 electrodes of our HD-MEA (electrode density: 3,150

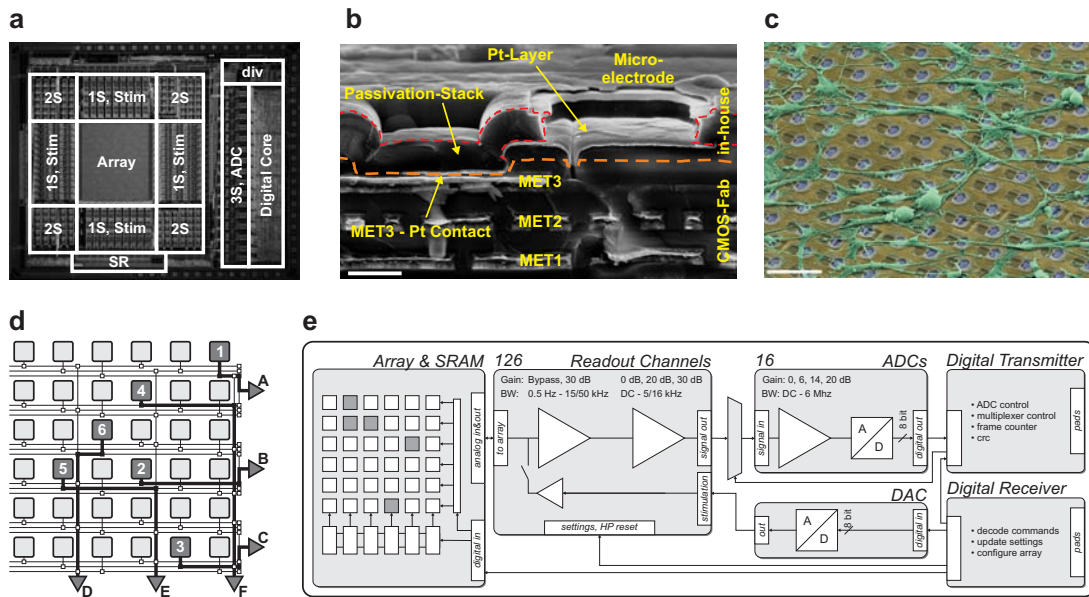


Figure 4.1: CMOS-based microelectrode array: (a) micrograph of the chip ($7.5 \times 6.1 \text{ mm}^2$). The electrode array is surrounded by the two first amplification and filtering stages (1S and 2S) and the stimulation buffers (Stim). Below the array are the shift register (SR) used to program the array and on the right-hand side the third amplifier stages, analog-to-digital converters (3S, ADC) and the digital core. (b) Scanning electron microscope cross-section of the chip showing the post-CMOS processing needed for biocompatibility (scale bar: $2 \mu\text{m}$). (c) Colored Scanning electron micrograph of chicken dorsal root ganglion neurons cultured on the HD-MEA (2 days *in vitro*) illustrating size and density of the microelectrodes (blue) in comparison to the neurons (green); scale bar: $30 \mu\text{m}$. (d) Sketch of the switch matrix for readout and stimulation. The electrodes (1-6) are connected to the amplifiers (A-F) through switches represented as open or filled small squares. (e) Block diagram of the on-chip circuitry.

electrodes/mm²; pitch 18 μm ; electrode diameter 7 μm), we use a reconfigurable routing scheme to connect an arbitrarily selectable subset of 126 electrodes (e.g., cohesive blocks, lines, or selected single electrodes) to recording and stimulation electronics channels. The channel circuitry, in particular the front-end amplifiers, are placed outside of the electrode array, where there is enough space to realize high-performance circuitry in standard CMOS technology (Fig. 4.1), enabling low noise levels between 7 and 9 μV_{rms} . Moreover, a selection approach is reasonable because (i) the signals from HD-MEAs are largely redundant (extracellular potentials of a cell or unit are simultaneously recorded on several neighboring electrodes), (ii) there is usually enough time to sequentially scan different regions of interest (ROIs), (iii) a high percentage of electrodes does often not provide relevant information, and, most importantly, (iv) this approach enables high spatio-temporal resolution, low-noise recordings for a detailed mapping of the extracellular potentials in the ROI.

To illustrate the performance of the developed devices, we analyzed the extracellular potential landscape of PCs in acute slices of the cerebellum. The electrical activity of individual cells was revealed by applying spike sorting and spike-triggered averaging methods to the recorded high-resolution data. The results were compared to a compartmental PC-model to interpret the fine structure of the extracellular APs, i.e. spikes. We show that the recorded spikes include detailed information on the cellular arrangement in the tissue and on the fine structure (subcellular resolution) of the AP dynamics.

4.2 Results

4.2.1 Recordings

Recordings from acute sagittal cerebellar slices were performed as previously described [Egert et al., 2002] to test the performance of the HD-MEA. The PCs are spontaneously active and are effectively disconnected from each other because the parallel fibers have been cut in a sagittal slice. In addition, the excitatory input from the deep cerebellar nuclei via climbing fibers is missing. The PC electrical fields can thus be considered independent from each other, which facilitates spike sorting and eases waveform interpretations.

Spikes in the voltage traces varied considerably in shape, and the signals on neighboring electrodes showed a high degree of synchronicity, which indicates that different neurons contribute to the overall signal on each electrode and that the same neuron provides signals on various electrodes (Fig. 4.2). The spike shape distributions were analyzed using independent component analysis (ICA) to identify and separate spikes originating from different neurons. Spike-triggered averages of the signal on all electrodes in a ROI were calculated for each identified unit, and the potential distribution generated by an individual neuron was analyzed.

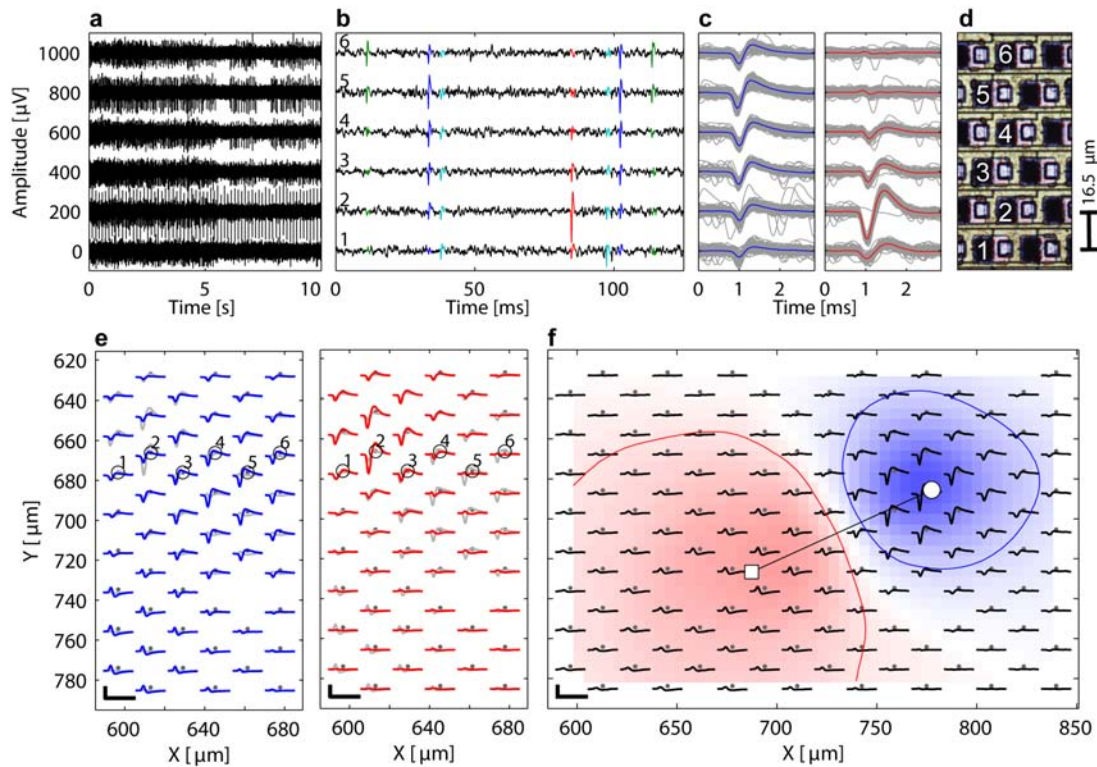


Figure 4.2: Recordings obtained from an acute parasagittal cerebellar slice. Electrical signals from the six neighboring electrodes (black) marked in (d). (a) Spontaneous spike activity. (b) Zoom into (a) with 4 differently shaped spikes identified through spike sorting and marked in color. Each unit is detectable on more than one electrode, but not on all six. (c) Superposition of events of two identified units in (b) within a 30s recording period. The average signal is indicated in color. (e) Average spatial distribution (footprint) of spike-triggered averages of the two neurons in (c); scale bars in (e, f): $100\ \mu\text{V}$, $1.9\ \text{ms}$. (f) Footprint of another cell reconstructed from three blocks of electrodes recorded sequentially at full spatial resolution: Potential distribution at the time of the first negative peak (circle: center of all negative peaks weighted with the peak amplitudes, square: center of all positive peaks). Colored contour lines represent equipotential lines at half peak amplitude, i.e., $-63\ \mu\text{V}$ for the blue line in the negative region (blue), and $+18\ \mu\text{V}$ for the red line in the positive region (red). The footprint reveals distinct spikes over a large area including more than one hundred electrodes; Frequency band: $100\ \text{Hz}$ - $3.5\ \text{kHz}$.

Spike amplitudes ranged from the detection limit ($\sim 35 \mu\text{V}$, $\sim 4\times$ noise level) up to a few $100 \mu\text{V}$, with firing rates of 7-35 Hz. No significant cross correlation of spike trains from neighboring PCs was observed. This fact and the large number of electrodes allowed for an effective application of ICA. The firing rates may be somewhat underestimated, since priority was given to precision over sensitivity during spike sorting in order to obtain accurate cell footprints, i.e., accurate extracellular-potential distributions.

Detectable spike activity was found in the cerebellar cortex only (Fig. 4.3). The rate of supra-threshold events and their amplitude was maximal in the region of the Purkinje cell layer (PCL). Spikes were typically bipolar with large negative peaks in the PCL region, and positive peaks in the molecular layer (ML). Spike shapes at positions in between represent combinations of these basic types. The spatio-temporal characteristics of the potential of a certain PC in the parasagittal slice were that of a dipole with the negative pole at the PCL and the positive pole in the ML during AP onset. During further spike evolution, the soma became more positive, while proximal parts of the dendrites became more negative, and the potential in the distal dendritic tree subsided. The potential distribution at the time of the negative peak (Fig. 4.2f) was used to estimate the orientation of each neuron relative to the device surface (N units = 27, Fig. 4.3b). Evidence suggests that we predominantly recorded from PCs, since we did not identify any units exclusively in the granular cell layer, the ML, or in the white matter. At a threshold value of $-35 \mu\text{V}$, the negative-potential area extended $50\text{-}150 \mu\text{m}$ along the surface of the chip. Its location coincided with that of the PCL and the positive-potential region extended across most of the adjacent ML (Fig. 4.4). In some regions a slight displacement of presumptive PC somata near the chip surface with regard to the PCL visible at the upper surface of the slice was observed, since the slice lays slightly slanted to the sagittal plane.

In a selected slice preparation (Fig. 4.5a-c) we analyzed 41 PCs with somata at an estimated 30 to $90 \mu\text{m}$ distance to the surface that have been identified by the spike sorter. The spikes of 37 PCs out of the total of 41 passed a negative threshold of $-35 \mu\text{V}$ and those were then simultaneously detectable on 25 ± 12 electrodes ($\sim 8000 \mu\text{m}^2$), only spikes of 12 PCs passed the threshold of $+35 \mu\text{V}$ and were detectable on 11 ± 7 electrodes ($\sim 3500 \mu\text{m}^2$ area). The area with amplitudes of at least half the maximum signal heights included 19 ± 8 electrodes ($\sim 6000 \mu\text{m}^2$) for negative signals and 38 ± 37 electrodes ($\sim 13000 \mu\text{m}^2$) for the smaller positive signals.

Figure 4.5 shows recordings from slices that were presumably cut slightly tilted to the sagittal plane. In the slice shown in Figure 4.5a-c, the activity on two adjacent to a fissure was approximately evenly distributed. The slice in Figure 4.5d-f, however, shows rather unevenly distributed electrical activity along a fissure, with higher activity to the right of the fissure. The widespread activity with an event rate below 10 Hz in Figure 4.5d stems from numerous small spikes with mostly positive amplitudes. We assume that the respective slice (Fig. 4.5d-f)

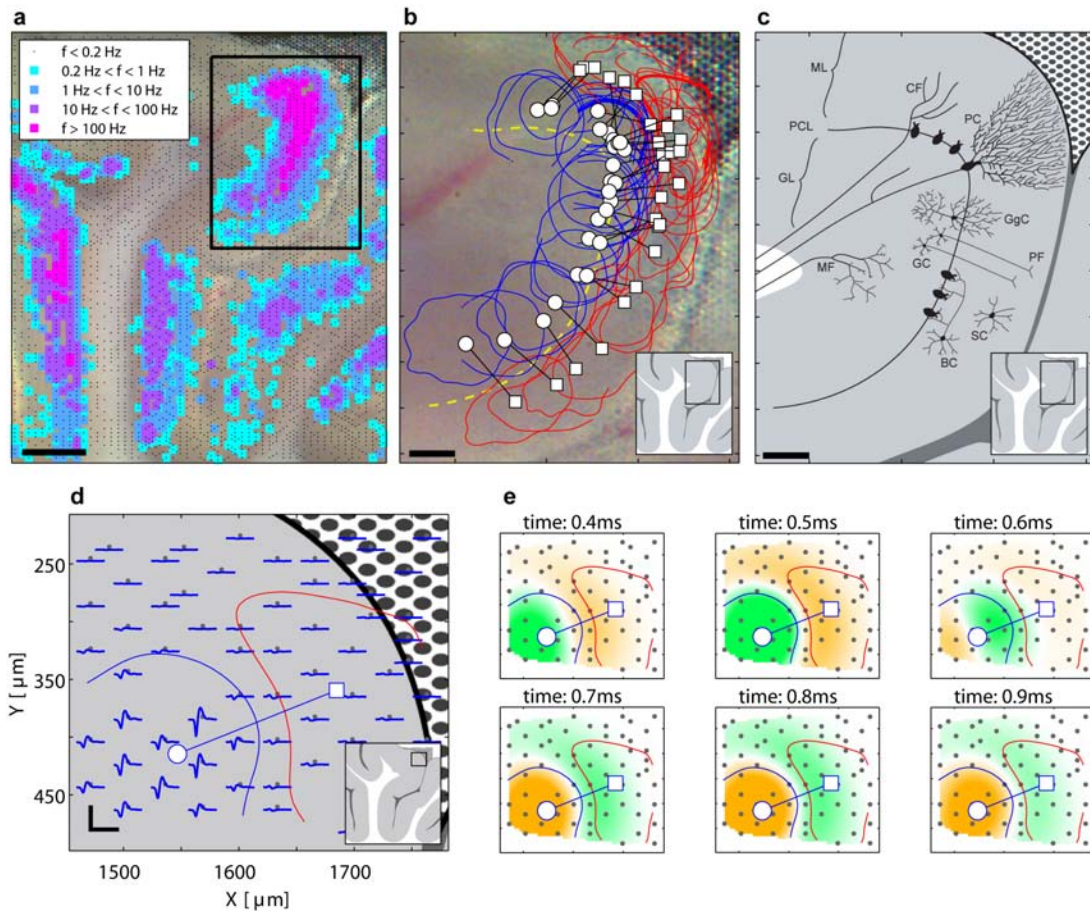


Figure 4.3: Recordings from a P18 acute slice preparation of the caudal half of the cerebellar vermis. (a) Spatial distribution of detectable spike activity in the recording area. All electrodes used for recording are marked with a small dot (approximately 30% of the available electrodes). Events exceeding a threshold of $\pm 36 \mu\text{V}$ were used to calculate the color-coded event rate; scale bar: 0.3 mm. Spike activity is found in a broad band following the cerebellar cortex. (b) Close-up of a region delimited in (a) with high activity. All units identified by spike sorting are marked in analogy to Figure 4.2f; scale bar: 0.1 mm. (c) Schematic of the basic cellular structures in the plane of the slice [Gray, 1918]. ML: Molecular layer, PCL: Purkinje cell layer, GL: Granular layer, CF: Climbing fiber, MF: Mossy fiber, PF: Parallel fiber, PC: Purkinje cell, GgC: Golgi cell, SC: stellate cell, BC: basket cell; scale bar: 0.1 mm. (d) Footprint of a neuron selected from the region shown in (b); scale bar is 200 μV , 1.9 ms. (e) CSD analysis for the cell shown in (d) at several points in time (green: sink; orange: source). The sink moves from the soma at 0.4 ms to the proximal dendrites at 0.6 ms and covers the dendritic area, while the soma repolarizes. Frequency band: 180 Hz-3.5 kHz.

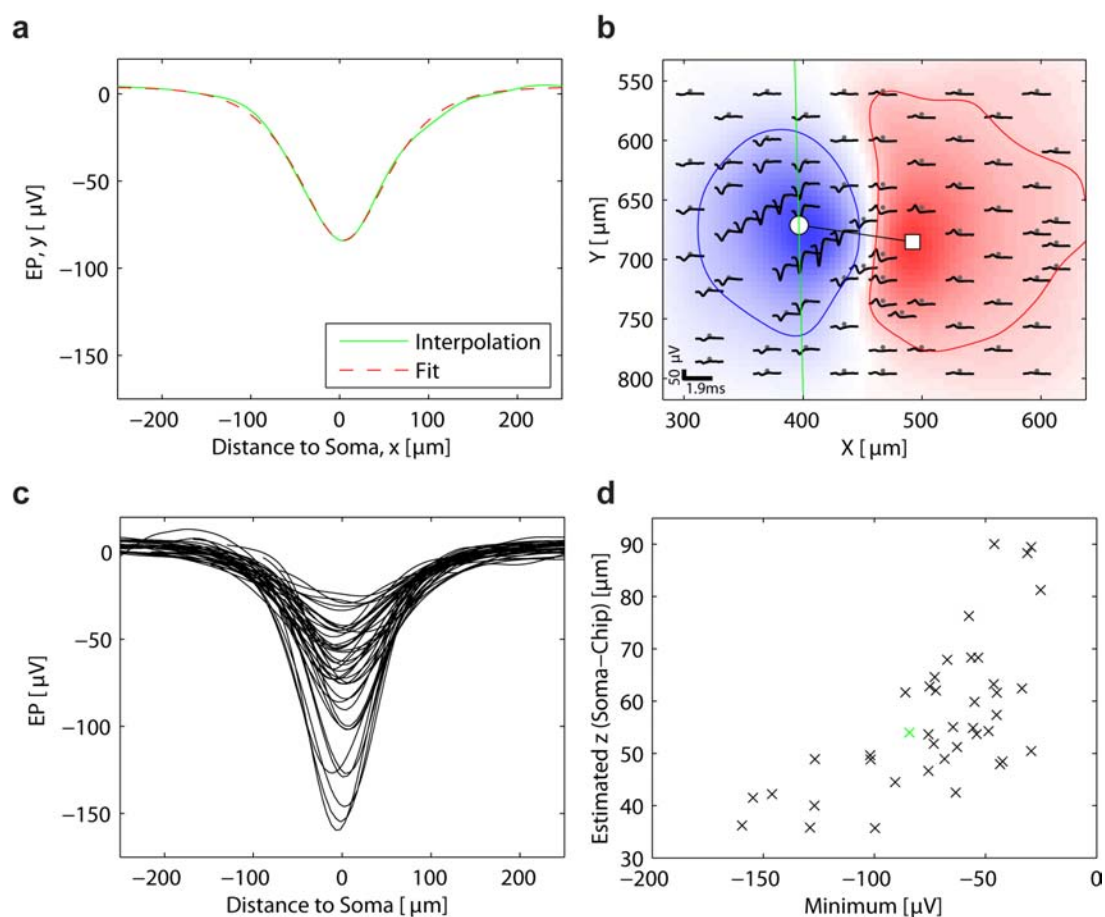


Figure 4.4: Estimation of the height of the PC above the chip surface. (a) The green curve represents the interpolated potential of a recorded spike along the solid green line in (b). The dashed red line shows the best fit according to equation (1). (c) Interpolated average potential distributions of 41 cells in analogy to (a); (d) Plot of the estimated height of the soma center, z , versus the voltage minimum of the spike. The green cross marks the sample spike shown in (a, b).

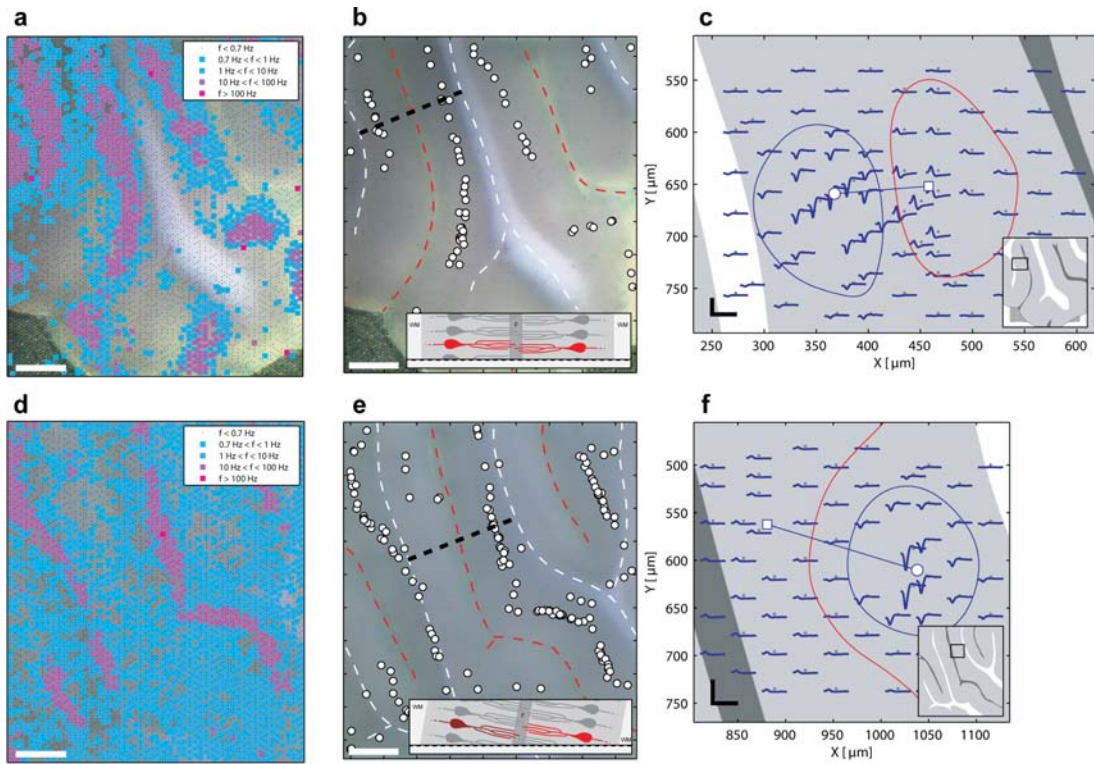


Figure 4.5: Measurements from two sagittal acute brain slice preparations (P17). (a, d) Activity map showing events larger than 4.3 times the RMS noise, with the event rate in color-coding (scale bar 0.3 mm). (b, e) Pictures of the brain slices; all detected PCs are marked by a circle, in analogy to Figure 4.2f. The red dashed line marks the fissure, the white dashed line the white matter (scale bar 0.3 mm). The insets represent sketches of cross sections as marked with the black dashed lines (F: fissure, WM: white matter). (c, f) Selected PC footprints in the corresponding slice preparation (scale bar 100 μV , 1.9 ms).

was cut along a plane that was slightly tilted with respect to the sagittal plane, so that the somata of intact PCs on the two sides of the fissure in Figure 4.5e were located at different distance to the chip surface. On the left of the fissure in Figure 4.5e the PCs close to the surface were cut through their dendrites, so that no active cells lie close to the surface, whereas to the right of the fissure, the dendrites point into the slice, and intact PCs lie next to the slice surface, as illustrated in the insets in Figure 4.5b,e. The footprints in (Fig. 4.5c,f) support this finding; the positive-amplitude spikes are a much smaller in Figure 4.5f and less confined in area than those in Figure 4.5c.

Since extracellular potentials reflect the dynamics of transmembrane currents during an AP, current source density (CSD) analysis was used by other authors to determine the location of synaptic currents, in particular in layered brain structures, such as the neocortex or the lateral geniculate nucleus. As yet, CSD analysis mostly has been applied to local field potential recordings and, only in one case, to single cells [Blanche et al., 2005]. The large number of tightly spaced electrodes of HD-MEAs, however, provides 2D subcellular resolution and, hence, gives access to the current dynamics of individual neurons. As PC activities are independent, we calculated individual time-resolved CSD distributions. The CSD structure revealed distinct dipole fields oriented in parallel to the HD-MEA surface. At spike onset there was a pronounced sink around the presumptive location of the PC soma and an equivalent, but spatially less focused, source in the ML (Fig. 4.3e). The sink then shifted towards the ML into the region of the proximal dendrites, where it slowly faded away. This backpropagation of the AP into the proximal dendrites was clearly visible and reproducible (see Fig. 4.6-4.7).

4.2.2 Comparison to a Purkinje Cell Model

A compartmental model of a PC [Roth and Hausser, 2001, Vetter et al., 2001] was built to enable a detailed interpretation of the spatio-temporal features of the extracellular recordings. The footprints obtained in our recordings featured very stereotypic shapes so that the precise morphology of the PCs seemingly was of minor importance [Gold et al., 2006]. However, the distribution of especially the Na^+ channels on the compartment model is critical to reproduce the footprints observed, which depended on a high concentration of Na^+ in the axon initial segment combined with a Na^+ channel concentration decay in the dendritic trunk (see Section 4.4).

The PC dendritic tree was oriented approximately plane-parallel to the HD-MEA surface (Fig. 4.8b). In this specific example, the soma center was slightly closer to the surface (center 40 μm above the surface) than the center of the dendritic tree. The spatio-temporal structure of the simulated cell signals was in good agreement with the experimental results (Fig. 4.8a). The simulations confirmed that the density of 3,150 electrodes/ mm^2 of the HD-MEA is sufficient to capture the details of the extracellular signal distribution (Fig. 4.8c) of neurons located

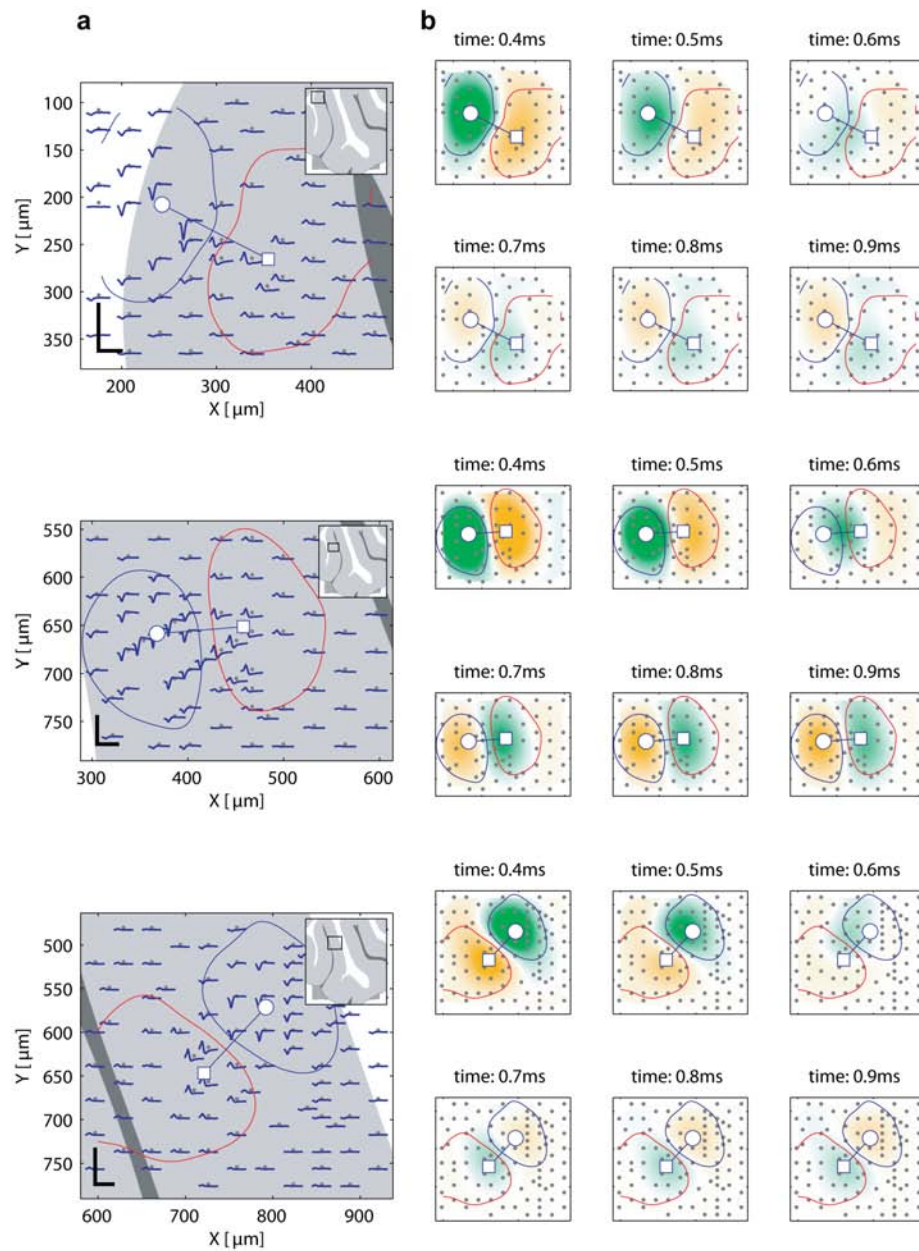


Figure 4.6: Additional footprints together with their CSD analysis, as explained in Figure 4.3d and 4.3e. (scale bar: 200 μV , 1.9 ms).

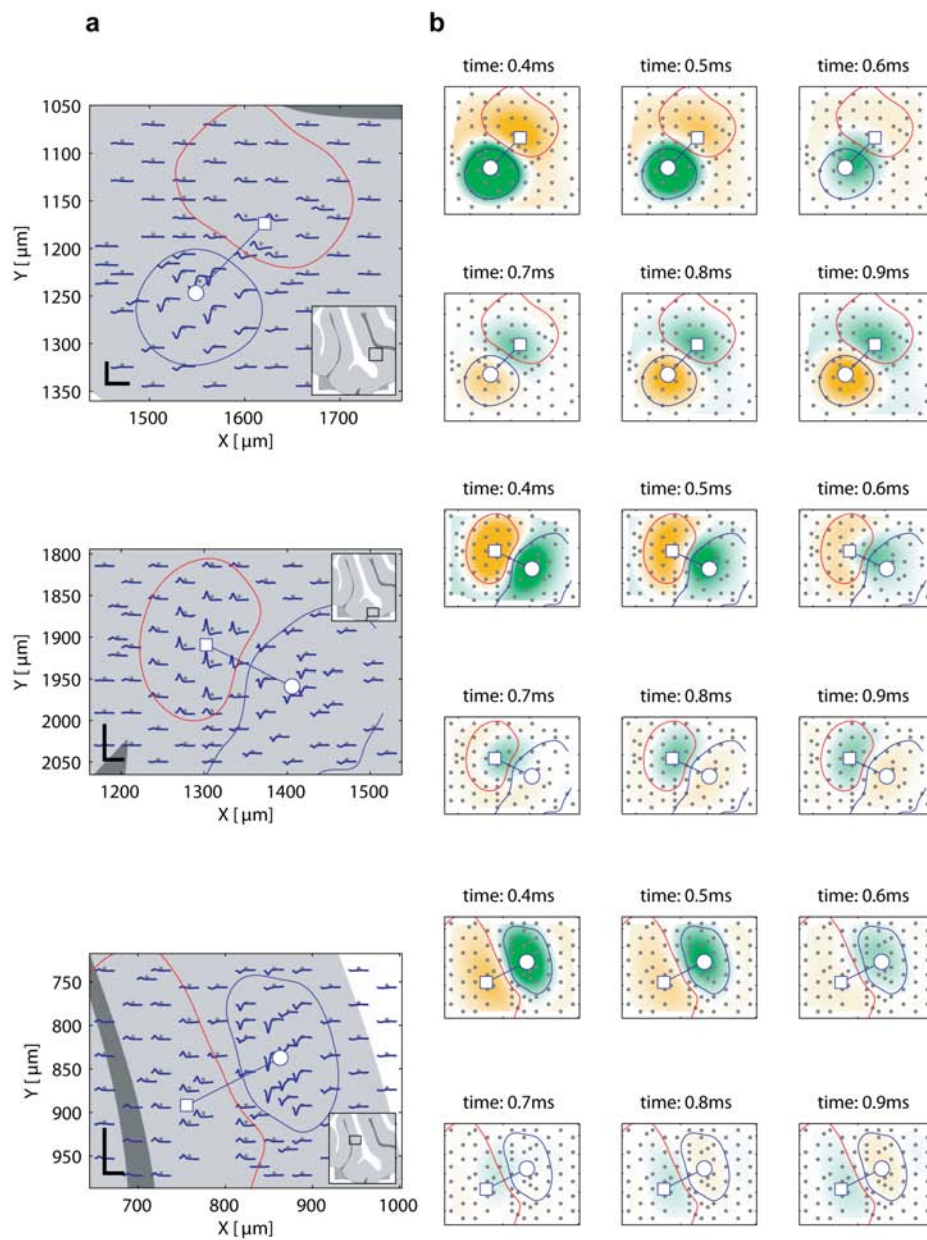


Figure 4.7: Additional footprints together with their CSD analysis, as explained in Figure 4.3d and 4.3e. (scale bar: 200 μV , 1.9 ms).

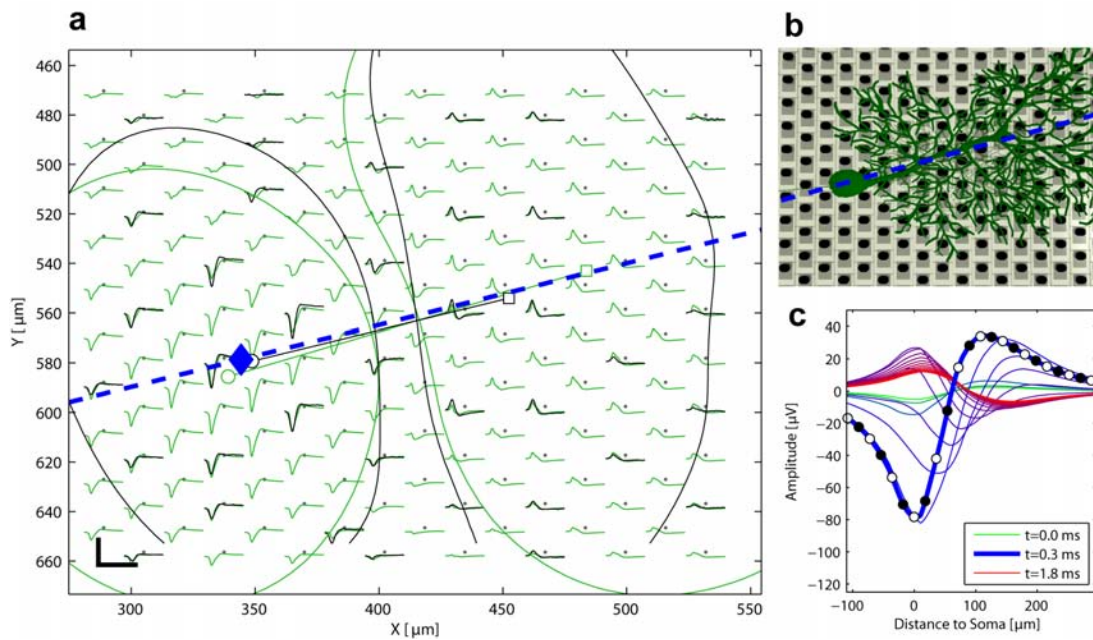


Figure 4.8: (a) Comparison of the recorded average single-unit spikes (black traces) and the spikes calculated from a compartment-model simulation of a PC (green traces). The markers for simulated and recorded units are the same as in Figure 4.2f; scale bar is $100 \mu\text{V}$, 1.9 ms . (b) Position and orientation of the simulated PC with the center of the soma located (blue diamond in (a)) $26 \mu\text{m}$ above the chip surface. (c) Simulated potential on the chip surface along a line parallel to the soma-dendrite axis (dashed blue line in (a) and (b)) during the spike evolution at 0.1 ms intervals. The black and white dots on the potential line of maximal amplitude (bold blue line) represent the electrode array spatial resolution ($18 \mu\text{m}$ pitch). Reducing the spatial resolution by 50% (black dots only, pitch $36 \mu\text{m}$) will already lead to a significant spatial undersampling of the potential distribution curve. Frequency band: 5 Hz - 3.5 kHz .

at a depth corresponding to the thickness of the cell layer damaged by the slicing procedure (20 - $50 \mu\text{m}$).

CSD distributions calculated from simulations were in good agreement with the measured CSD distributions (Fig. 4.9). The balloon-shaped equipotential surfaces (Fig. 4.9d) were somewhat drawn towards the chip, the surface of which was modeled as an insulator. This effectuated a 1.6-fold increase of the signal amplitude in comparison to models without an insulating chip surface. Additional simulations showed that the signal amplitude is reduced by only a few percent by using electrodes with diameters up to $30 \mu\text{m}$, depending on the surface-cell distance and the dynamics of signal propagation within the cell (data not shown). Similar findings have been reported for in vivo applications of shaft-type neuronal probes [Moffitt and McIntyre, 2005]. A shorter distance between cell and electrodes resulted in higher peak amplitudes and more finestructure of the CSD.

The sinks in the model represent a large influx of positive ions into the cell through Na^+ channels. A spatially extended source region develops in the den-

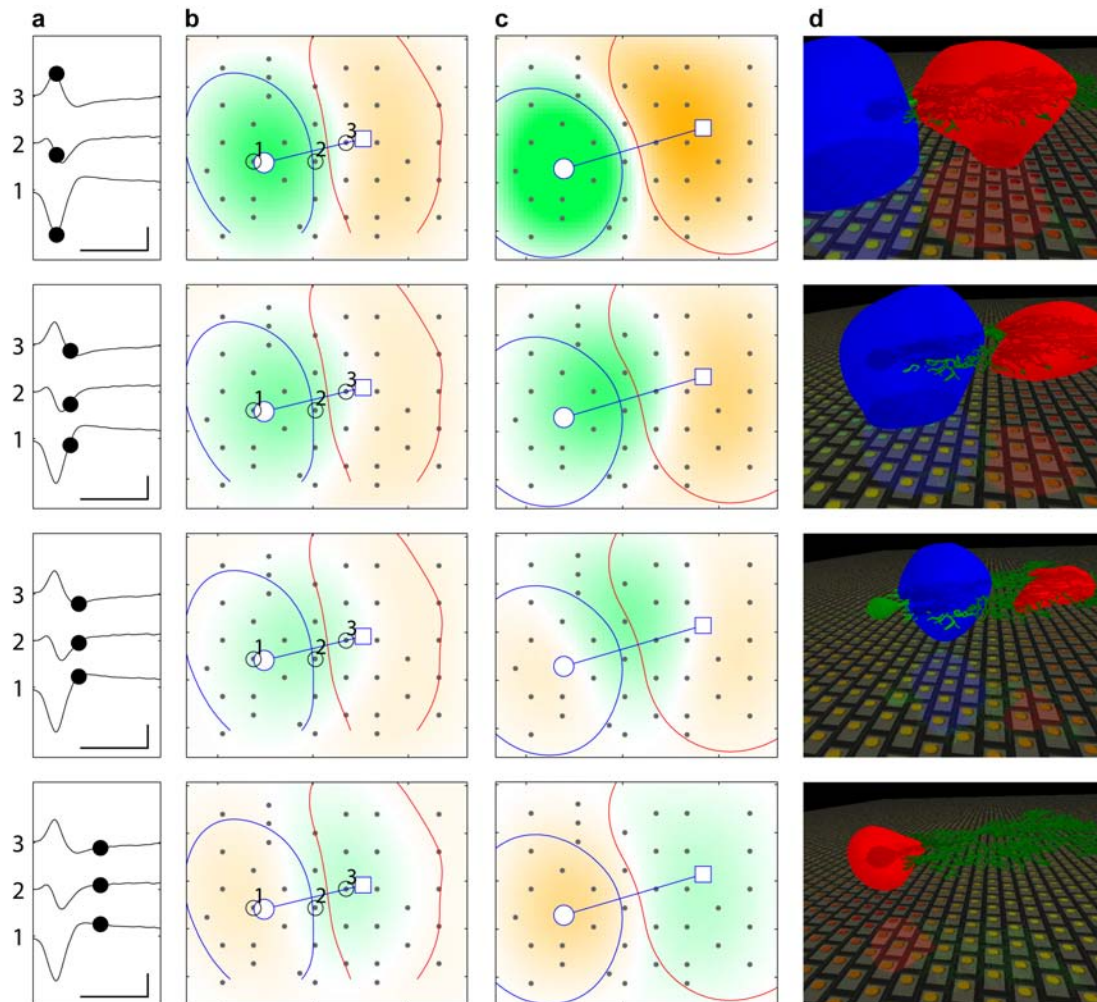


Figure 4.9: Comparison of measured and simulated evolution of the CSD during an AP. (a) Average spike recorded from the three electrodes assigned (1-3) in (b) at the specified times; scale bar is $50 \mu\text{V}$, 1 ms . (b) CSDs resulting from the measured spikes and (c) CSDs from simulations at defined points in time specified in (a). The spatiotemporal structures of the measured and simulated CSD distribution are very similar, although they differ in some details, since a rather general PC model was used in the simulation. (d) Equipotential surfaces at $-35 \mu\text{V}$ in blue and $+35 \mu\text{V}$ in red of the simulated PC. Note, that the chip distorts the equipotential balloons, which increases the signal near the electrodes.

drite, which can be assigned to passively drawn currents. Backpropagation of the AP into the dendrites is clearly visible. As PC dendrites lack active sodium channels in the distal dendrites, this backpropagation is thus mostly passive and limited to the proximal stem of the dendrite, in agreement with findings from single-cell patch-clamp studies [Stuart et al., 1997].

4.3 Discussion

Spike activity could be readily recorded in acute cerebellar slices with signal-to-noise ratios comparable to tungsten electrodes or passive planar electrode arrays. The large number of available electrodes facilitated spike sorting based on the spatio-temporal structure of the potential distribution and enabled a reliable identification of units at a given electrode. The footprint of each unit covered an area that extended well beyond the soma, but only partially covered the extension of the dendritic tree, which is in good agreement with estimates from *in vivo* and *in vitro* recordings [Egert et al., 2002].

Although spikes provide information about transmembrane currents, their characteristics are still not fully understood. Even though many cellular parameters are not available in the literature, and although the morphology of the PC here is not precisely known, the model showed a good qualitative match to the recorded data. The signal amplitude is sensitive to the intracellular resistivity, R_i [Gold et al., 2007], the extracellular conductivity, σ , and the distance between cell and chip surface, which includes contributions to account for a potential increase of conductivity in the outermost layer of dead cells. These parameters predominantly influence the overall amplitude and, to a lesser extent, the shape of the spike, which is much more sensitive to the distribution and dynamics of the active ion channels [Gold et al., 2006]. Therefore, high-resolution extracellular recordings provide a valuable tool to test and improve compartment models of neuronal cells.

From the modeling of the spike dynamics it became evident that the isolator nature of the chip and, to a lesser extent, the specific electrode structure influence the shape of the equipotential surfaces, and therefore the signal-to-noise ratio. The isolator nature of the chip partially compensates for the larger conductivity in the adjacent liquid phase resulting from dead cells or cell debris close to the surface.

CSD analysis has so far only been applied to assess population activity or one-dimensional recording patterns; here it has been applied in two-dimensions to single neurons. The HD-MEA electrode spacing provides a sufficient density of recording sites to assess subcellular sink/source distributions. The spatio-temporal CSD features in our recordings are in good agreement with those extracted from patch-clamp data and models based on measured ion channel dis-

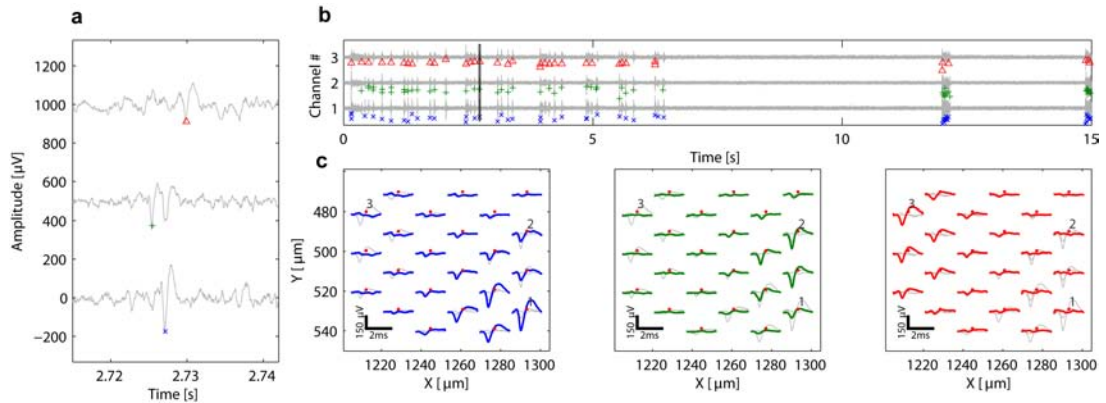


Figure 4.10: Electrophysiological measurements with the HD-MEA neuronal cell cultures. (a-c) shows data from a bursting culture of dissociated rat hippocampal neurons at day 16 *in vitro*. The long traces in (b) show raw data recorded on three selected electrodes (marked 1-3 in (c)). Events detected by a spike sorter are marked for three different neurons. The events occurred in bursts, a zoom into a short burst is shown in (a), with the time marked in (b). In (c), the spike-triggered averages of the three cells are shown. The positions of the three selected electrodes are marked with 1-3.

tributions in the dendritic tree [Stuart and Hausser, 1994]. The CSD data here reveal the extent of the backpropagation of APs.

To fine-tune the compartment model, detailed morphological and immunohistochemical analyses need to be combined with spatially highly resolved electrophysiological recordings. The resulting models will help to understand extracellular single-cell potential patterns and their contributions to the population activity recorded as local field potentials. They will further provide important information for spike sorting and will facilitate the identification of neuronal cell types in extracellular recordings. The agreement between measured data and the PC model in this study shows that the HD-MEA provides sufficient spatial and temporal resolution to capture the entire dynamics of the fast spike. The chip system provides detailed information on the spike shape and on how the spike distribution changes over time.

The chip and system will help to reveal how spikes depend on the activity level of the cell [Quirk et al., 2001] taking into account the neuronal network environment. It also can be used to monitor the spatio-temporal dynamics of activity in cultured neuronal networks and monolayers and microtissues of cardiac myocytes (Fig. 4.10). The system can potentially be applied to cultured or organotypic slices of the brain or the spinal cord, to retinal preparations and to other biological preparations involving electrogenic cells.

CMOS-based HD-MEAs enable high spatio-temporal resolution recordings and stimulation in relatively large areas, which allows for (i) a more detailed analysis of the behavior of individual neurons in a network, and for (ii) recording from a

larger fraction of neurons to assess collective behavior and the details of signal processing in neuronal networks. Besides the possibility to perform an overview scan of a cell ensemble (with the option of using electrical stimulation), to then select cells that are prominent in the networks signal processing and to trace their interaction, the CMOS-based active devices bear the potential to provide insights into subcellular mechanisms underlying the respective action-potential dynamics.

Selecting a subset of electrodes from a high-density array while providing low-noise signal amplification and filtering will be useful for many applications. The method presented here is likewise applicable to *in vivo* shaft-style probes [Najafi and Wise, 1986, Csicsvari et al., 2003]. There, it would simplify the tracking of neurons displaced by minute movements or tissue response.

4.4 Methods

4.4.1 CMOS-based Microelectrode System

The HD-MEA consists of several components on a single chip (Fig. 4.1a, e). The 126 readout channels provide signal conditioning with programmable amplification (1-10,000-fold). A first-order high-pass filter with adjustable cutoff frequency (0.3 Hz-100 Hz) removes DC offset and fluctuations resulting from the electrode-saline interface. A tunable second-order low-pass filter defines the upper frequency limit (3.5-14 kHz). The signals are sampled at 20 kSamples/s per channel using 8-bit analog-to-digital converters (ADCs). Electrical stimuli can be delivered through a 10-bit digital-to-analog converter (DAC). The total recording area of the 11,011 electrodes is $2.0 \times 1.75 \text{ mm}^2$ (3,150 electrodes/ mm^2). Flexibility in the electrode selection is attained by an analog switch matrix integrated underneath the electrode array (Fig. 4.1d and 3.5). The low-power design prevents heating of the biological preparation [Frey et al., 2007c].

4.4.2 Acute Slice Preparations

Parasagittal cerebellar slices (300 μm thick) were prepared from Long-Evans rats at postnatal days 16-18 as described previously [Heck, 1993]. Animals were anesthetized with isoflurane and decapitated. The brain was quickly removed and rinsed in ice-cold ($<4^\circ\text{C}$) artificial cerebrospinal fluid (ACSF; contents in mM: NaCl 132.0, KCl 2.0, KH_2PO_4 1.2, MgSO_4 1.1, NaHCO_3 19.0, CaCl_2 2.5, D-glucose 10.0, continuously gassed with 95% O_2 , 5% CO_2). Rats were housed and handled in accordance with the guidelines of the Univ. Freiburg and German law. Slices were cut with a vibratome (Dosaka), stored at 37°C for 1h and kept at room temperature thereafter. Recordings were performed at 28°C with 8 buffer exchanges/min.

To improve tissue adhesion, HD-MEAs were coated with cellulose nitrate (CN, Schleicher & Schuell, Dassel, Germany), dissolved in methanol (0.14 mg/ml) [Egert et al., 2002]. Slices were cut in half along the main stem of the white matter, and one of the pieces of the caudal section was positioned above the HD-MEA in a drop of artificial cerebrospinal fluid (ACSF). ACSF was then quickly and completely removed so that the slice settled onto the HD-MEA surface and adhered. The slice covered the electrode array almost completely.

4.4.3 Recordings

The recording setup consists of a custom-designed printed circuit board (PCB), a field-programmable gate array (FPGA), and a computer (Fig. 3.9). As 126 out of 11,011 electrodes are selected for recording, a twophase strategy was adopted: (1) an activity map (Fig. 4.3a) was generated from partially overlapping blocks of regularly spaced electrodes, covering patches of $0.3 \times 0.3 \text{ mm}^2$ to $0.5 \times 0.5 \text{ mm}^2$. This produced up to 50 recordings of roughly 1 minute duration. (2) Recordings at a higher resolution were then performed in selected ROIs. In total, we recorded from five cerebellar slices.

4.4.4 Spike Sorting

Events from multi-unit recordings were sorted according to their shape. Owing to the high electrode density, each signal source, i.e., each neuron is monitored by several electrodes. Blind source separation allows the separation of source signals from a set of mixed signals, which can be recovered by ICA assuming additive superposition of statistically independent non-Gaussian source signals [Lewicki, 1998, Takahashi et al., 2003a]. The large number of electrodes in our system allows us to directly apply ICA for spike sorting. The underlying assumption of an additive superposition of sources holds only in a first approximation, so that the events in independent components need to be clustered. The algorithm is briefly outlined here: (1) band-pass filter (500-3000 Hz), (2) ICA (using FastICA [Hyvarinen, 1999]) yielding separated independent components (IC), (3) threshold detection on the ICs using ± 4.2 standard deviations, (4) alignment of the events for maximal correlation with a template spike. (5) events are then clustered according to the shape of the ICs [Harris et al., 2000] and (6) spike triggered averages are calculated for each cluster. (7) Alternatively, the procedure is run iteratively by subtracting the spiketriggered averages from the data and repetition of steps (2) through (6). (8) Finally, spike footprints are calculated by re-extracting and averaging the events from the raw data that have been band-pass filtered at 5-4400 Hz.

4.4.5 Current Source Density

CSD [Nicholson and Freeman, 1975] analysis is frequently applied to extracellular potentials, as the source current provides a better contrast between the current sinks, $\mathbf{I}_{csd} < 0$, and sources, $\mathbf{I}_{csd} > 0$, in the medium as compared to the extracellular potential Φ_e ,

$$\mathbf{I}_{csd} = -\nabla \cdot \sigma \cdot \nabla \Phi_e$$

A homogenous and isotropic medium conductivity is assumed, and therefore,

$$\mathbf{I}_{csd} = -\sigma \cdot \Delta \Phi_e.$$

We can then approximate the CSD by applying the LoG operator (Laplacian of Gaussian) to the interpolated (grid of 5 μm) potential Φ_e . The convolution filter of the LoG can be calculated as

$$LoG(x, y) = \frac{x^2 + y^2 - 2w_\sigma^2}{2\pi w_\sigma^6} \cdot \frac{G(x, y)}{\sum_x \sum_y G(x, y)},$$

$$G(x, y) = e^{-\frac{x^2 + y^2}{2w_\sigma^2}}$$

and w_σ is chosen as 1.5 times the electrode spacing. An accurate value of the conductivity is difficult to obtain, therefore all CSDs are given in arbitrary units with sinks marked in green and sources marked in orange.

4.4.6 Extracellular Action Potential Model

To calculate the extracellular potential induced by an action potential (AP) in the model we modified the approach described in Gold et al. [Gold et al., 2006]. It consisted of two stages. First, the dynamic transmembrane potential and the currents were computed using the NEURON 5.9 simulation environment [Hines and Carnevale, 1997] with a detailed compartment model [Vetter et al., 2001]. The obtained membrane currents, $I_m(n)$, were used to calculate the DC electric field in a conductive medium.

The extracellular mechanism included in NEURON was used to calculate the membrane currents. The two-step procedure is suitable, since transmembrane currents do not significantly affect the extracellular potential in comparison to the voltage drop across the membrane [Gold et al., 2006]. For point-current sources in an infinite isotropic, homogenous volume conductor, the electrical potential, Φ_e , can be calculated as [de No, 1947, Klee and Rall, 1977]:

$$\Phi_e = \frac{1}{4\pi\sigma} \sum \frac{I_m(n)}{d(n)},$$

where σ is the conductivity of the medium and d the distance from the current source, $I_m(n)$. The cylindrical compartments were modeled as point sources and not as line source approximations as described in [Holt and Koch, 1999], since the ratio of d and the compartment length is large. The extracellular conductivity was shown to be inhomogeneous and anisotropic in the cerebellum [Kwan and Murphy, 1974, Okada et al., 1994, Yedlin et al., 1974], which was neglected, as accurate values are difficult to obtain. Capacitive or low-pass filtering effects of the extracellular medium as described by other authors [Bedard et al., 2006] have been neglected, since the effect was estimated to be marginal given the cell-to-electrode distances in slices and the frequency range of interest. A homogenous and isotropic extracellular conductivity of $\sigma=0.22$ S/m was used here.

Based on this model the ideal extracellular potential was calculated on a grid in three dimensions around the neuron (MATLAB R2007b, MathWorks, Natick, MA). Next, the simulated neuron was semi-automatically positioned to match with the measured neuron (Fig. 4.8a). Finally, we solved a finite-element model (FEM) that takes into account the chip surface as an insulator (the amplifiers have a very high input impedance) using FEMLAB's conductive media DC application mode (COMSOL 3.3). The assumptions described above allow for a quasi-static description of the electric field, \mathbf{E} , in the extracellular space [Mitzdorf, 1985]. Ohm's law holds for the current density, \mathbf{J} :

$$\mathbf{J} = \sigma \mathbf{E}.$$

The model was solved in a cylindrical domain with an insulator, $n\mathbf{J} = 0$, as the boundary condition for the bottom plate (the chip surface), whereas the upper plate and the cylinder wall were grounded: $\Phi_e = 0$. The platinum electrodes (10% of the overall chip surface) have been neglected. Equipotential surfaces were calculated and visualized using POV-Ray 3.6.

The morphology of a PC was taken from Figure 2 in Roth and Hausser 2001, cell 3 in ref. [Roth and Hausser, 2001]. The Na reversal potential has been set to 71 mV. $\text{Na}_v1.1$ channels (implementation from [Khaliq et al., 2003, Akemann and Knopfel, 2006]) feature a maximum density on the soma of 0.22 S/cm² and decay rapidly to zero in the dendritic trunk (~ 0.1 S/cm² at 50 μm and below 0.025 S/cm² at 100 μm and further away from the soma) [Stuart and Hausser, 1994, Migliore and Shepherd, 2002, Trimmer and Rhodes, 2004, Bekkers and Hausser, 2007]. The $\text{Na}_v1.6$ channel modified from [Akemann and Knopfel, 2006] with a slightly lower activation threshold has been placed at high density on the initial segment (0.6 S/cm²) and on the nodes of Ranvier (1.5 S/cm²) [Boiko et al., 2003, Kole et al., 2008]. The K^+ channels were implemented using K, D, A, BK types of voltage- and calcium-activated channels as well as I_h [Gold et al., 2006]. K^+ channels were placed at high density on the nodes and the initial segment [Kole et al., 2007]. Intracellular resistivity, R_i , was set to 70 Ωcm in the soma and the dendrites and to 50 Ω in the axon [Gold et al., 2006]. A passive leakage current with a reversal potential of -65 mV and a membrane resistance

of $R_m=15 \text{ k}\Omega\text{cm}^2$ (myelin: $40 \text{ k}\Omega\text{cm}^2$, nodes: $2 \text{ k}\Omega\text{cm}^2$) was included. The membrane capacitance, C_m , was set to $1 \text{ }\mu\text{F}/\text{cm}^2$. Spines were accounted for by scaling membrane capacitance and conductivity. The axon was modeled similarly to ref. [Mainen et al., 1995]. We simulated synaptic activation by lowering the membrane resistance at the distal dendrites and increased the reversal potential to -40 mV [Destexhe and Pare, 1999]. Channel types that do not significantly contribute to the signal shape were omitted.

4.4.7 Estimating the height of the PC above the chip surface

To obtain an estimation for the height, z , of the recorded cells above the chip surface (surface – center of soma) we looked at the potential distribution at the time of the negative-signal peak maximum along a line (green line in Fig. 4.4b) through the soma marker. This line is in the plane of the chip surface and perpendicular to the gradient of the electric field between the soma and dendrite markers. The decay of the potential with increasing distance from the cell can be described as $\Phi_e \propto d^{-b}$, depending on the distance regime, with b ranging between 1 and 3: $1 < b < 3$ (point-source, dipole, linear quadrupole). The potential decay can be fitted with an exponential [Gold et al., 2007] $\Phi_e \propto e^{-kd}$. We used the FEM model to constrain the parameter, k , for the decay along the perpendicular line described above and obtained:

$$k = 0.05e^{-0.02z} + 0.01.$$

The potential along this line can then be described as:

$$y = ae^{-kd} + c,$$

With:

$$d = \sqrt{(x - s)^2 + z^2}$$

where a is a fit parameter for the amplitude (dependent on the total membrane current, conductivity and distance), which is independent of the shape that only depends on z . To account for offset and shift in x (distance on the chip surface to the soma marker) c and s are also free parameters. In this approach z is estimated based on the potential distribution shape of a given neuron model and z is independent of the amplitude. For peak amplitudes of -25 to $-150 \text{ }\mu\text{V}$ the height was estimated to $30\text{-}90 \text{ }\mu\text{m}$ above the array surface, which is in good agreement with estimates based on visual inspection of intact cells (Fig. 4.4d). The spread presumably results from different total membrane currents, which depend on cell size, as well as different cell orientations and morphologies.

Acknowledgments

The authors would like to thank R. Pedron, K.-U. Kirstein, D. Scheiwiller, and F. Greve for their contributions to the development of the device. U. Wahlen and J. Sedivy, C.D. Bustamante, A. Blau, T. Neumann and B. Roscic are acknowledged for help with the measurements and the data analysis and H. Baltes for sharing laboratories resources. P. Vetter et al. are acknowledged for the model program *Dendritica* featuring Purkinje cell morphologies, and the EMZ, University Zurich for providing Figure 4.1c. Financial support was kindly provided by ETH under the internal grant TH-00108, the German BMBF under grant no. 01GQ0420 (U.E.) and EU-NEURO grant no 12788 (U.E.).

Chapter 5

Electrical Properties of Cardiomyocytes

Carlota Diaz Sanchez-Bustamante¹, Urs Frey², Jens M. Kelm³,
Andreas Hierlemann², and Martin Fussenegger¹

Tissue Engineering, 2008, in publication

¹Institute for Chemical and Bio-Engineering, ETH Zurich, Switzerland

²Physical Electronics Laboratory, ETH Zurich, Switzerland

³Clinic of Cardiovascular Surgery, Zurich University Hospital, Switzerland

*The chapter includes a subset of the experiments and methods
contained in the original paper [Sanchez-Bustamante et al., 2008].*

See Section 2.1 for the contributions.

Abstract Since cardiomyocytes lose their ability to divide after birth, any subsequent cell loss or dysfunction results in pathologic cardiac rhythm initiation or impulse conduction. Strategies to restore and control electrophysiological activity of the heart may, therefore, have a great impact on the regeneration of cardiac tissue functionality. Using lentivirus-derived particles to regulate bone morphogenetic protein-2 (BMP-2) gene expression in a pristinamycin-inducible manner, we demonstrate the adjustment of the electrophysiological characteristics of cardiomyocytes. We have made use of CMOS-based high-density microelectrode arrays (HD-MEAs) to monitor the electrophysiological activity of neonatal rat cardiomyocytes (NRCs) cultured either as monolayers (NRCml) or as microtissues (NRCmt). NRCmt more closely reproduce the heart tissue physiology and could be conveniently monitored using HD-MEAs due to their ability to detect low-signal events and to sub-select the region of interest, e.g., areas where the microtissues were placed. Significantly, cardiomyocyte-forming microtissues, transduced with lentiviral vectors encoding the (BMP-2), were capable of restoring the electrical activity of the myocardial microtissue. The controlled expression of therapeutic transgenes represents a crucial advancement for clinical interventions as well as for advanced gene-function analysis.

5.1 Introduction

Cardiomyocytes are responsible for heart contractions and are the dominant cell type in the normal heart with respect to volume. Irregularities in the heartbeat, due to cardiac electric dysfunction, are one of the most frequent causes of mortality and morbidity in today's industrialized society [Cohn et al., 1997]. An increasing number of cardiac electrical diseases have been related to dysfunction of ion channels, such as the long-QT syndrome, and to defects in contractile proteins, structural proteins, or signaling molecules [Keating and Sanguinetti, 1996, Lehmann-Horn and Jurkat-Rott, 1999]. These ion channelopathies or cardiac excitation-coupling disorders lead to cardiac arrhythmias and other cardiomyopathies [Gambit, 2001, Priori and Napolitano, 2006]. There is, accordingly, a compelling need to move clinical studies toward cardiac regenerative therapeutic strategies aimed at improving cardiac functionality [Chien, 2006, Kehat et al., 2004, Rubart and Field, 2006, Rubart et al., 2003]. This will require more complex *in vitro* models that enable the study and assessment of how potent therapeutic genes, related to heart functionality, impact cardiac electrophysiological irregularities [Stett et al., 2003b].

Cardiac cells (cardiomyocytes) isolated from a neonatal heart adapt readily to culture plates and maintain an intact myofibrillar apparatus, as demonstrated by their beating [Atherton et al., 1986]. Neonatal cardiomyocytes have, therefore, emerged as the preferred cell type because of their inherent structural, electrophysiological and contractile properties [Chlopcikova et al., 2001], which make them suitable for the study of contractile activities [Galaris et al., 1980, Harary and Farley, 1963a,b]. Despite global initiatives to foster advances in cardiomyocyte-related therapies, this cell type has turned out to be refractory to

gene transfer technologies, particularly with regard to its terminally differentiated adult phenotype [Datwyler et al., 2001]. Based on the ability of pseudotyped lentiviral vectors to transduce a wide variety of cell types and tissues, including quiescent cells, transgenic lentiviral particles have become an attractive gene-transfer tool for cardiac cells [Mitta et al., 2002, Sakoda et al., 1999, Zhao et al., 2002]. Moreover, lentiviral vectors have been recently engineered to regulate transgene expression [Hartenbach and Fussenegger, 2005, Mitta et al., 2005b, 2004], thus providing a powerful tool for (i) functional genomic research [Vogel et al., 2004], (ii) production of transgenes in animal models of human diseases [Regulier et al., 2003], (iii) *in vivo* or *ex vivo* titration of pharmaceutical proteins within a therapeutic range [Johansen et al., 2002, Koponen et al., 2003, Vigna et al., 2002], and (iv) rational reprogramming of the proliferation, differentiation, or apoptosis pathways to engineer specific cell/tissue phenotypes [Fussenegger, 2001, Fussenegger et al., 1998, Fux et al., 2004a,b, Kelm et al., 2004b, Mitta et al., 2004]. Capitalizing on the potential of inducible viral transgene expression [?] and on recent advances in novel regulation system [Weber and Fussenegger, 2007], we selected a lentivirus-based gene-regulation systems to genetically manipulate neonatal cardiomyocytes: a streptogramin-responsive expression system [Fussenegger et al., 2000, Mitta et al., 2004], in which addition of pristinamycin I switches off transgene expression (OFF system).

Controlling physiological changes in cell behavior on a single-cell level remains a major challenge. To this end, a cell embedded within a three-dimensional configuration/extracellular matrix (ECM) more closely reproduces its *in vivo* physiology than standard culture technologies (two-dimensional monolayer cultures) [Abbott, 2003, Zhang, 2004]. Therefore, it was sought to validate gene transfer and its impact on myocardial microtissue electrophysiology by using microtissues (NRCmt) in addition to conventional monolayer cultures (NRCml). To evaluate electrophysiological changes CMOS (complementary metal oxide semiconductor)-based high-density microelectrode arrays (HD-MEAs) have been used [Frey et al., 2007c,b, Heer et al., 2007a], which provide a reconfigurable routing for an almost arbitrary set of 126 electrodes out of a total of 11,000 to record electrical changes of multicellular cardiac myocytes in real time.

In order to modulate cardiac electrogenic properties we selected the bone morphogenetic protein-2 (BMP-2) gene, which was originally identified as a molecule that induces bone and cartilage formation [Wozney et al., 1988] but is today considered to be a multifunctional cytokine [Hogan, 1996]. It was previously reported to induce myocyte shortening [Ghosh-Choudhury et al., 2003a] and more recently suggested to control cardiac ventricular contractility upstream of MEF2A (myocyte-specific enhancer factor 2A) [Wang et al., 2007] via PI3K (phosphatidylinositol 3-kinase) [Crackower et al., 2002, Ghosh-Choudhury et al., 2003b]. BMP-2 appears to operate at several temporal points. First, during embryogenesis and differentiation, it was shown that BMP-2 is essential for proper heart tissue formation [Abdelwahid et al., 2001, Monzen et al., 2002, Zhang and Bradley, 1996]. Secondly, in the adult state, BMP-2 is involved in cardiac

functionality [Wang et al., 2007] as well as in promoting cardiomyocyte survival [Izumi et al., 2001, Masaki et al., 2005]. For these reasons expression control and a precise fine-tuning of BMP-2 expression could prove to be a potential therapy to alleviate complications in cardiac development and dysfunctional contractility at different developmental stages of the heart.

To date, proof of the control of the electrophysiological properties of cells through heterologous synthetic regulation systems is lacking. The model system described here may be useful for both, basic and applied biological research of electrically active cells. In this case, we demonstrate how the genetic control of BMP-2 modulates cardiac electrogenic activity, which might represent an important therapeutic advantage in the future treatment of heart failure.

5.2 Material and methods

5.2.1 CMOS-based high-density microelectrode array (HD-MEA)

The HD-MEA consists of 11,016 metal electrodes and 126 on-chip channels (Fig. 5.1A), each of which contains recording and stimulation electronics for bidirectional communication with electrogenic cells, as described by Frey *et al* [Frey et al., 2007d]. Each HD-MEA-based device exhibits a total array area of $1.75 \times 1.97 \text{ mm}^2$ and electrode openings of $8.2 \times 5.8 \text{ }\mu\text{m}^2$ (Fig. 5.1B). The array was fabricated in an industrial $0.6 \text{ }\mu\text{m}$ CMOS-process that features three metal layers. The electrodes were fabricated in a two-mask post-processing step; Ti:W, as an adhesion promoter (20 nm), and platinum (200 nm), as the electrode material, were sputtered onto the wafer and patterned using a lift-off process. Then, a passivation layer stack, $1.6\text{-}\mu\text{m}$ thick, consisting of alternating SiO_2 and Si_3N_4 layers (1 μm of Si_3N_4 followed by twice 100 nm SiO_2 / 200 nm Si_3N_4) was deposited by means of plasma enhanced chemical vapor deposition (PECVD) to protect the array against corrosion. Then, a glass ring was mounted and the bond wires were encapsulated with epoxy resin (EPOTEK 302 3M). A platinum wire, which represents the counter/reference electrode, was inserted into the culture medium. The recorded cell signals, simultaneously obtained from up to 126 selected electrodes, were first high-pass filtered (0.3 Hz cut off) to remove large DC offsets and fluctuations of the electrode-solution interface; the signals were amplified by a programmable-gain (amplification from 1 to 10,000 in 18 steps), low-pass filtered twice (first to 15 kHz and then to 4 kHz), and digitalized using an 8-bit AD converter with 20 KSamples/s per channel (Fig. 1B). The processed data were sent to a PC for further processing. Recordings were performed at 37°C , each recording including 20 seconds.

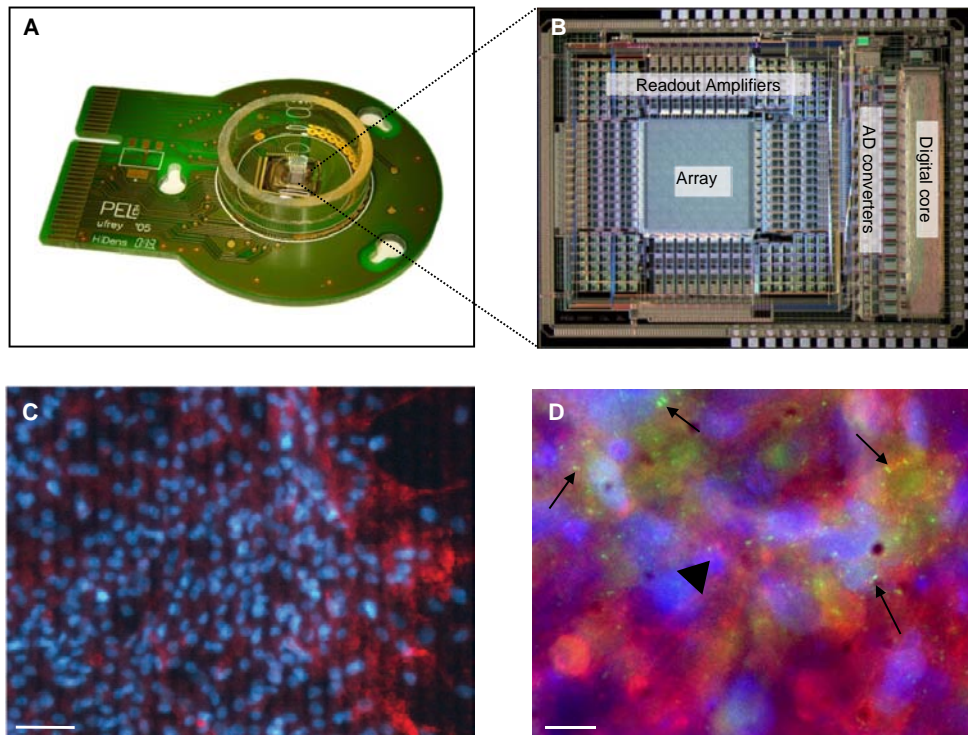


Figure 5.1: Neonatal rat cardiomyocytes (NRCs) cultured as monolayers (NRCml) on HD-MEAs. (A) Packaged HD-MEA device. (B) Overall HD-MEA micrograph. (C-D) NRCml cultured for a total of 10 days on the HD-MEA. Morphology of NRCml and electrical coupling were visualized by immunohistologic staining specific for sarcomeric α -actinin (red), 4'-6-diamidino-2-phenylindole (DAPI) (blue) and connexin 43 (green, arrows). Intercalated disks are also shown (arrow head). Scale bar 50 μm in (C) and 5 μm in (D).

5.2.2 Isolation of neonatal rat cardiomyocytes and culture on HD-MEAs

Neonatal rat cardiomyocytes (NRCs) from both, the left and the right ventricles were isolated from the hearts of newborn rats (Wistar rats; Elevage Janvier, Le Genest Saint Isle, France) by digestion with collagenase (Worthington Biochemical Corp., Freehold, NJ, USA) and pancreatin (Invitrogen, Carlsbad, CA, USA), followed by density gradient purification according to the protocol of Auerbach *et al* [Auerbach *et al.*, 1999]. One thousand NRCs were seeded in 1-ml plating media (67% Dulbecco's modified Eagle medium [DMEM; Invitrogen], 17% M199 EBS [AMIMED, Allschwil, Switzerland], 10% horse serum [Cat. No. 16050-122, Lot. No. 336379, Invitrogen], 5% fetal bovine serum [FBS; Cat. No. 3302-P251110, Lot No. P251110, PAN biotech GmbH, Aidenbach, Germany], and 1% penicillin/streptomycin solution [Sigma, St. Louis, MO, USA]), and then placed onto a HD-MEA that had been previously incubated with 20 $\mu\text{g}/\text{ml}$ laminin (Sigma) for 2 hours at 37°C. HD-MEAs containing cells were cultivated at 37°C in a humidified atmosphere containing 5% CO₂ for up to 10 days. Four hundred thousand freshly isolated cardiomyocytes, seeded in plating media and cultured on tissue culture plates (35 × 10 mm) previously coated with collagen (Sigma), were used as culture controls.

5.2.3 Immunofluorescence microscopy

NRCml seeded on HD-MEAs were washed twice in phosphate-buffered saline solution (PBS; 150 mM NaCl, 6.5 mM Na₂HPO₄ × 2 H₂O, 2.7 mM KCl, 1.5 mM KH₂PO₄, pH 7.4; Sigma Chemicals), fixed at room temperature for 30 min. in PBS containing 2% paraformaldehyde (PFA, Sigma Chemicals), washed three times for 5 min. in PBS, and permeated for 10 min. in PBS containing 0.2% Triton X-100. Primary antibodies, specific for desired proteins, as well as fluorescence-labeled secondary antibodies were diluted in 1% BSA-containing Tris-buffered saline (TBS, 20 mM Tris base, 155 mM NaCl, 2 mM EGTA, 2 mM MgCl₂) and sequentially incubated for 1 h at room temperature (RT); they were washed three times during this process. Finally, the NRCml on the HD-MEAs were washed in PBS and embedded on Tris-buffered glycerol (a 3:7 mixture of 0.1 M Tris-HCl (pH 9.5) and glycerol supplemented with 50 mg/ml n-propyl-gallat). Immunofluorescence-based analysis of NRCmt was performed as described elsewhere [Sanchez-Bustamante *et al.*, 2006]. NRCml plated on HD-MEAs as well as NRCmt required specific antibodies for sarcomeric- α -actinin (mouse monoclonal, clone EA53, Sigma Chemicals) and connexin 43 (rabbit polyclonal, sc-9059, Santa Cruz Biotechnology, Inc.), and staining with Cy3-coupled secondary anti-mouse antibodies (Jackson Immunochemicals, West Grove, PA, USA) and Cy2-coupled anti-rabbit antibodies (Jackson Immunochemicals). All the samples were co-stained with 4',6-diamidino-2-phenylindole (DAPI; Molecular Probes Inc., Eugene, OR, USA) for nuclear localization.

Confocal imaging was performed with a fluorescence microscope equipped with oil immersion objectives ($40\times/63\times$) and a confocal scanner (Zeiss LSM 510; Carl Zeiss AG, Feldbach, Switzerland) with a two-photon laser featuring a Chameleon, argon, and helium-neon laser. Images were obtained with a BP 565-615 filter for Cy3 dye or BP 490-520 filter for Cy2 fluorescence. A BP 390-465 filter was used for DAPI detection. Image acquisition was performed by multitracking the different filters; the data were processed by Zeiss LSM software and a 3D multichannel image processor (Bitplane, AG, Zurich, Switzerland). Fluorescent micrographs from NRCml on HD-MEAs were obtained using an upright microscope (DM IL, Leica Microsystems AG, Glattbrugg, Switzerland) equipped with a digital camera (DC300FX, Leica Microsystems), and the filters for Cy2, Cy3, and UV light (Leica Microsystems). Fluorescent images from tissue culture plates were taken using a Leica AF6000 system equipped with a DMI 6000B microscope and a DFC350 FX digital camera (Leica Microsystems). Videos were taken by standard Leica light microscopy (Leica DMIL, Leica Microsystems) and a digital camera (Canon, Power shot S50).

5.2.4 Data analysis

Data analysis was performed using MATLAB software (2007a, MathWorks, Natick, MA). The data were high pass filtered at 10 Hz in addition to the filtering on the HD-MEA. RMS noise was estimated as described by Quiroga et al. [Quiroga et al., 2004]. Nonviable channels, such as channels providing values at the rails, were discarded. Events were detected using a threshold set to 4.5 times the RMS noise level. Events were upsampled to 100 kHz and then aligned with regard to the center between the first positive peak (maximum) and the following negative peak (minimum). If the first positive peak was missing, the events were aligned with regard to the negative peak. As an accurate timestamp is pivotal to determining the wave propagation characteristics, the timestamps were obtained in the following way. An overall spike shape template was calculated as the average of all aligned events. The peak of the normalized cross-correlation between the events and the template was then used as a timestamp, which was less sensitive to noise and showed improved accuracy over the peak-based timestamp described above. Next, waves (bursts) were detected if the inter spike interval (ISI) falls below a threshold based on the total activity and at least 25% of all viable channels participate in the wave.

Four parameters were then used, two parameters characterizing the culture (frequency and propagation velocity) and two describing the signal shape (signal amplitude and upstroke duration). The frequency was taken as one over the mean inter burst interval (IBI), which represents the rhythm of the culture (Fig. 5.2A). Rhythm variability corresponds to the coefficient of variation of the IBI. The propagation velocity was averaged over all bursts within one recording (an example of one burst in Figure 5.2B) and calculated in the following way: a two-dimensional map of the time difference between the first event within a burst

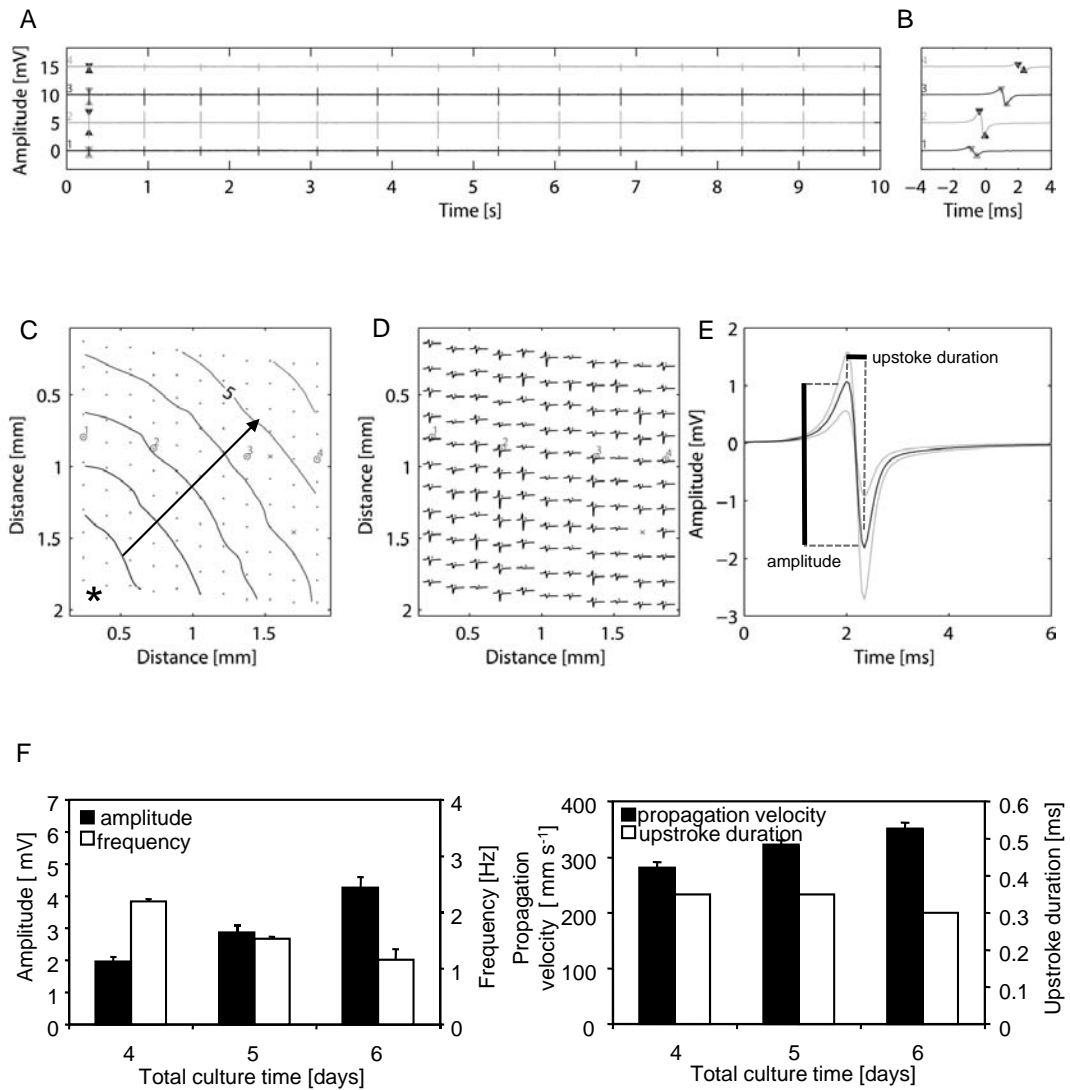


Figure 5.2: Electrogenic recordings of NRCml cultured for 5 days on HD-MEAs. (A) Long signal trace showing the synchronized contraction frequency and the field potential amplitude of NRCml over 10 seconds and a close-up of one burst in (B). The location of the four channels shown in (A-B) is marked in (C). (C) propagation pattern of an electrical wave showing the electrical activation origin (asterisk), the direction of the wave (arrow), and the location of the 126 electrodes (dots). The contour lines are in milliseconds. (D) Detailed activation map illustrating the average signal shape of the 126 electrodes for 10 seconds. (E) Average signal shape over all 126 channels. (F) Electrophysiological properties of wild-type NRCml over time. In this case the error bars represent the average from different recordings on one HD-MEA.

and the subsequent events on each channel was generated and then interpolated using a regular grid. A contour plot of such a map is shown in Figure 5.2C. The propagation velocity was then determined from the mean gradient of this map. Signal amplitude and upstroke duration were calculated from the signal shape averaged over all channels and all detected events, as shown in Figure 5.2D-E. The signal amplitude was taken as the difference between the maximum and the minimum averaged signal value. The upstroke duration was taken as the time difference between those two values.

5.2.5 Statistics

Standard deviations of all the parameter values have been calculated as well. The error bars shown in the figures, however, represent the variations of the mean values obtained from separate HD-MEAs with cells cultured under the same conditions to get an estimate for the reproducibility of culture-to-culture and HD-MEA-to-HD-MEA variability.

5.3 Results

5.3.1 HD-MEA-based electrophysiological analysis of neonatal rat cardiomyocytes

To monitor the electrophysiological properties of cardiomyocytes and to characterize HD-MEA-based electrophysiological results, we used NRCml placed on HD-MEAs (Fig. 5.1A-B). NRCml were positive for sarcomeric α -actinin and connexin 43 required for electrical coupling between the cells (Fig. 5.1C-D). A typical HD-MEA-based electrogram plot, generated during the spontaneous rhythm of contracting NRCml for four days in plating media, demonstrated tight temporal coupling over the culture at a frequency of 1.4 ± 0.05 Hz (Fig. 5.2A). Although electrogenic signals, recorded by extracellular electrodes, rely on local membrane currents of individual cardiomyocytes, the observed signal is modulated by the electrically coupled neighboring cells, so that local field potentials are recorded [Halbach et al., 2003, Hescheler et al., 2004]. Therefore, the first positive peak (positive voltage) represents a passive signal caused by the neighboring cells contracting earlier, while the following negative peak (negative voltage) shows the rapid depolarization phase (entrance of Na^+ ions) (Fig. 5.2B). As HD-MEAs simultaneously record extracellular potentials (field potentials) from 126 electrodes (Fig. 5.2D), it is possible to generate activation maps that show the impulse initiation, the direction of the excitation spread and propagation velocity (322 ± 8 mm/s) within the cultures (Fig. 5.2C). Figure 5.2D shows the average signal shape per channel aligned in time. As described by Halbach *et al.* the action potential (AP) parameters can be estimated from the field potential

(FP) [Halbach et al., 2003]. Based on these parameters, the average peak-to-peak amplitude was determined to 2.8 ± 1.3 mV (Fig. 5.2E). A similar correlation was obtained by [Spach et al., 1979]), where the duration of the AP upstroke (depolarization time) matched the time from maximum to minimum peak, which here corresponds to 0.35 ± 0.05 ms (Fig. 5.2E). Hence, the AP upstroke voltage gradient can be calculated as 8 V/s. After four days in culture NRCml started spontaneous beating. We monitored an increase in the amplitude of the electrical signal and in the velocity of the wave propagation, indicating that the level of membrane depolarization rises over time (Fig. 5.2F).

In order to evaluate the reliability of the recorded signals from HD-MEAs, we applied standard stimulators of the α - and β -adrenergic signaling cascade (phenylephrine and isoprenaline) and cardioactive drugs (lidocain and 4-aminopyridine). Although the responsiveness of cardiomyocytes to adrenergic drugs, such as adrenalin is controversial, they are known to increase the strength of cardiac contraction and the heart rate. When 10 μ M phenylephrine (PE), an α 1-adrenergic drug, were added to NRCml cultured on HD-MEA-based devices, a 2.5-fold increase in the beating frequency (positive chronotropic effect) was monitored 10 minutes after the addition [Fedida, 1993, Jahnel et al., 1994, Liu and Kennedy, 1998]. This effect was temporary and disappeared after 30 minutes in culture [Li et al., 1997, Xiao et al., 2004a] (Fig. 5.3A). Furthermore, upstroke duration increased, which can be attributed to the inhibition of a variety of K^+ currents [Fedida et al., 1991, Wagoner et al., 1996]. In contrast to PE, 10 nM isoprenaline (ISO), a β -adrenergic drug responsible for cAMP responses [Xiao et al., 2004a], enhanced the signal propagation velocity up to 2-fold, thus decreasing the upstroke duration [Banach et al., 2003, Hescheler et al., 2004] (Fig. 5.3B). The field potential amplitude increased up to 2.5-fold (positive inotropic effect) and beating frequency up to 2-fold [Godecke et al., 2001, Vandecasteele et al., 1999]. Application of the Na^+ channel blocker, lidocain (21 μ M) [Xue et al., 2005], led to a 7-fold decrease in field potential amplitude (negative inotropic effect), a 4-fold reduction in propagation velocity, and an increase of up to nine times in upstroke duration after two hours in culture [Halbach et al., 2006, Xiao et al., 2004b] (Fig. 5.3C). After adding 5 mM 4-aminopyridine, an unselective blocker of voltage-dependent K^+ channels [Ridley et al., 2003], the upstroke duration was nine times longer and the contractility was enhanced after 10 minutes in culture [Halbach et al., 2006, Wang and Duff, 1997] (Fig. 5.3D).

These results confirm that HD-MEA-based recordings reflect the electrophysiological properties of cardiomyocytes induced by the addition of known drugs, substantiating that this system can be used to assess the electrophysiological effects of drugs and genes.

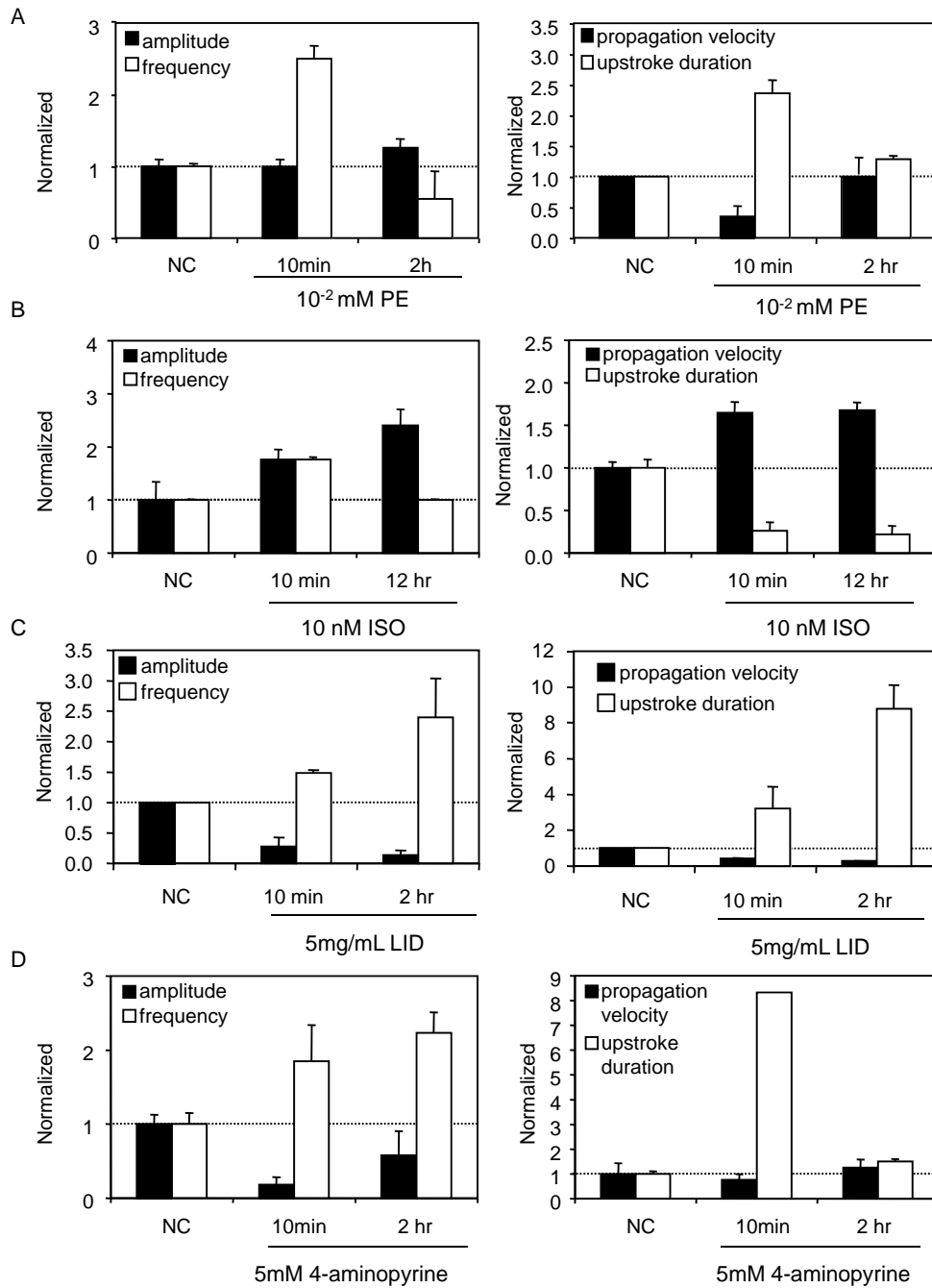


Figure 5.3: Electrophysiological reaction of wild-type NRCml (negative control, NC) incubated with (A) phenylephrine (PE, α 1-adrenergic agonist), (B) isoprenaline (ISO, β -adrenergic agonist), (C) lidocain (LID, blocker of Na^+ channels), and (D) 4-aminopyridine (blocker of the K^+ channels) for 10 minutes and two hours. Error bars represent the average from three independent measurements (HD-MEA-to-HD-MEA and NRC batch variability).

5.3.2 Modulation of the electrophysiology of neonatal rat cardiomyocytes by genetic manipulation

Capitalizing on the ability of HD-MEAs to characterize cardiac electrical signals we modulated cardiac electrophysiology and validated this system for gene/cell therapeutic applications. Freshly isolated cardiomyocytes were seeded on HD-MEAs and transduced with third-generation self-inactivating lentiviral particles.

After BMP-2 was expressed for 24 hours in NRCml, a higher contraction frequency and a lower action potential amplitude were recorded and confirmed using a HD-MEA (Fig. 5.4A). The activation map showed a clear decrease in the signal propagation velocity when BMP-2 was expressed. The upstroke duration increased in the presence of BMP-2 (Fig. 5.4A). In order to compare and quantify electrophysiological changes during BMP-2 expression, the average value of three independent cultures was normalized to that of a control HD-MEA containing negative control NRCml recorded under equivalent conditions. Whereas contraction frequency was up-regulated 4-fold in BMP-2-transduced NRCml, peak-to-peak amplitude was down-regulated 6-fold (Fig. 5.4B). Rhythm variability decreased in the presence of BMP-2 (NC; 25%, BMP-2; 8%). In addition, the signal propagation velocity was 3.5 times lower and the upstroke duration 12 times higher. EYFP-transduced cells showed no significant differences in basal contractility, suggesting that the electrophysiological changes were not due to transfection with the lentiviral particles (Fig. 5B). Moreover, BMP-2-transduced cells responded to an α -adrenergic stimulus of PE, thus leading to a three-fold increase in beating frequency and up to a 5-fold increase compared to PE alone (Fig. 5.4B). We also monitored the electrophysiological characteristics over time in order to evaluate the durability of the BMP-2-electrogenic effect (Fig. 5.4C). These results showed that an enhanced frequency and a reduced propagation velocity were maintained for up to five days. Importantly, after 48 hours of BMP-2 expression, peak-to-peak amplitude and upstroke duration were back to the values measured in negative control NRCml (NC) (Fig. 5.4C). This resulted in a slight reduction in the beating frequency and an increase in the velocity of signal propagation, which correlated with the electrophysiological properties of the negative control, NRCml, as previously observed (Fig. 5.2E). After one week of BMP-2 expression and a total of 10 days in culture, NRCml started to detach from the array surface, and the recordings were stopped (Fig. 5.4C).

5.3.3 Electrophysiological regulation of cardiac-like microtissue

Although monolayer cultures have been used so far as *in vitro* models to characterize the electrophysiology of cardiomyocytes, this culture type is not very representative for an *in vivo* structure. Previous experiments demonstrated that monodisperse cardiomyocytes, self-assembled in hanging drops, preserved their

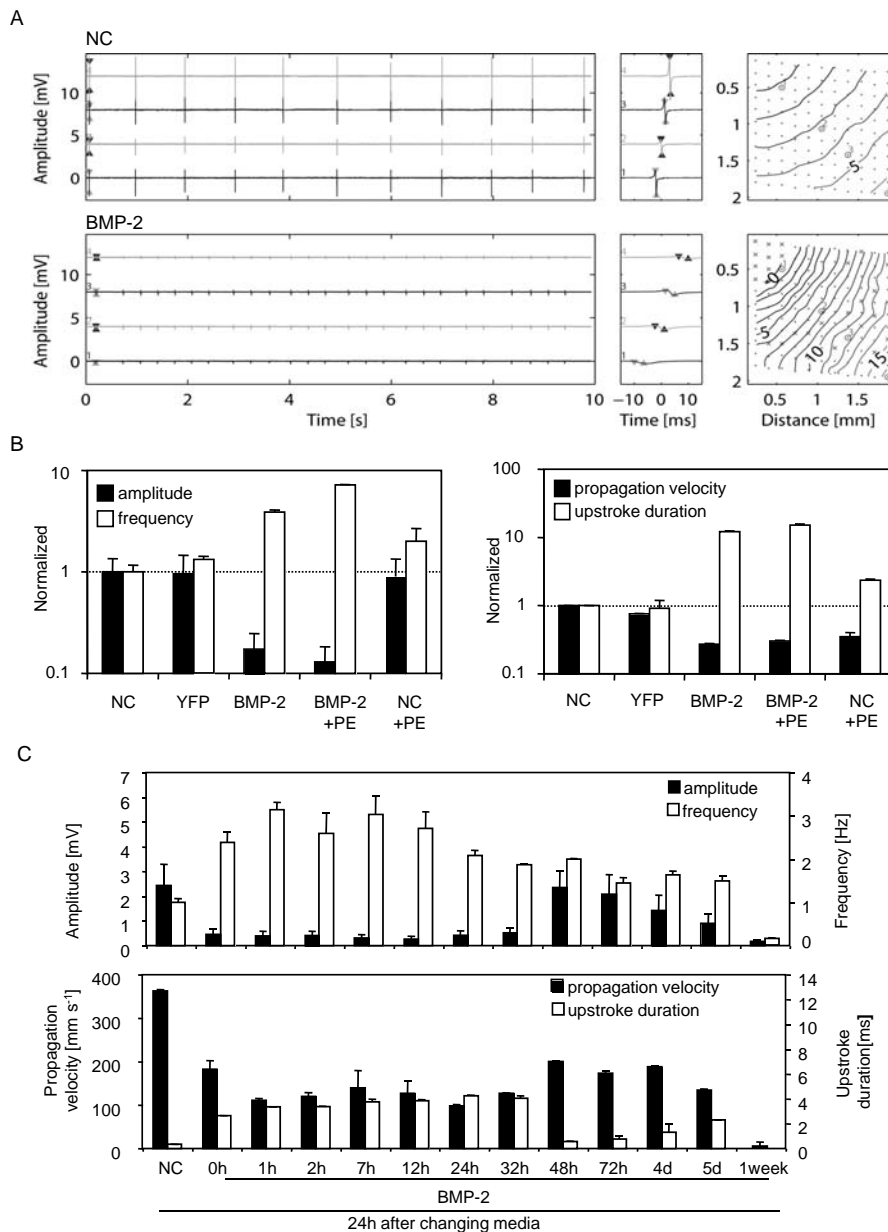


Figure 5.4: Electrophysiological characterization of genetically engineered NRCm1 for constitutive BMP-2 expression. (A) Long signal traces and wave propagation maps for wild-type (NC) and NRCm1 transduced with pBP253-derived lentiviral particles (BMP-2). (B) Plots of the field potential amplitude, frequency, signal propagation velocity and upstroke duration of NRCm1 transduced with pMF365-(YFP) or pBP253-(BMP-2) derived lentiviral particles. The data were normalized to negative control NRCm1 (NC). The y-axis is plotted on a logarithmic scale in order to visualize all values. (C) Plots showing the electrophysiological characteristics of cardiomyocytes constitutively expressing BMP-2 for 24 hr (0 hr) over time. Y-axes showing the recorded absolute values. Error bars represent the average of three independent measurements (HD-MEA-to-HD-MEA and NRC batch variability).

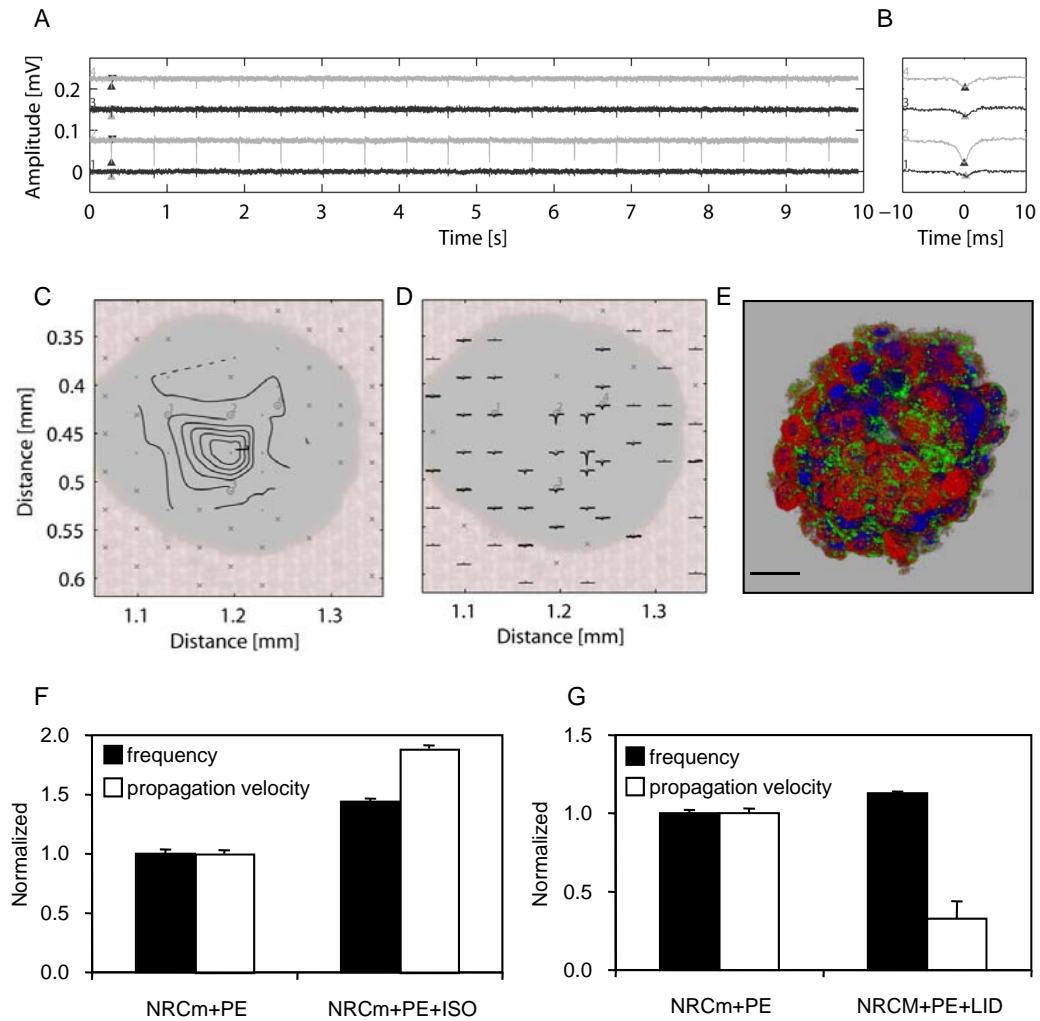


Figure 5.5: Electrophysiological characterization of neonatal rat cardiomyocyte microtissues (NRCmt). (A) Long signal traces showing synchronized beating frequency and the field potential amplitude recorded from different electrodes located under the NRCmt. (B) Close-up into one wave. (C) Propagation pattern of an electrical wave within the NRCmt. The contour lines represent 0.2 milliseconds. (D) Average signal shape of each electrode adjacent to the NRCmt. (E) Immunofluorescence-based characterization of a 5-day old NRCmt. Morphology and electrical coupling within the NRCmt was visualized by immunohistologic staining specific for sarcomeric α -actinin (red), 4'-6-diamidino-2-phenylindole (DAPI) (blue) and connexin 43 (green, arrows). Scale bar 50 μ m. (F-G) Electrophysiological reaction of NRCmt cultured in media supplemented with 10^2 M phenylephrine (PE) and incubated for 10 minutes with (F) 10 nM isoprenaline (ISO) or (G) 5 mg/ml lidocain (LID). Error bars represent the average from a minimum of three independent measurements (NRCmt-to-NRCmt variability).

cardiomyocyte-specific cell phenotype, intramicrotissue superstructures, and extracellular matrix [Kelm et al., 2004a]. In this study we used myocardial microtissues (NRCmt) to monitor the electrophysiology of cardiac-like tissue and the BMP-2 cardiogenic effect in the whole tissue. For future high-throughput drug/gene screening applications using 3D cultures, we scaled up NRCmt production using a novel robotic microtissue assembly module enabling serial formation of scaffold-free microtissues. Four-day old NRCmt were cultured in plating media supplemented with PE on HD-MEAs, previously coated with laminin. After five minutes, NRCmt started rhythmic contraction and after six hours the beating frequencies reached 100 ± 40 bpm (beatings per minute) (Fig 5.5A). NRCmt did not initiate contraction or rhythmic beats in the absence of hormonal stimuli [Kelm et al., 2004a]. The field potential signal shape included only one negative peak (negative voltage), suggesting that the origin of the excitation was close to the recording area (Fig. 5.5B). The electrical signals enabled us to plot a two-dimensional representation of the wave propagation in cardiac microtissues (Fig. 5.5C). Activation maps show the location and the field potential shape of electrically active cells that were integrated into a three-dimensional cardiac extracellular matrix (Fig. 5.5D) This observation confirmed electrophysiological coupling among the cardiomyocytes embedded in an artificial microtissue structure [Kelm et al., 2006], which correlates to the high number of gap junctions visualized by confocal microscopy (Fig. 5.5E). In order to validate the effect of known cardiogenic hormones/drugs on NRCmt, we first added 10^{-2} mM PE and one hour later, we applied (i) ISO or (ii) LID for 10 minutes. We analyzed the contraction frequency and the signal propagation velocity from different NRCmts. Field potential amplitude and upstroke duration were not considered due to the variability in the adhesion of the microtissues to the array surface, which directly influences the electrical potential values. Addition of 10 nM ISO increased the beating frequency of the microtissue and enhanced the signal propagation velocity through the tissue (Fig. 8F), while the application of 5 mg/ml Lid decreased the field potential propagation velocity (Fig. 5.5G). This demonstrates that 3D cultures also show the drug-induced effects and that corresponding changes in electrical activity can be assessed using HD-MEAs.

5.4 Discussion

The physiological control of cells and tissues remains one of the greatest challenges for molecular and cellular biologists which, if overcome, promises a wide variety of therapeutic applications. To this end, the control and restoration of the electrophysiological functions of cardiac tissue is today one of the central aims of cardiovascular medicine and research [Kusumoto and Goldschlager, 1996]. We have shown here the ability to regulate cardiac electrophysiology by means of synthetic gene control systems responsive to external factors such as antibiotics. We have explored this approach by extensively analyzing electrophysiological

changes in freshly isolated neonatal rat cardiomyocytes cultured on HD-MEAs. We also established HD-MEA-based devices as means to evaluate field potential properties, such as the upstroke duration and the depolarization amplitude, which were previously demonstrated to correlate with changes in action potentials [Halbach et al., 2003]. Moreover, the field potential signal shapes indicated the presence of previously excited cells. While a positive followed by a negative peak indicates the presence of previously excited cells, a negative peak only indicates the absence of previously excited cells, thus designating the origin of excitation region. Signal propagation velocities, localization of the origin of excitation, and contraction rate were also assessed. Overall, the electrophysiological control of cardiac cells in HD-MEAs offers the possibility to measure functional effects in real time, and thus constitute a ready-to-use tool for gene-function studies and for future discovery and preclinical evaluation of novel genes with potential therapeutic effects.

At present, tissue transplantation and insertion of electrical pacemakers are the clinical solutions offered to treat cardiac dysfunction. As cardiac-related insufficiencies are the major cause of death in industrialized countries [Hennekens, 1998], new technologies are required to regenerate cardiac tissue functionality [Dowell et al., 2003], such as (i) stem cell transplantation [Strauer et al., 2002], (ii) active myogenic cell transplantation [SoRelle, 2000], or (iii) implantation of biologic pacemakers [Robinson et al., 2006, Rosen et al., 2004]. The efficient delivery and adjustable expression of therapeutic genes might also be required to cure common disorders. Therefore, regulation systems, in which the expression of one or more selected therapeutic transgenes can be controlled, represent an attractive approach to improve/restore cardiac tissue functionality. We have been able to control cardiac electrical activity of cardiomyocytes by using lentivectors engineered for streptogramin-responsiveness [Fussenegger et al., 2000, Mitta et al., 2004]. Lentiviral particles successfully transduced non-dividing cardiomyocytes without disturbing the electrophysiological behavior of the cells. The pristinamycin I (PI) controllable system exhibited (i) a change of up to 12-fold in electrophysiological activity (upstroke duration) in the induced (absence of PI) state, (ii) a side-effect-free state (no effect seen in negative controls) under repressed conditions, (iii) fine-tuning of electrophysiological changes through intermediate PI dosing, and (iv) a design compatible with lentiviral delivery systems, thus meeting the requirements of future clinical implementations.

Today's strategies for drug/gene discovery also require fast and easy-to-use test methods that mimic the human tissue environment in order to optimize pre-clinical selection of the most active molecules from a large pool of potential effectors. Although 3D cultures better reflect the *in vivo* behavior of most cell types, these 3D test systems have not yet been incorporated into the mainstream drug development operations [Kunz-Schughart et al., 2004]. We have recorded the electrogenic activity in myocardial microtissues, which reproduced the *in vivo* electrogenic effect of known cardioactive drugs. This suggests that these microtissues and the HD-MEAs might provide an ex-vivo feasible assay to determine

cardiac excitation patterns for the screening of potential therapeutic molecules and as a pre-implantation quality control. The feasibility of a 3D platform to assess cardiac functionality was confirmed by the impact of regulable BMP-2 expression. BMP-2-transduced NRCmt showed a coordinated beating. Microtissues transgenic for BMP-2 did not require a hormonal stimulus as it is the case for wild-type microtissues, demonstrating that BMP-2 is a relevant molecule for cardiac cell activity, which is able to restore cardiac electrical activity. Controlled production of BMP-2-transduced NRCmt in the absence of a repressing molecule (pristinamycin-inducible system) or in the presence of the inducer (acetaldehyde-inducible system) also restored NRCmt electrical activity. This demonstrates the functionality of these inducible systems for a 3D culture, which inherently reflects *in vivo* functioning more accurately.

The ability to engineer cell and tissue electrophysiology will foster great advances in the understanding of cardiac cell behavior and in the development of novel therapies to treat cardiac contractility disorders. In particular, BMP-2 might represent a therapeutic molecule for the recovery of cardiomyocyte function, when mechanical contractility is the cause of reduced heart function. We have, for the first time, demonstrated the ability to regulate cardiac electrophysiology by biocompatible inducers, which can adjust the therapeutic transgene expression level, and thus fine-tune the electrical activity of cardiac cells. Moreover, we have been able to restore the cardiac contractility from myocardial-like microtissues. Finally, the approach detailed here may represent an ex-vivo assay to determine cardiac excitation patterns for (i) pre-clinical and experimental electrophysiological tests and (ii) novel gene function studies.

Acknowledgements

We thank Evelyne Perriard, Anna Bogdanova and Nikolai Bogdanov for providing neonatal rat cardiomyocytes and advice, Francesca Faraci for help with the data analysis, Frauke Greve for technical support, Shizuka Hartenbach for providing pSH16 prior to publication and David Greber for critical comments on the manuscript. This work was supported by an ETH-internal grant TH-1-03-1, by the Swiss National Science foundation (grant no. 3100A0-112549) and the EC Framework 7 (COBIOS).

Chapter 6

Conclusion & Outlook

The design, fabrication, system integration and operation of a high-density microelectrode array integrated in CMOS-technology was demonstrated. It was shown that an analog switch matrix provides a suitable solution for achieving a high spatial resolution while maintaining low noise levels. Electrical measurements showed the full functionality of the device. The measurement setup was described and tested. Biological measurements of neonatal rat cardiomyocytes, of cultured rat hippocampal neurons, of chicken retina (data not shown) and of acute rat cerebellum preparations have been successfully conducted.

Two thirds of this part of thesis were focused on applications of the developed technology, since, obtaining the first silicon chip is only a little step towards a fully functional system. Electrical testing has to be performed, a data acquisition system has to be developed, the biocompatible packaging poses a major challenge, and, most importantly a lot of software engineering is required. The design and operability of this system is largely depending on software: 1) The switch matrix cannot be designed without software that generates schematics, the layout and provides a golden model for testing; 2) The switch matrix shifts hardware challenges to software, it cannot be operated without dedicated algorithms for the routing and without the real time generation and stepping of configurations. Also the software has to hide the complexity of the electrode selection process to the user; 3) Recording at high temporal resolution from many channels inherently generates a lot of data that must be handled; 4) Software that extracts information from the raw data traces is crucial, as the naked eye cannot recognize and distinguish the highly complex patterns generated by the neurons.

Although the section on the applications is a large fraction of this thesis, it represents only a very small fraction of possible device applications. Does the high resolution and the resulting more comprehensive recordings of neuronal activity provide deeper insights into learning mechanisms and plasticity of neuronal cells in culture? Can we follow neuronal migration in cultures and correlate it to the electrical activity of the cells? Can we record from different acute slice

preparations as easily as from the cerebellum? Can the data lead to more detailed compartment models of cells that precisely reproduce the extracellular fields, and can those models be used to identify cell types according to their extracellular fields? These are only a few open questions. In this thesis only the first steps of a description of the device, a short outline of its potential and possibilities in new applications, and a demonstration of its capabilities has been demonstrated. An obvious next step is to make this device available to other researchers, e.g., within the framework of new interdisciplinary projects, or to initiate a commercial exploitation of the technology.

Chapter 7

HD-MEA Bibliography

- A. Abbott. Cell culture: biology's new dimension. *Nature*, 424(6951):870–872, Aug 21 2003.
- E. Abdelwahid, D. Rice, L. J. Pelliniemi, and E. Jokinen. Overlapping and differential localization of bmp-2, bmp-4, msx-2 and apoptosis in the endocardial cushion and adjacent tissues of the developing mouse heart. *Cell Tissue Res*, 305(1):67–78, Jul 2001.
- W. Akemann and T. Knopfel. Interaction of Kv3 potassium channels and resurgent sodium current influences the rate of spontaneous firing of Purkinje neurons. *J. Neurosci.*, 26(17):4602–4612, 2006.
- B. T. Atherton, D. M. Meyer, and D. G. Simpson. Assembly and remodelling of myofibrils and intercalated discs in cultured neonatal rat heart cells. *J. Cell Sci.*, 86:233–248, Dec 1986.
- D. Auerbach, S. Bantle, S. Keller, V. Hinderling, M. Leu, E. Ehler, and J. C. Perriard. Different domains of the m-band protein myomesin are involved in myosin binding and m-band targeting. *Mol Biol Cell*, 10(5):1297–1308, May 1999.
- K. Banach, M. D. Halbach, P. Hu, J. Hescheler, and U. Egert. Development of electrical activity in cardiac myocyte aggregates derived from mouse embryonic stem cells. *Am J Physiol Heart Circ Physiol*, 284(6):2114–2123, Jun 2003.
- C. Bedard, H. Kroger, and A. Destexhe. Model of low-pass filtering of local field potentials in brain tissue. *Physical Review E (Statistical, Nonlinear, and Soft Matter Physics)*, 73(5):051911, 2006.
- John M. Bekkers and Michael Hausser. Targeted dendrotomy reveals active and passive contributions of the dendritic tree to synaptic integration and neuronal output. *PNAS*, 104(27):11447–11452, 2007.
- L. Berdondini, P.D. Van der Wal, O. Guenat, N.F. de Rooij, M. Koudelka-Hep, P. Seitz, R. Kaufmann, P. Metzler, N. Blanc, and S. Rohr. High-density electrode array for imaging in vitro electrophysiological activity. *Biosensors Bioelectronics*, 21:167–174, 2005.
- T. J. Blanche, M. A. Spacek, J. F. Hetke, and N. V. Swindale. Polytrodes: High-Density Silicon Electrode Arrays for Large-Scale Multiunit Recording. *J Neurophysiol*, 93(5):2987–3000, 2005.
- T. Boiko, A. Van Wart, J. H. Caldwell, S. R. Levinson, J. S. Trimmer, and G. Matthews. Functional Specialization of the Axon Initial Segment by Isoform-Specific Sodium Channel Targeting. *J. Neurosci.*, 23(6):2306–2313, 2003.

- G. Buzsaki. Large-scale recording of neuronal ensembles. *Nat Neurosci*, 7:446–451, May 2004. 10.1038/nn1233.
- K. Chien. Making a play at regrowing hearts. *The Scientist*, 20(6), 2006.
- S. Chlopčikova, J. Psotova, and P. Míketova. Neonatal rat cardiomyocytes a model for the study of morphological, biochemical and electrophysiological characteristics of the heart. *Biomed Pap Med Fac Univ Palacky Olomouc Czech Repub*, 145(2):49–55, Dec 2001.
- J. N. Cohn, M. R. Bristow, K. R. Chien, W. S. Colucci, O. H. Frazier, L. A. Leinwand, B. H. Lorell, A. J. Moss, E. H. Sonnenblick, R. A. Walsh, S. C. Mockrin, and L. Reinlib. Report of the national heart, lung, and blood institute special emphasis panel on heart failure research. *Circulation*, 95(4):766–770, Feb 18 1997.
- M. A. Crackower, G. Y. Oudit, I. Kozieradzki, R. Sarao, H. Sun, T. Sasaki, E. Hirsch, A. Suzuki, T. Shioi, J. Irie-Sasaki, R. Sah, H. Y. Cheng, V. O. Rybin, G. Lembo, L. Fratta, A. J. Oliveira dos Santos, J. L. Benovic, C. R. Kahn, S. Izumo, S. F. Steinberg, M. P. Wymann, P. H. Backx, and J. M. Penninger. Regulation of myocardial contractility and cell size by distinct pi3k-pten signaling pathways. *Cell*, 110(6):737–749, Sep 20 2002.
- J. Csicsvari, D. A. Henze, B. Jamieson, K. D. Harris, A. Sirota, P. Bartho, K. D. Wise, and G. Buzsaki. Massively parallel recording of unit and local field potentials with silicon-based electrodes. *J Neurophysiol*, 90(2):1314–1323, 2003.
- D. A. Datwyler, J. P. Magyar, V. Busceti, A. Hirschy, J. C. Perriard, J. E. Bailey, and H. M. Eppenberger. Recombinant sindbis virus allows expression and precise targeting of proteins of the contractile apparatus in cultured cardiomyocytes. *Basic Res Cardiol*, 96(6):630–635, Nov 2001.
- R. Lorente de No. Analysis of the distribution of action currents of nerve in volume conductors. *Studies Rockefeller Inst. Med. Res.*, 132:384–477, 1947.
- T. Delbruck and C.A. Mead. Adaptive photoreceptor with wide dynamic range. *Proc. IEEE International Symposium on Circuits and Systems (ISCAS'94)*, 4:339–342, 1994.
- A. Destexhe and D. Pare. Impact of Network Activity on the Integrative Properties of Neocortical Pyramidal Neurons In Vivo. *J Neurophysiol*, 81(4):1531–1547, 1999.
- J. D. Dowell, M. Rubart, K. B. Pasumarthi, M. H. Soonpaa, and L. J. Field. Myocyte and myogenic stem cell transplantation in the heart. *Cardiovasc Res*, 58(2):336–350, May 1 2003.
- U. Egert, Heck, and Aertsen. Two-dimensional monitoring of spiking networks in acute brain slices. *Experimental Brain Research*, 142:268–274, January 2002.
- B. Eversmann, M. Jenkner, F. Hofmann, C. Paulus, R. Brederlow, B. Holzapfl, P. Fromherz, M. Merz, M. Brenner, M. Schreiter, R. Gabl, K. Plehnert, M. Steinhauser, G. Eckstein, D. Schmitt-Landsiedel, and R. Thewes. A 128 x 128 CMOS biosensor array for extracellular recording of neural activity. *IEEE Journal of Solid-State Circuits*, 38:2306–2317, 2003a.
- D. Fedida. Modulation of cardiac contractility by alpha 1 adrenoceptors. *Cardiovasc Res*, 27(10):1735–1742, Oct 1993.
- D. Fedida, A. P. Braun, and W. R. Giles. Alpha 1-adrenoceptors reduce background k⁺ current in rabbit ventricular myocytes. *J Physiol*, 441:673–684, Sep 1991.

- S. Fennrich, H. Stier, K.J. Foehr, D. Ray, J.F. Ghersi Egea, and B. Schlosshauer. Organotypic rat brain culture as in vivo-like model system. *Methods in Cell Science*, 18:283–291, 1996.
- W. Franks. *Towards Monolithic CMOS Cell-based Biosensors*. Ph.D. Thesis, No. 15990, ETH Zurich, Zurich, 2005.
- U. Frey, F. Heer, R. Pedron, F. Greve, S. Hafzovic, K.-U. Kirstein, and A. Hierlemann. 11'000 electrode-, 126 channel-CMOS microelectrode array for electrogenic cells. In *MEMS 2007*, pages 541–544, Kobe, Japan, 2007b. ISBN 1-4244-0950-0.
- U. Frey, F. Heer, R. Pedron, S. Hafzovic, F. Greve, J. Sedivy, K. U. Kirstein, and A. Hierlemann. An 11k-electrode 126-channel high-density microelectrode array to interact with electrogenic cells. In *Solid-State Circuits Conference, 2007. ISSCC 2007. Digest of Technical Papers. IEEE International*, pages 158–159, San Francisco, California, 2007c.
- U. Frey, C.D. Sanchez-Bustamante, T. Ugniwenko, F. Heer, J. Sedivy, S. Hafzovic, B. Roscic, M. Fussenegger, A. Blau, U. Egert, and A. Hierlemann. Cell Recordings with a CMOS High-density Microelectrode Array. In *Proceedings of the 29th Annual International Conference of the IEEE EMBS*, pages 167–170, Lyon, France, 2007d. ISBN 1-4244-0788-5.
- M. Fussenegger. The impact of mammalian gene regulation concepts on functional genomic research, metabolic engineering, and advanced gene therapies. *Biotechnol. Prog.*, 17(1):1–51, Jan-Feb 2001.
- M. Fussenegger, S. Schlatter, D. Datwyler, X. Mazur, and J. E. Bailey. Controlled proliferation by multigene metabolic engineering enhances the productivity of chinese hamster ovary cells. *Nat. Biotechnol.*, 16(5):468–472, May 1998.
- M. Fussenegger, R. P. Morris, C. Fux, M. Rimann, B. von Stockar, C. J. Thompson, and J. E. Bailey. Streptogramin-based gene regulation systems for mammalian cells. *Nat. Biotechnol.*, 18(11):1203–1208, Nov 2000.
- C. Fux, D. Langer, and M. Fussenegger. Dual-regulated myod- and msx1-based interventions in c2c12-derived cells enable precise myogenic/osteogenic/adipogenic lineage control. *J Gene Med*, 6(10):1159–1169, Oct 2004a.
- C. Fux, B. Mitta, B. P. Kramer, and M. Fussenegger. Dual-regulated expression of c/ebp-alpha and bmp-2 enables differential differentiation of c2c12 cells into adipocytes and osteoblasts. *Nucleic Acids Res*, 32(1):e1, 2004b.
- D. Galaris, B. Hoijer, and J. Rydstrom. Improved methods for automatic monitoring of contracting heart cells in culture. *J Biochem Biophys Methods*, 2(4):213–225, Apr 1980.
- S. Gambit. New approaches to antiarrhythmic therapy: emerging therapeutic applications of the cell biology of cardiac arrhythmias(1). *Cardiovasc Res*, 52(3):345–360, Dec 2001.
- G. Gholmieh, W. Soussou, M. Han, A. Ahuja, M.C. Hsiao, D. Song, A.R. Tanguay, Jr, and T.W. Berger. Custom-designed high-density conformal planar multielectrode arrays for brain slice electrophysiology. *J Neurosci Methods*, 152(1-2):116–129, 2006.
- N. Ghosh-Choudhury, S. L. Abboud, B. Chandrasekar, and G. G. Choudhury. Bmp-2 regulates cardiomyocyte contractility in a phosphatidylinositol 3 kinase-dependent manner. *FEBS Lett.*, 544(1-3):181–184, Jun 5 2003a.

- N. Ghosh-Choudhury, S. L. Abboud, L. Mahimainathan, B. Chandrasekar, and G. G. Choudhury. Phosphatidylinositol 3-kinase regulates bone morphogenetic protein-2 (bmp-2)-induced myocyte enhancer factor 2a-dependent transcription of bmp-2 gene in cardiomyocyte precursor cells. *J. Biol. Chem.*, 278(24):21998–22005, Jun 13 2003b.
- W. Gobel, B. M. Kampa, and F. Helmchen. Imaging cellular network dynamics in three dimensions using fast 3d laser scanning. *Nat Meth*, 4:73–79, January 2007. ISSN 1548-7091. 10.1038/nmeth989.
- A. Godecke, T. Heinicke, A. Kamkin, I. Kiseleva, R. H. Strasser, U. K. Decking, T. Stumpe, G. Isenberg, and J. Schrader. Inotropic response to beta-adrenergic receptor stimulation and anti-adrenergic effect of ach in endothelial no synthase-deficient mouse hearts. *J Physiol*, 532(Pt 1):195–204, Apr 1 2001.
- C. Gold, D. A. Henze, C. Koch, and G. Buzsaki. On the Origin of the Extracellular Action Potential Waveform: A Modeling Study. *J Neurophysiol*, 95(5):3113–3128, 2006.
- C. Gold, D. Henze, and C. Koch. Using extracellular action potential recordings to constrain compartmental models. *Journal of Computational Neuroscience*, 23:39–58, August 2007. 10.1007/s10827-006-0018-2.
- H. Gray. *Anatomy of the Human Body*. Lea & Febiger, 1918.
- G.W. Gross, B.K. Rhoades, H.M.E. Azzazy, and W. Ming-Chi. The use of neuronal networks on multielectrode arrays as biosensors. *Biosens. Bioelectron.*, 10:553–567, 1995.
- S. Hafizovic. *Neural Interface and Atomic-Force Microscope in CMOS Technology*. Ph.D. Thesis, No. 16806, ETH Zurich, Zurich, 2006a.
- M. Halbach, U. Egert, J. Hescheler, and K. Banach. Estimation of action potential changes from field potential recordings in multicellular mouse cardiac myocyte cultures. *Cell Physiol Biochem*, 13(5):271–284, 2003.
- M. Halbach, F. Pillekamp, K. Brockmeier, J. Hescheler, J. Muller-Ehmsen, and M. Reppel. Ventricular slices of adult mouse hearts a new multicellular in vitro model for electrophysiological studies. *Cell. Physiol. Biochem.*, 18(1-3):1–8, 2006.
- I. Harary and B. Farley. In vitro studies on single beating rat heart cells. i. growth and organization. *Exp Cell Res*, 29:451–465, Feb 1963a.
- I. Harary and B. Farley. In vitro studies on single beating rat heart cells. ii. intercellular communication. *Exp Cell Res*, 29:466–474, Feb 1963b.
- K. D. Harris, D. A. Henze, J. Csicsvari, H. Hirase, and G. Buzsaki. Accuracy of Tetrode Spike Separation as Determined by Simultaneous Intracellular and Extracellular Measurements. *J Neurophysiol*, 84(1):401–414, 2000.
- R.R. Harrison and C. Charles. A low-power low-noise CMOS amplifier for neural recording applications. *IEEE Journal of Solid-State Circuits*, 38:958–965, 2003.
- S. Hartenbach and M. Fussenegger. Autoregulated, bidirectional and multicistronic gas-inducible mammalian as well as lentiviral expression vectors. *J. Biotechnol.*, 120(1):83–98, Oct 17 2005.
- D. Heck. Rat cerebellar cortex in vitro responds specifically to moving stimuli. *Neuroscience Letters*, 157:95–98, July 1993.

- F. Heer. *CMOS-based Microelectrode Array for Communication with Electrogenic Cells*. Ph.D. Thesis, No. 16330, ETH Zurich, Zurich, 2005.
- F. Heer, S. Hafizovic, W. Franks, A. Blau, C. Ziegler, and A. Hierlemann. Cmos microelectrode array for bidirectional interaction with neuronal networks. *Solid-State Circuits, IEEE Journal of*, 41:1620–1629, 2006a.
- F. Heer, S. Hafizovic, T. Ugniwenko, U. Frey, W. Franks, E. Perriard, J. C. Perriard, A. Blau, C. Ziegler, and A. Hierlemann. Single-chip microelectronic system to interface with living cells. *Biosens. Bioelectron.*, 22:2546–2553, May 2007a.
- C. H. Hennekens. Increasing burden of cardiovascular disease: current knowledge and future directions for research on risk factors. *Circulation*, 97(11):1095–1102, Mar 24 1998.
- J. Hescheler, M. Halbach, U. Egert, Z. J. Lu, H. Bohlen, B. K. Fleischmann, and M. Reppel. Determination of electrical properties of es cell-derived cardiomyocytes using meas. *Journal of Electrocardiology*, 37(59):110–116, October 2004.
- M.L. Hines and N.T. Carnevale. The neuron simulation environment. *Neural Computation*, 9:1179–1209, 1997.
- B. L. Hogan. Bone morphogenetic proteins: multifunctional regulators of vertebrate development. *Genes Dev*, 10(13):1580–1594, Jul 1 1996.
- G. R. Holt and C. Koch. Electrical interactions via the extracellular potential near cell bodies. *J Comput Neurosci*, 6(2):169–184, 1999.
- A. Hyvarinen. Fast and robust fixed-point algorithms for independent component analysis. *Neural Networks, IEEE Transactions on*, 10:626–634, 1999. ISSN 1045-9227.
- M. Izumi, Y. Fujio, K. Kunisada, S. Negoro, E. Tone, M. Funamoto, T. Osugi, Y. Oshima, Y. Nakaoka, T. Kishimoto, K. Yamauchi-Takahara, and H. Hirota. Bone morphogenetic protein-2 inhibits serum deprivation-induced apoptosis of neonatal cardiac myocytes through activation of the smad1 pathway. *J. Biol. Chem.*, 276(33):31133–31141, Aug 17 2001.
- U. Jahnel, E. Duwe, S. Pfennigsdorf, and H. Nawrath. On the mechanism of action of phenylephrine in rat atrial heart muscle. *Naunyn-Schmiedeberg's Arch. Pharmacol.*, 349(4):408–415, Apr 1994.
- Y. Jimbo and H.P.C. Robinson. Propagation of spontaneous synchronized activity in cortical slice cultures recorded by planar electrode arrays. *Bioelectrochemistry*, 51:107–115, 6 2000.
- J. Johansen, C. Rosenblad, K. Andsberg, A. Moller, C. Lundberg, A. Bjorlund, and T. E. Johansen. Evaluation of tet-on system to avoid transgene down-regulation in ex vivo gene transfer to the cns. *Gene Ther*, 9(19):1291–1301, Oct 2002.
- M. T. Keating and M. C. Sanguinetti. Molecular genetic insights into cardiovascular disease. *Science*, 272(5262):681–685, May 3 1996.
- I. Kehat, L. Khimovich, O. Caspi, A. Gepstein, R. Shofti, G. Arbel, I. Huber, J. Satin, J. Itskovitz-Eldor, and L. Gepstein. Electromechanical integration of cardiomyocytes derived from human embryonic stem cells. *Nat. Biotechnol.*, 22(10):1282–1289, Oct 2004.
- J. M. Kelm, E. Ehler, L. K. Nielsen, S. Schlatter, J. C. Perriard, and M. Fussenegger. Design of artificial myocardial microtissues. *Tissue Eng.*, 10(1-2):201–214, Jan-Feb 2004a.

- J. M. Kelm, B. P. Kramer, V. Gonzalez-Nicolini, B. Ley, and M. Fussenegger. Synergies of microtissue design, viral transduction and adjustable transgene expression for regenerative medicine. *Biotechnol. Appl. Biochem.*, 39(Pt 1):3–16, Feb 2004b.
- J. M. Kelm, V. Djonov, S. P. Hoerstrup, C. I. Guenter, L. M. Ittner, F. Greve, A. Hierlemann, C. D. Sanchez-Bustamante, J. C. Perriard, E. Ehler, and M. Fussenegger. Tissue-transplant fusion and vascularization of myocardial microtissues and macrotissues implanted into chicken embryos and rats. *Tissue Eng.*, 12(9):2541–2553, Sep 2006.
- J.M. Kelm, N.E. Timmins, C.J. Brown, M. Fussenegger, and L.K. Nielsen. Method for generation of homogeneous multicellular tumor spheroids applicable to a wide variety of cell types. *Biotechnol Bioeng*, 83(2):173–180, 2003.
- J.M. Kelm, E. Ehler, L.K. Nielsen, S. Schlatter, J.C. Perriard, and M. Fussenegger. Design of artificial myocardial microtissues. *Tissue Eng.*, 10(1-2):201–214, 2004c.
- Z. M. Khaliq, N. W. Gouwens, and I. M. Raman. The Contribution of Resurgent Sodium Current to High-Frequency Firing in Purkinje Neurons: An Experimental and Modeling Study. *J. Neurosci.*, 23(12):4899–4912, 2003.
- M. Klee and W. Rall. Computed potentials of cortically arranged populations of neurons. *J Neurophysiol*, 40(3):647–666, 1977.
- M. H. P. Kole, J. J. Letzkus, and G. J. Stuart. Axon initial segment kv1 channels control axonal action potential waveform and synaptic efficacy. *Neuron*, 55:633–647, August 2007.
- M. H. P. Kole, S. U. Ilschner, B. M. Kampa, S. R. Williams, P. C. Ruben, and G. J. Stuart. Action potential generation requires a high sodium channel density in the axon initial segment. *Nat Neurosci*, 11:178–186, February 2008. ISSN 1097-6256. 10.1038/nm2040.
- J. K. Koponen, H. Kankkonen, J. Kannasto, T. Wirth, W. Hillen, H. Bujard, and S. Yla-Herttuala. Doxycycline-regulated lentiviral vector system with a novel reverse transactivator rtta2s-m2 shows a tight control of gene expression in vitro and in vivo. *Gene Ther*, 10(6):459–466, Mar 2003.
- G.T.A. Kovacs. Electronic sensors with living cellular components. *Proceedings of the IEEE*, 91:915–929, 2003.
- L. A. Kunz-Schughart, J. P. Freyer, F. Hofstaedter, and R. Ebner. The use of 3-d cultures for high-throughput screening: the multicellular spheroid model. *J Biomol Screen*, 9(4):273–285, Jun 2004.
- F. M. Kusumoto and N. Goldschlager. Cardiac pacing. *N Engl J Med*, 334(2):89–97, Jan 11 1996.
- H. C. Kwan and J. T. Murphy. A basis for extracellular current density analysis in cerebellar cortex. *J Neurophysiol*, 37(1):170–180, 1974.
- F. Lehmann-Horn and K. Jurkat-Rott. Voltage-gated ion channels and hereditary disease. *Physiol Rev*, 79(4):1317–1372, Oct 1999.
- Michael S Lewicki. A review of methods for spike sorting: the detection and classification of neural action potentials. *Comput. Neural Syst.*, pages 53–78, 9 1998.
- K. Li, H. He, C. Li, P. Sirois, and J. L. Rouleau. Myocardial alpha1-adrenoceptor: inotropic effect and physiologic and pathologic implications. *Life Sci.*, 60(16):1305–1318, 1997.

- S. J. Liu and R. H. Kennedy. α 1-adrenergic activation of l-type ca current in rat ventricular myocytes: perforated patch-clamp recordings. *Am J Physiol*, 274(6 Pt 2):H2203–7, Jun 1998.
- Z. F. Mainen, J. Joerges, J. R. Huguenard, and T. J. Sejnowski. A model of spike initiation in neocortical pyramidal neurons. *Neuron*, 15:1427–1439, December 1995.
- S. Marom and G. Shahaf. Development, learning and memory in large random networks of cortical neurons: lessons beyond anatomy. *Quarterly Reviews Of Biophysics*, 35:63–87, 2002.
- M. Masaki, M. Izumi, Y. Oshima, Y. Nakaoka, T. Kuroda, R. Kimura, S. Sugiyama, K. Terai, M. Kitakaze, K. Yamauchi-Takahara, I. Kawase, and H. Hirota. Smad1 protects cardiomyocytes from ischemia-reperfusion injury. *Circulation*, 111(21):2752–2759, May 31 2005.
- T. Meyer, C. Leisgen, B. Gonser, and E. Guenther. Qt-screen: High-throughput cardiac safety pharmacology by extracellular electrophysiology on primary cardiac myocytes. *ASSAY and Drug Development Technologies*, 2(5):507–515, 2004.
- M. Migliore and G. M. Shepherd. Emerging rules for the distributions of active dendritic conductances. *Nat Rev Neurosci*, 3:362–370, May 2002. ISSN 1471-003X. 10.1038/nrn810.
- B. Mitta, M. Rimann, M. U. Ehrenguber, M. Ehrbar, V. Djonov, J. Kelm, and M. Fussenegger. Advanced modular self-inactivating lentiviral expression vectors for multigene interventions in mammalian cells and in vivo transduction. *Nucleic Acids Res*, 30(21):e113, Nov 1 2002.
- B. Mitta, C. C. Weber, M. Rimann, and M. Fussenegger. Design and in vivo characterization of self-inactivating human and non-human lentiviral expression vectors engineered for streptogramin-adjustable transgene expression. *Nucleic Acids Res*, 32(12):e106, 2004.
- B. Mitta, C. C. Weber, and M. Fussenegger. In vivo transduction of hiv-1-derived lentiviral particles engineered for macrolide-adjustable transgene expression. *J Gene Med*, 7(11):1400–1408, Nov 2005b.
- U. Mitzdorf. Current source-density method and application in cat cerebral cortex: investigation of evoked potentials and EEG phenomena. *Physiol. Rev.*, 65(1):37–100, 1985.
- M. A. Moffitt and C. C. McIntyre. Model-based analysis of cortical recording with silicon microelectrodes. *Clinical Neurophysiology*, 116:2240–2250, September 2005.
- K. Monzen, R. Nagai, and I. Komuro. A role for bone morphogenetic protein signaling in cardiomyocyte differentiation. *Trends Cardiovasc Med*, 12(6):263–269, Aug 2002.
- K. Najafi and K.D. Wise. An implantable multielectrode array with on-chip signal processing. *IEEE Journal of Solid-State Circuits*, 21:1035–1044, 1986.
- C. Nicholson and J. A. Freeman. Theory of current source-density analysis and determination of conductivity tensor for anuran cerebellum. *J Neurophysiol*, 38(2):356–368, 1975.
- Y. C. Okada, J. C. Huang, M. E. Rice, D. Tranchina, and C. Nicholson. Origin of the apparent tissue conductivity in the molecular and granular layers of the in vitro turtle cerebellum and the interpretation of current source-density analysis. *J Neurophysiol*, 72(2):742–753, 1994.
- J. Pine. Recording action potentials from cultured neurons with extracellular microcircuit electrodes. *J Neurosci Methods*, 2(1):19–31, 1980.

- S. G. Priori and C. Napolitano. Role of genetic analyses in cardiology: part i: mendelian diseases: cardiac channelopathies. *Circulation*, 113(8):1130–1135, Feb 28 2006.
- M. C. Quirk, K. I. Blum, and M. A. Wilson. Experience-Dependent Changes in Extracellular Spike Amplitude May Reflect Regulation of Dendritic Action Potential Back-Propagation in Rat Hippocampal Pyramidal Cells. *J. Neurosci.*, 21(1):240–248, 2001.
- R.Q. Quiroga, Z. Nadasdy, and Y. Ben-Shaul. Unsupervised spike detection and sorting with wavelets and superparamagnetic clustering. *Neural Comput.*, 16(8):1661–87, 2004.
- E. Regulier, Y. Trottier, V. Perrin, P. Aebischer, and N. Deglon. Early and reversible neuropathology induced by tetracycline-regulated lentiviral overexpression of mutant huntingtin in rat striatum. *Hum Mol Genet*, 12(21):2827–2836, Nov 1 2003.
- R. F. Rice. Some practical universal noiseless coding techniques. *Jet Propulsion Laboratory, Pasadena, California, JPL Publication*, pages 79–22, Mar 1979.
- J. M. Ridley, J. T. Milnes, Y. H. Zhang, H. J. Witchel, and J. C. Hancox. Inhibition of hERG K⁺ current and prolongation of the guinea-pig ventricular action potential by 4-aminopyridine. *J Physiol*, 549(Pt 3):667–672, Jun 15 2003.
- R. B. Robinson, P. R. Brink, I. S. Cohen, and M. R. Rosen. I(f) and the biological pacemaker. *Pharmacol. Res.*, 53(5):407–415, May 2006.
- M. R. Rosen, P. R. Brink, I. S. Cohen, and R. B. Robinson. Genes, stem cells and biological pacemakers. *Cardiovasc Res*, 64(1):12–23, Oct 1 2004.
- A. Roth and M. Hausser. Compartmental models of rat cerebellar Purkinje cells based on simultaneous somatic and dendritic patch-clamp recordings. *J Physiol*, 535(2):445–472, 2001.
- M. Rubart and L. J. Field. Cardiac regeneration: repopulating the heart. *Annu Rev Physiol*, 68(8):29–49, 2006.
- M. Rubart, K. B. Pasumarthi, H. Nakajima, M. H. Soonpaa, H. O. Nakajima, and L. J. Field. Physiological coupling of donor and host cardiomyocytes after cellular transplantation. *Circ Res*, 92(11):1217–1224, Jun 13 2003.
- W.L.C. Rutten. Selective electrical interfaces with the nervous system. *Annual Review Of Biomedical Engineering*, 4:407–452, 2002.
- T. Sakoda, N. Kasahara, Y. Hamamori, and L. Kedes. A high-titer lentiviral production system mediates efficient transduction of differentiated cells including beating cardiac myocytes. *J Mol Cell Cardiol*, 31(11):2037–2047, Nov 1999.
- C. D. Sanchez-Bustamante, J. M. Kelm, B. Mitta, and M. Fussenegger. Heterologous protein production capacity of mammalian cells cultivated as monolayers and microtissues. *Biotechnol. Bioeng.*, 93(1):169–180, Jan 5 2006.
- C. Diaz Sanchez-Bustamante, U. Frey, J. Kelm, A. Hierlemann, and M. Fussenegger. Modulation of Electrical Properties of Cardiomyocytes by Regulated BMP-2 Expression. *Tissue Engineering*, in publication, 2008.
- R. SoRelle. Myoblast transplant to heart attempted. *Circulation*, 102(15):E9030–1, Oct 10 2000.

- M. S. Spach, W. T. Miller, rd, E. Miller-Jones, R. B. Warren, and R. C. Barr. Extracellular potentials related to intracellular action potentials during impulse conduction in anisotropic canine cardiac muscle. *Circ Res*, 45(2):188–204, Aug 1979.
- D.A. Stenger, G.W. Gross, E.W. Keefer, K.M.Shaffer, J.D. Andreadis, W. Ma, and J.J. Pancrazio. Detection of physiologically active compounds using cell-based biosensors. *TRENDS in Biotechnology*, 19(8):304–309, 2001.
- A. Stett, U. Egert, E. Guenther, F. Hofmann, T. Meyer, W. Nisch, and H. Haemmerle. Biological application of microelectrode arrays in drug discovery and basic research. *Analytical and Bioanalytical Chemistry*, 377:486–495, October 2003b.
- B. E. Strauer, M. Brehm, T. Zeus, M. Kosterling, A. Hernandez, R. V. Sorg, G. Kogler, and P. Wernet. Repair of infarcted myocardium by autologous intracoronary mononuclear bone marrow cell transplantation in humans. *Circulation*, 106(15):1913–1918, Oct 8 2002.
- G. Stuart and M. Hausser. Initiation and spread of sodium action potentials in cerebellar Purkinje cells. *Neuron*, 13(3):703–712, 1994.
- G. Stuart, N. Spruston, B. Sakmann, and M. Hausser. Action potential initiation and back-propagation in neurons of the mammalian cns. *Trends in Neurosciences*, 20:125–131, February 1997.
- S. Takahashi, Y. Anzai, and Y. Sakurai. A new approach to spike sorting for multi-neuronal activities recorded with a tetrode how ICA can be practical. *Neurosci Res*, 46(3):265–272, 2003a.
- C.A. Thomas, P.A. Springer, G.E. Loeb, Y. Berwald-Netter, and L.M. Okum. A miniature microelectrode array to monitor the bioelectric activity of cultured cells. *Experimental Cell Research*, 74:61–66, 1972.
- James S. Trimmer and Kenneth J. Rhodes. Localization of voltage-gated ion channels in mammalian brain. *Annual Review of Physiology*, 66(1):477–519, 2004.
- G. Vandecasteele, T. Eschenhagen, H. Scholz, B. Stein, I. Verde, and R. Fischmeister. Muscarinic and beta-adrenergic regulation of heart rate, force of contraction and calcium current is preserved in mice lacking endothelial nitric oxide synthase. *Nat Med*, 5(3):331–334, Mar 1999.
- P. Vetter, A. Roth, and M. Hausser. Propagation of Action Potentials in Dendrites Depends on Dendritic Morphology. *J Neurophysiol*, 85(2):926–937, 2001.
- E. Vigna, S. Cavalieri, L. Ailles, M. Geuna, R. Loew, H. Bujard, and L. Naldini. Robust and efficient regulation of transgene expression in vivo by improved tetracycline-dependent lentiviral vectors. *Mol Ther*, 5(3):252–261, Mar 2002.
- R. Vogel, L. Amar, A. D. Thi, P. Saillour, and J. Mallet. A single lentivirus vector mediates doxycycline-regulated expression of transgenes in the brain. *Hum Gene Ther*, 15(2):157–165, Feb 2004.
- D. Wagenaar, J. Pine, and S. Potter. An extremely rich repertoire of bursting patterns during the development of cortical cultures. *BMC Neuroscience*, 7(1):11, 2006a.
- D. R. Van Wagoner, M. Kirian, and M. Lamorgese. Phenylephrine suppresses outward k+ currents in rat atrial myocytes. *Am J Physiol*, 271(3 Pt 2):H937–46, Sep 1996.

- L. Wang and H. J. Duff. Developmental changes in transient outward current in mouse ventricle. *Circ Res*, 81(1):120–127, Jul 1997.
- Y. X. Wang, L. X. Qian, D. Liu, L. L. Yao, Q. Jiang, Z. Yu, Y. H. Gui, T. P. Zhong, and H. Y. Song. Bone morphogenetic protein-2 acts upstream of myocyte-specific enhancer factor 2a to control embryonic cardiac contractility. *Cardiovasc Res*, 74(2):290–303, May 1 2007.
- W. Weber and M. Fussenegger. Novel gene switches. *Handb. Exp. Pharmacol.*, (178):73–105, 2007.
- J. M. Wozney, V. Rosen, A. J. Celeste, L. M. Mitsock, M. J. Whitters, R. W. Kriz, R. M. Hewick, and E. A. Wang. Novel regulators of bone formation: molecular clones and activities. *Science*, 242(4885):1528–1534, Dec 16 1988.
- R. P. Xiao, W. Zhu, M. Zheng, K. Chakir, R. Bond, E. G. Lakatta, and H. Cheng. Subtype-specific beta-adrenoceptor signaling pathways in the heart and their potential clinical implications. *Trends Pharmacol Sci*, 25(7):358–365, Jul 2004a.
- Y. F. Xiao, Q. Ke, S. Y. Wang, Y. Yang, Y. Chen, G. K. Wang, J. P. Morgan, B. Cox, and A. Leaf. Electrophysiologic properties of lidocaine, cocaine, and n-3 fatty-acids block of cardiac Na^+ channels. *Eur. J. Pharmacol.*, 485(1-3):31–41, Feb 6 2004b.
- T. Xue, H.C. Cho, F.G. Akar, S.Y. Tsang, S.P. Jones, E. Marban, G.F. Tomaselli, and R.A. Li. Functional integration of electrically active cardiac derivatives from genetically engineered human embryonic stem cells with quiescent recipient ventricular cardiomyocytes: insights into the development of cell-based pacemakers. *Circulation*, 111(1):11–20, 2005.
- M. Yedlin, H. Kwan, J. T. Murphy, H. Nguyen-Huu, and Y. C. Wong. Electrical conductivity in cat cerebellar cortex. *Experimental Neurology*, 43:555–569, June 1974.
- Gunther Zeck and Peter Fromherz. Noninvasive neuroelectronic interfacing with synaptically connected snail neurons immobilized on a semiconductor chip. *PNAS*, 98(18):10457–10462, 2001.
- H. Zhang and A. Bradley. Mice deficient for *bmp2* are nonviable and have defects in amnion/chorion and cardiac development. *Development*, 122(10):2977–2986, Oct 1996.
- S. Zhang. Beyond the petri dish. *Nat. Biotechnol.*, 22(2):151–152, Feb 2004.
- J. Zhao, G. J. Pettigrew, J. Thomas, J. I. Vandenberg, L. Delriviere, E. M. Bolton, A. Carmichael, J. L. Martin, M. S. Marber, and A. M. Lever. Lentiviral vectors for delivery of genes into neonatal and adult ventricular cardiac myocytes in vitro and in vivo. *Basic Res Cardiol*, 97(5):348–358, Sep 2002.

Part II

Microhotplate Gas Sensor

Chapter 8

Introduction

This part of the thesis reports on work in the context of the European project ADA¹. The core team of three people in this project included:

- Markus Graf: transistor-heater based microhotplate, design, fabrication, characterization and measurements.
- Urs Frey: Data acquisition system, characterization and testing of the device, redesign of the device and gas measurement tests.
- Stefano Taschini: Initial circuit design of the device.

This part contains a single paper:

- *A Digital CMOS Architecture for a Micro-Hotplate Array*
U. Frey, M. Graf, S. Taschini, K.-U. Kirstein, and A. Hierlemann
Journal of Solid-State Circuits 2007, 42(2), pp. 441-450.

Additional measurements can be found in Graf et al. [Graf et al., 2006].

¹ADA: Advanced distributed architecture for telemonitoring services. BBW Nr. 00.0591, EU Nr. IST-2000-28452, duration: 08.2001-08.2004.

Chapter 9

A Digital CMOS Architecture for a Microhotplate Array

Urs Frey, Markus Graf, Stefano Taschini,
Kay-Uwe Kirstein, and Andreas Hierlemann

Journal of Solid-State Circuits 2007, 42(2), pp. 441-450¹

Physical Electronics Laboratory, ETH Zurich, Switzerland

Abstract A monolithic gas sensor array fabricated in industrial CMOS technology combined with post-CMOS micromachining is presented. The device comprises an array of three metal-oxide-coated microhotplates with integrated MOS transistor heaters and the needed driving and signal-conditioning circuitry. Three digital PID controllers enable individual temperature regulation for each hotplate. The operating temperature of the SnO₂ metal-oxide sensors may amount up to 350°C. A serial interface and the temperature control units have been digitally implemented. Emphasis was put on designing a modular system with the required analog circuitry reduced to a minimum. With its small overall size of 5.5 x 4.5 mm², its digital interface and its good hotplate thermal efficiency of 6°C/mW, the system represents a significant development on the way to low-cost mobile gas sensor systems. The limit of detection at constant temperature has been assessed to be below 1 ppm for CO and approximately 100 ppm for CH₄. The mainly digital implementation with a maximum sampling rate of 9.3 kHz for all three sensors offers the advantage to apply a power-saving mode and temperature modulation techniques to enhance the analyte discrimination capability.

¹Manuscript received February 15, 2006; revised October 18, 2006. Digital Object Identifier 10.1109/JSSC.2006.889367.

9.1 Introduction

Chemical sensors based on CMOS technology can be categorized in four groups with regard to the respective transduction principle: chemomechanical sensors, thermal sensors, optical sensors and electrochemical sensors [Janata, 1989, Hierlemann and Baltes, 2003]. The sensor presented here is a high-temperature chemoresistor belonging to the last category. High-temperature chemoresistors usually operate between 200°C and 600°C and rely on wide-bandgap semiconducting materials as sensitive layers contacted by two metal electrodes. The resistance and the gas-induced resistance changes of the semiconducting material, such as tin oxide, gallium oxide, indium oxide, or zinc oxide, are then measured. In general, gaseous species, which act as electron donors (hydrogen) or electron acceptors (nitrogen oxide), adsorb at the metal-oxide surface and form surface states, which, can exchange electrons with the semiconductor at high temperature. An acceptor molecule will extract electrons from the semiconductor metal-oxide and thus decrease its conductivity. The opposite holds true for an electron-donating gas molecule. The reaction between the gases and the oxide surface depends on the sensor temperature, the nature of the gases involved, and sensor materials.

There are two main technological challenges in developing a fully integrated, high-temperature chemoresistor-based sensor. The chemoresistors need operation temperatures of up to 350°C, so that the circuitry needs to be protected against such elevated temperatures and associated large temperature fluctuations. Therefore, the heated stage has to be thermally decoupled from the circuitry. To this end, thermally well-insulated and well controlled stages such as membranes, which allow for keeping the sensing materials at a known and adjustable high temperature without heating the bulk chip (protection of electronic components), are used. The second challenge concerns the large range of initial material resistances and the large dynamic sensor response or resistance change range, which can amount up to six orders of magnitude. Resistance changes can be positive or negative depending on the detected gas (oxidizing/reducing gas). The required measurement range in each direction is three orders of magnitude, which leads to a total of six orders of magnitude.

Moreover, there is a strong interest in developing so-called microhotplate -based gas sensors due to miniaturization advantages, such as low power consumption, the use in portable devices and the possibility of applying new dynamic sensor operation modes owing to the low thermal mass of such hotplates [Semancik et al., 2001, Simon et al., 2001]. Commercial CMOS technology offers reliable batch-fabrication and enables low-cost mass production. Moreover, the use of micromachining technologies allows for the integration of the sensor structures with the electronics on the same CMOS chip [Hierlemann and Baltes, 2003]. First versions of monolithic microhotplate-based gas sensor systems in CMOS technology have been demonstrated in the past [Afridi et al., 2002, Graf et al., 2004b,a, Suehle et al., 1993].

Metal oxides are known to exhibit high sensitivities to environmentally relevant gases such as carbon monoxide or methane. However, these materials are also well known for their lack of selectivity and their inherent drift. An array of sensors and the use of multi-component analysis algorithms, such as principal component regression (PCR), multi-way analysis (MCR, PARAFAC), partial least squares (PLS) or artificial neural networks (ANN) can help to partially overcome these problems [Gutierrez-Osuna, 2002, Hines et al., 2003, Heilig et al., 1997, Wollenstein et al., 2003].

Most existing devices are based on resistive heating elements for the hotplates. An alternative approach is the integration of a transistor heater [Graf et al., 2005b]. A key advantage of transistor-based heaters is a significant reduction of the overall power consumption, since no additional power amplifier is needed on chip for driving the heating current. Moreover, new temperature control modes are feasible, since the microhotplate temperature is directly adjustable via the gate voltage of the transistor heater, the correlation between temperature and gate voltage being almost linear [Graf et al., 2005b].

The device presented here features three microhotplates monolithically integrated with digital proportional-integral-derivative (PID) temperature controllers, digital readout, and a serial interface. The hotplates were covered with different tin dioxide (SnO_2)-based sensitive materials. The pure SnO_2 , which is predominantly sensitive to nitrogen dioxide (NO_2), was doped with different concentrations of palladium (Pd) and thus rendered more sensitive to carbon monoxide (CO) or methane (CH_4). All sensor functions can be accessed via the digital interface, which drastically reduces the number of connections and, hence, the packaging efforts.

The device presented here features a very high degree of integration in comparison to other CMOS-based systems [Afridi et al., 2002, Wollenstein et al., 2003], and it provides a standard digital bus interface. All logic units needed for the relatively fast operation of the closed-loop temperature controllers are integrated on the device. In comparing the device with other systems that feature a similar level of integration [Barrettino et al., 2004a] the following aspects are important: 1) the power efficiency has been improved due to the use of a transistor heater, that is driven by a pulse-density modulated bitstream; 2) the system complexity has been decreased as a consequence of sharing several important circuitry units and due to the mostly digital realization; 3) the system consumes much less area than that reported on in [Barrettino et al., 2004a]; porting the device to a CMOS technology with a smaller feature size would decrease the required CMOS real estate even further; 4) a practical solution (adjustable bias, see later in the text) to cope with the huge range of sensor resistances has been implemented; and 5) all reference voltages and currents are generated on chip.

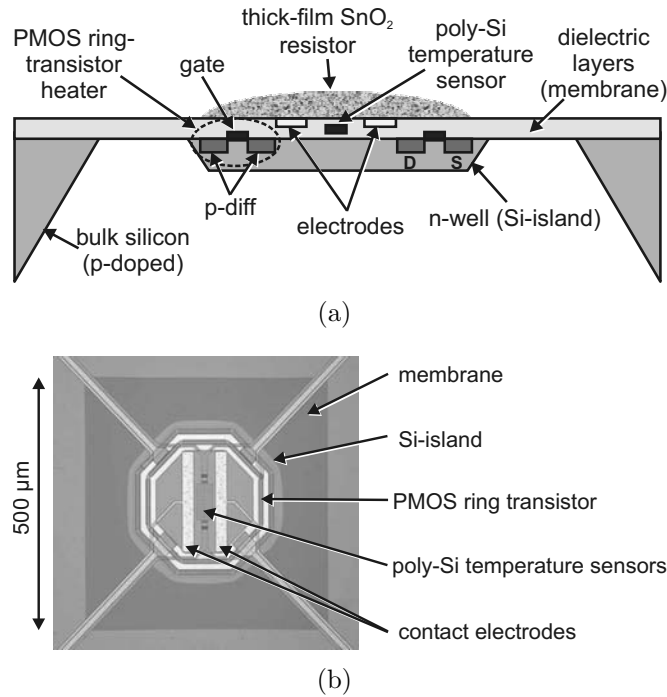


Figure 9.1: Microhotplate with integrated MOS-transistor heater. (a) Cross section of a microhotplate. (b) Micrograph of a hotplate without the SnO₂ sensitive metal-oxide layer.

9.2 Microhotplate Design

Figure 9.1 shows the cross-section and a micrograph of a single microhotplate. In order to ensure a good thermal decoupling of the hotplate from the rest of the chip, only the dielectric layers of the industrial CMOS process form the membrane. The inner section of the membrane additionally includes an n-well silicon island underneath the dielectric layers. The n-well is thermally and electrically insulated and serves as a heat spreader. It also hosts the pMOS transistor, which constitutes the heating element. The resistance change of the nanocrystalline thick-film SnO₂-layer upon gas exposure is measured by means of two metal electrodes. In order to establish a good contact to the sensitive layer, the CMOS aluminum electrodes are first covered with titanium/tungsten (Ti/W, diffusion barrier and adhesion layer, 50 nm) followed by a platinum layer (Pt, 200 nm). The total size of the quadratic membrane is 500 μm by 500 μm. The octagonal shape of the n-well silicon island provides a relatively long distance between the heated membrane area and the cold bulk of the chip. Thus, the heat dissipation via metal connections is considerably reduced. The overall membrane layout is symmetric to ensure a homogeneous temperature and stress distribution.

The pMOS transistor of 5 μm gate-length and 720 μm overall gate width is integrated on the island, it is an improved version of the transistor heater described in [Graf et al., 2005b]. A special ring-shape transistor arrangement was chosen.

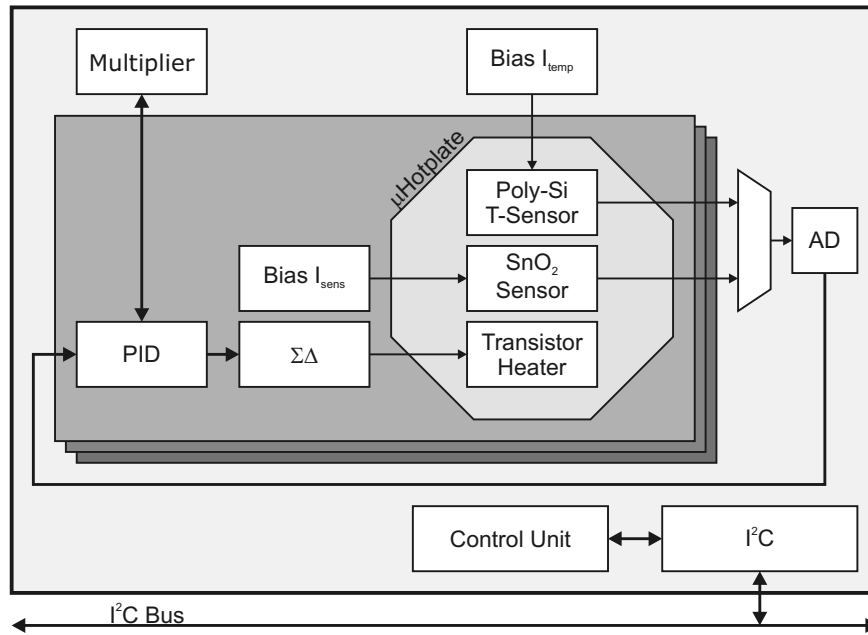


Figure 9.2: Block diagram of the monolithic system.

This shape leaves enough space to implement resistive polysilicon temperature sensors in the center. The thermistor in the lower part of Figure 9.1b is used to control the membrane temperature. The other temperature sensor is not connected to the control circuitry and can be used for an accurate calibration of the membrane temperature and for the verification of the controller performance.

9.3 Integrated Gas Sensor System

9.3.1 Architecture

Figure 9.2 shows a block diagram of the system architecture. The system is designed in a modular fashion to enable future designs with larger arrays of sensors.

Three digital PID controllers provide independent temperature regulation for each hotplate. The MOS heating transistors are operated in pulse-density modulation by a first-order $\Sigma\Delta$ -modulator. Analog circuitry is required only for the readout of the metal-oxide resistors, the temperature sensors, and for the necessary bias currents. A single analog-to-digital converter and a single multiplier for the PID controllers are accessed in time-multiplexed fashion. The control unit takes care of scheduling the different operations, the access to the shared multiplier and to the shared analog-to-digital converter (ADC) for all three hotplates. An inter-IC (I²C) bus interface is used to connect to off-chip units.

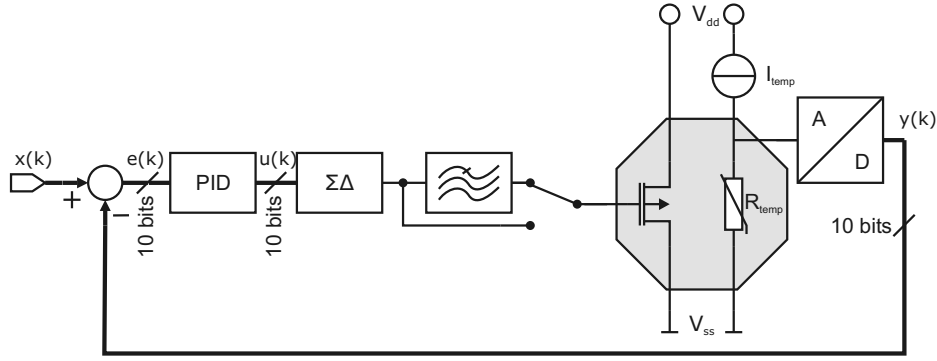


Figure 9.3: Temperature control loop.

9.3.2 Analog-to-Digital Conversion

The analog-to-digital converter is realized as a 10-bit successive-approximation (SAR) ADC. An internal bandgap with a nominal voltage of 1.26 V, or an external voltage can be used as reference voltage for the ADC. The ADC features a maximum sampling rate of 50 kSamples/s. The digital-to-analog converter (DAC) and the comparator are located in the analog chip section, however, the SAR registers and the logic controlling the DAC and the comparator are included in the digital part.

9.3.3 Temperature Control

The schematic of the temperature control loop is shown in Figure 9.3. The temperature on the microhotplate is measured using a polysilicon resistor, R_{temp} , as a temperature sensor with a nominal resistance of approximately 10 k Ω . The resistor is biased with an adjustable, temperature-independent current, I_{temp} , to cope with process variations. The voltage drop across the resistor is converted to a 10-bit digital value, labeled $y(k)$ in Figure 9.3. This value is fed back to the digital PID temperature controller, which is implemented as a recursive filter. The PID implementation is based on the following continuous-time equation:

$$u(t) = K \left(e(t) + \frac{1}{\tau_i} \int_0^t e(t) dt + \tau_d \frac{de(t)}{dt} \right),$$

where K is the gain, τ_i is the integral time, τ_d the derivative time, $e(t)$ the error value and $u(t)$ the actuation value, as shown in Figure 9.3. The discrete time form in the z -plane is given by

$$D(z) = \frac{u(z)}{e(z)} = K \left(1 + \frac{1}{\tau_i} \frac{T_s}{2} \frac{z+1}{z-1} + \frac{\tau_d}{T_s} \frac{z-1}{z} \right),$$

with T_s being the sampling period. It is implemented in the following form:

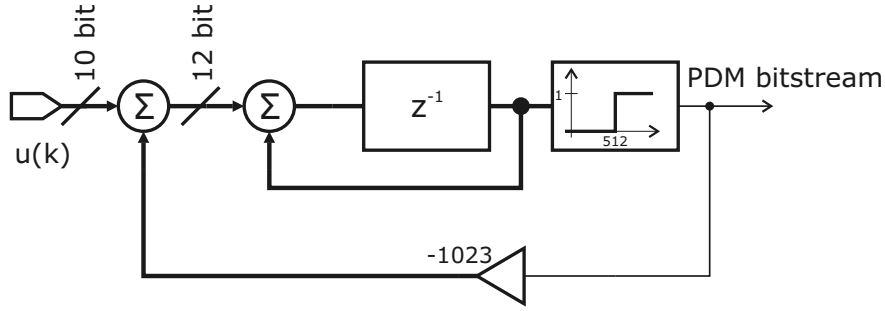


Figure 9.4: Sigma-Delta Modulator.

$$u(k) = u(k-1) + c_0 e(k) + c_1 e(k-1) + c_2 e(k-2),$$

where k are the time-discrete indices and

$$\begin{aligned} c_0 &= K \left(1 + \frac{T_s}{2\tau_i} + \frac{\tau_d}{T_s} \right) \\ c_1 &= K \left(-1 + \frac{T_s}{2\tau_i} - 2\frac{\tau_d}{T_s} \right) \\ c_2 &= K \frac{\tau_d}{T_s}. \end{aligned}$$

The sampling period, T_s , is adjustable using the digital interface with a minimum value of $108 \mu\text{s}$, resulting in a sampling rate of 9.3 kHz for all three sensors. The value corresponding to the target temperature, $x(k)$, is given as a 10-bit value, and the three PID coefficients, c_0 , c_1 , and c_2 , are 11-bit signed values that can be set individually for each hotplate. The actuation value, $u(k)$, calculated by the PID is then converted to a pulse-density modulated (PDM) digital bitstream using a digital first-order modulator with a sampling rate of 500 kHz, as shown in Figure 9.4.

The heating transistor is directly driven with this bitstream or, optionally, the bitstream can be filtered using a low pass. Early experiments revealed that driving the heating transistor with the unfiltered bitstream might cause some electromigration as a consequence of the high peak currents. A low-pass filter option was therefore included to enhance the hotplate lifetime and reliability. It is implemented as a second-order Sallen-Key filter with a cut-off frequency of 17 kHz, far above the actual thermal time constant of the hotplate, which is below 10 ms for uncoated hotplates and around 20 ms for coated hotplates, depending on the overall volume of the deposited material.

As the thermal capacitance and resistance of the hotplate provide a thermal low-pass transfer function with the dominant pole corresponding to a measured characteristic time of 10 to 20 ms, the modulator driving the hotplate constitutes a linear noise-shaping DAC with output in the thermal domain and a low pass cut-off frequency of around 100 Hz.

The main advantage of using a transistor heater, as opposed to a resistor, is a significant reduction in power consumption and an improvement of the life time. If a resistor is driven with an off-membrane power transistor that is controlled by an analog voltage, this power transistor will consume a considerable fraction of the overall power. An off-membrane power-transistor can also be controlled by means of a digital bitstream from, e.g., a sigma-delta modulator, which offers the potential of drastically reducing the amount of needed power. However, as mentioned above, electromigration may still reduce the life time of a sensor operated this way. By integrating the transistor on the hotplate, large current peaks can be avoided through driving the transistor with an analog voltage without dissipating any power off membrane.

9.3.4 SnO₂ Resistance Readout and Current Biasing

There are several ways to cope with the large range of resistances, from a few k Ω s to several tens of M Ω s, that can occur in metal oxide layers, such as SnO₂. A logarithmic compression of the resistance value can be employed [Barrettino et al., 2004d]. Another way is to make use of an oscillator, the time constant of which is proportional to the sensor impedance [Flammini et al., 2004, Bota et al., 2004, Grassi et al., 2005]. All these compression methods primarily aim at being able to cope with the huge range of initial material resistances. Another issue is to linearize the gas response of the sensors, which is approximately exponential. The latter, however, can be done in a better way on a PC, in particular, since there are numerous data analysis methods that can cope with non-linear data. Tin oxide materials exhibit quite large baseline drifts during measurements and also show baseline resistance variations from batch to batch, so that the baseline value is usually subtracted from the measured data, and only relative resistance changes are used for the data analysis. For the analysis of relative changes, a logarithmic compression is very appropriate, as it provides a defined and constant resolution for relative changes over the whole measurement range.

The approach selected for the system here is to measure the voltage drop across the SnO₂ sensitive layer upon biasing with a constant current, as shown in Figure 9.5. To cope with the large resistance range a 10-bit adjustable bias current source has been implemented. A reference current of around 15 μ A, generated by a temperature-compensated constant-current source, is copied by means of a binary-scale current mirror with cascoded stages. The digital current bias registers are used to switch on and off the individual currents. The resulting current has a maximum value of 109 μ A, yielding a least-significant bit (LSB) of around 0.1 μ A. This results in a measurable resistance of up to 12 M Ω using the on-chip band gap reference for the ADC.

The current flowing through the sensor electrodes can be separately adjusted for each hotplate. The voltage drop across the resistive material is then converted

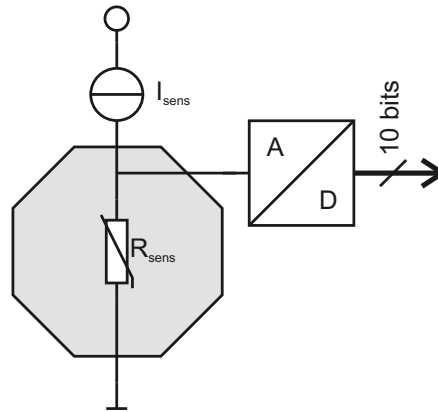


Figure 9.5: Sensor resistance readout.

to a digital value with the same successive-approximation ADC that is also used for the temperature control loop.

Figure 9.6 sketches the dynamic range and the theoretically resolvable resistance value as obtained by using this approach. For very high resistances, the minimum bias current needs to be applied to obtain a measurable voltage drop across the sensor. When the resistance drops, the voltage drops as well. Once a certain, relatively low voltage is reached, the bias can be increased to achieve a better resolution. In this region, the bias current is continuously updated by the software to keep the output voltage at a fixed level. Once the resistance goes to very low values, the maximum bias current is reached, and a further increase in resolution is not possible anymore. The theoretical resolution of 20 bits is only reached for low resistances when the largest possible bias current is applied (ideal current-source and ADC). For larger resistances, the resolution drops and reaches 10 bits when the smallest possible bias current is applied. The approach chosen here, therefore, corresponds to a logarithmic compression, which would be represented by a straight line in Figure 9.6. However, it does not rely on the logarithmic properties of analog units in contrast to the method presented in ref. [Barrettino et al. \[2004d\]](#).

9.3.5 Control Unit and Serial Interface

Apart from the digital units described above, the digital core, which occupies nearly half of the device area, also includes an interface to the outside world and a control unit. The control unit mainly controls the timing of the ADC and the PIDs and the access to the shared multiplier. The minimum cycle time is 108 clock cycles, which, however, can be prolonged by setting the T_s register. The operations are performed sequentially for each hotplate, resulting in a minimum of 36 clock cycles per hotplate. The operations that have to be executed include two ADC conversions and one PID operation executed in parallel. As three multiplications are needed for one PID operation, and as these are performed by

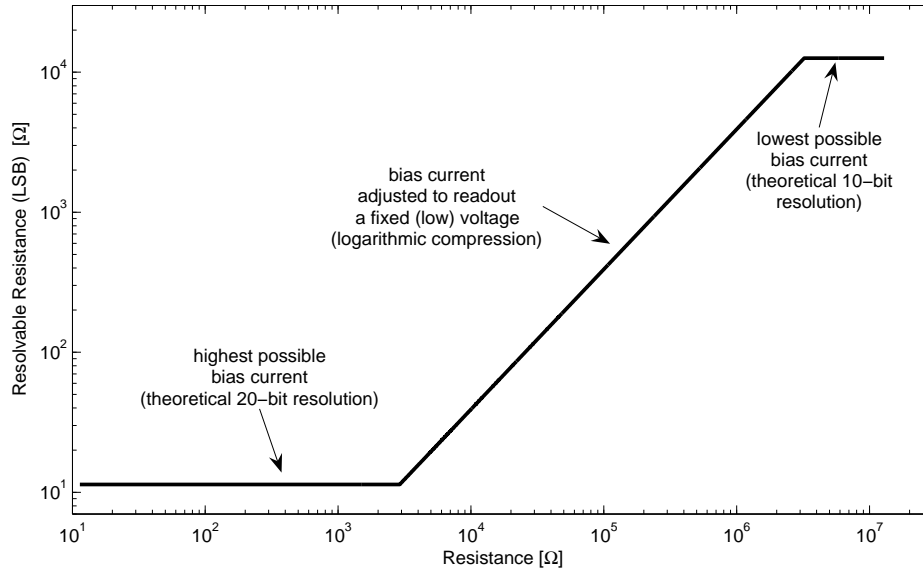


Figure 9.6: Resolvable resistance versus sensor resistance. The resistance in Ohms corresponding to the least significant bit of the ADC is plotted versus the absolute sensor resistance. For the slope in the center of the graph, the bias current is continuously updated to keep the voltage at a fixed level, here $1/3$ of the ADC range, which corresponds to a logarithmic compression.

means of a single sequential fixed-point multiplier, the speed is limited by these multiplications. The control unit also takes care of the settings of the analog multiplexer in front of the ADC.

To reduce the number of needed bond pads and to reduce external circuitry to a minimum, an I²C serial bus, which is available on most micro controllers, was used to interface to the chip. The communication protocol is kept very simple. The I²C address is split into two parts, the lower two bits are used to address the individual sensors on a single sensor chip, whereas the upper 5 bits can be used to address other devices, such as other sensor systems on the same I²C bus. The first data byte contains the register address. The following optional byte contains the actual data that is to be written to the specified register. Registers that can be written and read include the PID coefficients, the PID sampling period, the target temperature, the different bias currents and some flags used for power-down mode and calibration settings. Registers that are only readable include the voltage values originating from the sensor material and the temperature sensor signals as converted by the ADC.

The I²C core on the chip uses the serial clock (SCL) line to clock in the data and, therefore, works at high speed. The current setup provides bit rates of 330 kHz and more. For a single register, this results in a rate of more than 3000 readings per second, so that reading of the three sensor values can be done faster than 1 kSample/s. If new target temperatures and new bias currents have to be set at every sampling of the resistance readout, and if the measured temperature of

all hotplates needs to be read out as well, the read-out rate is reduced to 250 Hz, which is still fast in comparison to the thermal time constant of the hotplates or the electrochemical processes in the sensitive material.

9.3.6 Fabrication

The chip is fabricated in industrial 5-Volt, 0.8- μm , double-poly, double-metal CMOS technology as provided by austriamicrosystems. The total chip dimensions are 5.5 x 4.5 mm². The electrodes are first covered with Ti/W followed by a Pt-layer, which are both patterned by lift-off. The membranes are released by etching the wafer from the backside with potassium hydroxide (KOH). An electrochemical etch-stop technique is used to preserve the central n-well islands of the hotplates. The deposition and annealing of the nanocrystalline tin dioxide containing various dopings at 400°C concludes the post-processing sequence, which is fully CMOS-compatible [Graf et al., 2004a].

The die is then affixed to a gold-coated TO8-16 package and wire-bonded. To protect the bond wires and the circuitry, the chip is partially covered with a glob top epoxy, which leaves only the three membranes uncovered.

Figure 9.7 shows the fabricated chip with the digital circuitry on the left side including the three temperature controllers and the $\Sigma\Delta$ converters, the control unit and the serial interface. The analog circuitry for biasing and A/D conversion is placed in the center, and the three microhotplates are located on the right side.

The analog circuitry is comparably small, because of the time-multiplexed access to the ADC and the employment of a transistor-based heater without the need for additional analog driving circuitry. The number of bond pads (left side of Figure 9.7) is reduced to only 11, which drastically decreases the packaging efforts. Five of those pads are used for the I²C address, they are equipped with pull-down transistors and only need to be bonded if more than one device will be attached to the same I²C bus.

9.4 Measurement Results

To perform chemical measurements, an USB-to-I²C adapter was used, as shown in Figure 9.8. Optionally, a printed-circuit-board (PCB) adapter on a ribbon cable can be connected for easier insertion into a gas measurement setup. On the PC side, LabView was used to control the sensor and acquire the data. The software allows to apply arbitrary functions to modulate the temperature on the hotplates, provides a control loop for automatic bias current adjustments, and includes routines to convert the register values of the applied bias currents and read-out voltages to temperatures in degrees Celsius and sensor resistances in Ohms. The conversion of register values to Ohms is done by taking into account

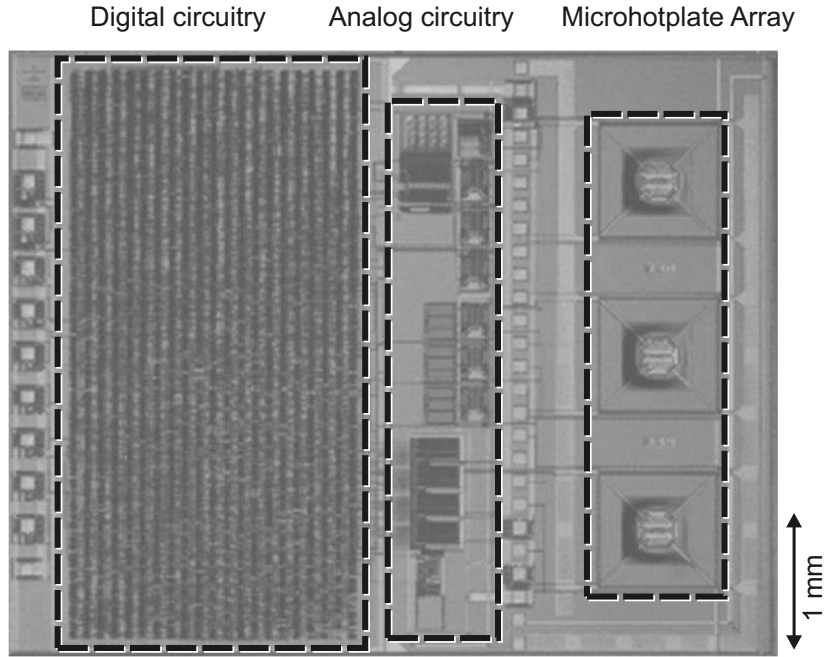


Figure 9.7: Micrograph of the fabricated monolithic hotplate sensor system.

the non-linearity of the current source as described later (Section 9.4.1.1). The conversion of the temperature-sensor resistances to degrees Celsius is done as described in ref. Graf et al. [2004b] by using the following equation:

$$\Delta T = T - T_0 = \alpha_1 \left(\frac{\Delta R}{R_0} \right) + \alpha_2 \left(\frac{\Delta R}{R_0} \right)^2.$$

The polysilicon temperature coefficients α_1 and α_2 of this second-order polynomial have been measured beforehand. To account for process variations, R_0 is measured for each single hotplate. During short measurement intervals of typically a few hours, no significant drift in R_0 occurred. However, in long-term measurements over several months, which have been performed with this system, a first-order recalibration by measuring R_0 was done every few days.

The tasks performed in LabView are roughly sketched in Algorithm 1. After a chip reset the device is initialized using appropriate default values, which include: PID settings, $c_{0,i}$, $c_{1,i}$, $c_{2,i}$, PID sampling period for each hotplate, i , the bias current, I_{temp} , for the temperature sensors, bias currents, $I_{sens,i}$, for the SnO₂ sensors, some flags specifying calibration modes, power modes and optional low-pass settings. Initially, the target temperature, x_i , is set to 0. Then an optional first-order calibration of the poly-Si temperature is performed, which is required only every few days. During the measurement cycle, the temperature value, y_i , and the sensor value, $sens_i$, are read from the sensor and converted to degrees Celsius and Ohms respectively. The raw register values are stored to the hard disk for later analysis. The obtained sensor value is then compared to a specified

Algorithm 1 LabView Program

1. open device
 2. reset chip
 3. send initial settings
 4. IF needed THEN perform first-order recalibration of poly-Si temperature sensor
 5. read temperature sensor, y_i , and SnO₂ sensor, $sens_i$, of all hotplates
 6. calculate new SnO₂ bias currents, $I_{sens,i}$, for all hotplates
 - (a) IF $sens_i < min$ THEN $I(k+1)_{sens,i} = I(k)_{sens,i} * (1 + adjRatio)$
 - (b) IF $sens_i > max$ THEN $I(k+1)_{sens,i} = I(k)_{sens,i} * (1 - adjRatio)$
 7. IF needed THEN update target temperatures, x_i , and $I_{sens,i}$
 8. wait
 9. IF continue THEN GOTO step 4
 10. close device
-

minimum register value (approx. 1/4 of the total range) and a maximum register value (approx. 5/6) and, if needed, the bias current is adjusted by the factor *adjRatio*, which is usually approximately 8%. If one or more temperature profiles of the individual hotplates require a new target temperature, x_i , the respective registers are written. An optional delay is inserted before the program loops back to step 4. As all these operations have to be executed at a rather low frequency (in contrast to the on-chip PID controller), they can easily be performed on an external device. In the current measurement setup, the USB-to-I²C adapter is the speed-limiting factor. For very fast temperature profiles, this adapter would have to be optimized for speed, or the control loop would have to be executed on a microcontroller connected to the I²C bus.

9.4.1 Electrical Measurements

9.4.1.1 Current Biasing

The 10-bit current source has a measured integral nonlinearity (INL) of ± 2.5 LSB. For the temperature sensor, the source current is set once and is then not changed anymore. The first-order recalibration of the sensor as explained above also accounts for nonidealities of the current source. For the readout of the chemore-

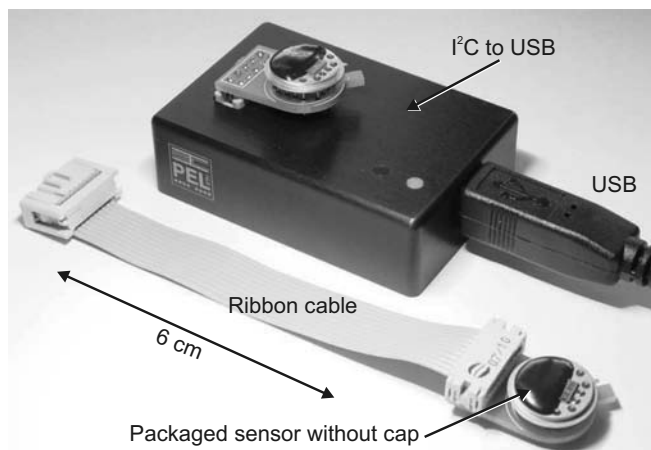


Figure 9.8: Micrograph of a packaged sensor system connected to an I²C-to-USB adapter.

sistors, the nonidealities of the current source have to be taken into account. As the sensor values are sent to a PC for analysis and not further processed on the chip, this can be achieved by calibrating the current source with an external resistor with a defined value. The obtained current values are then stored and taken into account for the calculation of the resistances from the respective current source settings and measured voltages. If the calibration needs to be done without the use of an external resistor it could be done by relying on the fact that the temperature resistor on an unheated hotplate only carries low-frequency AC signals. The hotplate temperature resistor can, therefore, be used for a relative calibration of the current source without the need for an external resistor.

9.4.1.2 Analog to Digital Converter

The 10-bit successive-approximation ADC has a measured INL of ± 2.5 LSB from 0 V to 1.26 V, which is mainly caused by nonlinearities of the driving buffer at low voltages. Due to the flexible biasing scheme as detailed in 9.3.4, the ADC can be operated, except for very small resistances below 3 k Ω , in the upper three quarters of the full range, where it has a measured INL of ± 1.5 LSB. The measured differential nonlinearity (DNL) is ± 0.5 LSB, which entails a good overall accuracy. For the readout of the sensor material resistance, an accuracy of better than 99.8 % has been achieved. In the case of the temperature sensor, the deviation resulting from the ADC INL is $\pm 1.8^\circ\text{C}$ at 300°C.

9.4.1.3 Temperature Control

The performance of the temperature controller was measured in stabilization mode and in tracking mode. Figure 9.9 shows a graph, in which the temperature

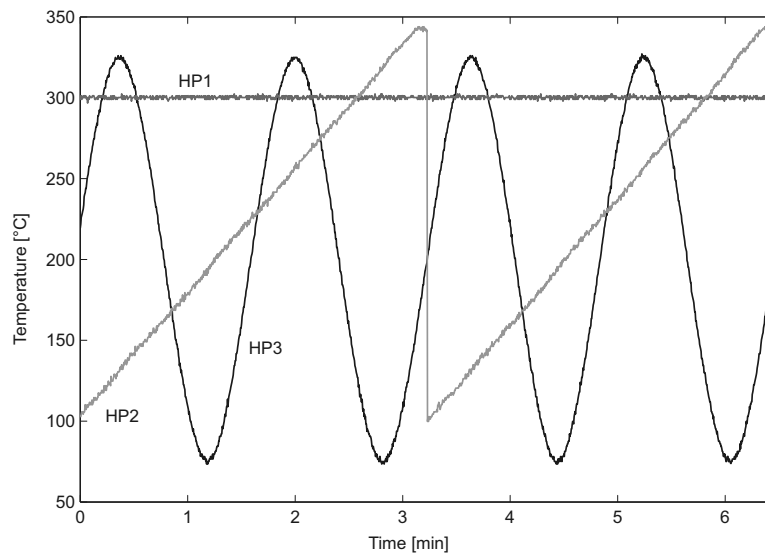


Figure 9.9: Temperature tracking in PID control mode: one hotplate (HP1) is kept at constant temperature (300°C), while the temperature of the other two is modulated sinusoidally (HP3) or in a saw-tooth form (HP2).

of one microhotplate (HP1) is kept at a constant temperature of 300°C, the temperature of HP2 is ramped from 100°C up to 350°C and the temperature of HP3 is modulated using a sine wave of 10 mHz. Operating one hotplate in constant temperature stabilization mode, the measurements showed a variance below 1°C, while modulating the temperature of the neighboring hotplates. Without individual temperature control, thermal crosstalk between the hotplates would be clearly visible.

Figure 9.10 shows the response of the polysilicon temperature sensor that is not connected to the circuitry and has been measured with an oscilloscope. The black curve corresponds to an unregulated step in the hotplate target temperature from 100°C to 300°C. The thermal time constant for this hotplate was assessed to be 8.1 ms. The gray line shows the same step in the target temperature, however, this time in closed-loop PID mode. As all three PID parameters and the PID sampling period are tunable, the system can be set to respond slower, with less over-swing, or even faster. A full PID controller has many advantages, such as a fast response time without over-swing and without steady state error.

9.4.1.4 Power Consumption

The power dissipation of the chip is up to 190 mW when heating all three membranes simultaneously to 350°C. The thermal efficiency of each hotplate is 6°C/mW.

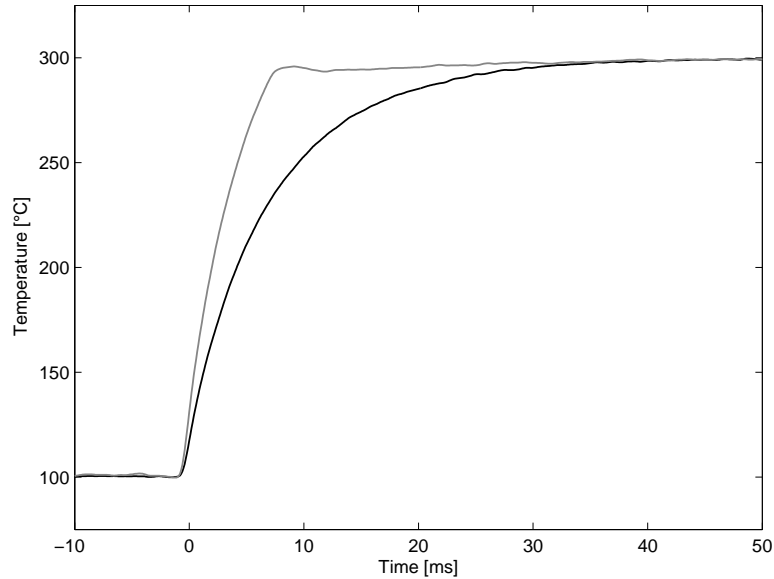


Figure 9.10: Response of the temperature sensor to a step of the target temperature. Open loop (unregulated) response is shown in black and the same step in a regulated PID mode in grey.

Table 9.1: Predicted (PLS) CO concentrations in ppm

CH ₄ \ CO	0	1	2	5	10
0		.6	2.2	5.8	8.8
100	-0.4	1.4	2.3	5.4	9.4
200	-0.4	0.9	1.7	5.5	9.6
500	0.1	1.2	1.8	5.6	9.9
1000	0.1	0.5	1.7	5.6	10.4

9.4.2 Chemical Measurements

The measured characteristics of the ADC and the current bias source result in the following specifications for the sensor readout. When applying the largest bias current to measure a small resistance, the smallest resolvable value is 11 Ω . Resistances larger than 6 k Ω can be measured with a relative accuracy of better than 99.8 %, see 9.4.1.2. The largest measurable value is 12 M Ω , when the internal bandgap reference is used. If larger values need to be measured, an external voltage reference can be used to extend the range to 50 M Ω .

Chemical measurements with different concentrations of carbon monoxide (CO) and methane (CH₄) in humidified synthetic air have been performed to evaluate the performance of the gas sensor system. The measurements were carried out using a custom-designed gas manifold [Graf et al., 2004b,a]. Figure 9.11 shows the variation of the sensor resistance during measurements with each hotplate being operated at a constant temperature. The respective gas concentrations have been applied for a duration of 20 minutes alternated with purging with pure

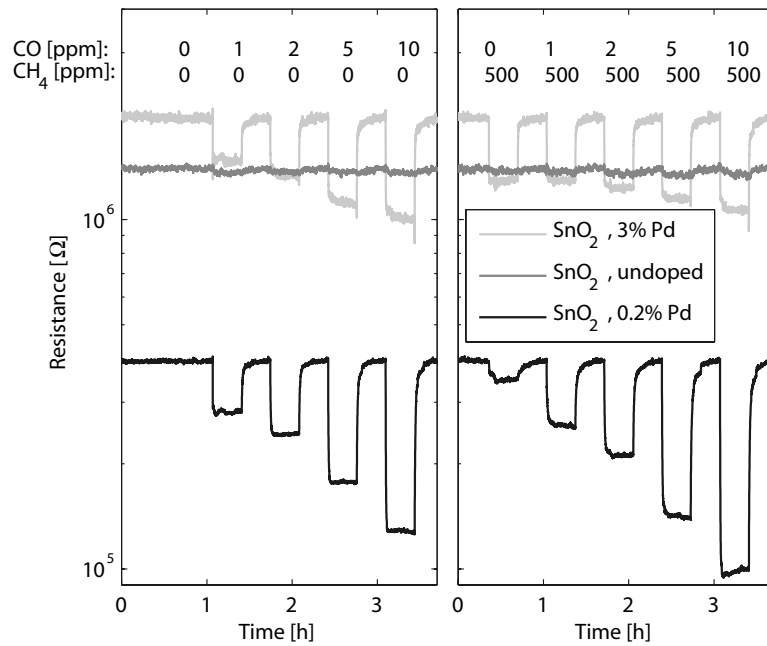


Figure 9.11: Measurements of different concentrations of pure CO and CO mixed with 500 ppm CH_4 , at 20% relative humidity. All sensors were operated at constant temperature.

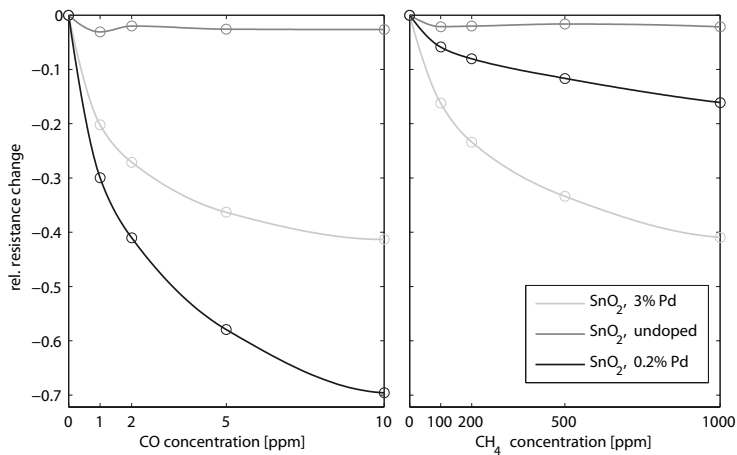


Figure 9.12: Relative resistance change versus concentration.

Table 9.2: Predicted (PLS) CH_4 concentrations in ppm

$\text{CH}_4 \backslash \text{CO}$	0	1	2	5	10
0	0	0	-50	0	30
100	140	170	80	150	50
200	170	170	210	230	230
500	450	390	540	520	590
1000	1070	1070	900	970	900

air. CO has been dosed at concentrations of 1 ppm, 2 ppm, 5 ppm and 10 ppm, the CH₄ concentrations included 100 ppm, 200 ppm, 500 ppm and 1000 ppm. The exposures to 500 ppm CH₄ are displayed on the left side of Figure 9.11. The light gray line is the sensor response of a heavily doped (3 wt% Pd) SnO₂ sensor, operated at 330°C and predominantly sensitive to CH₄. The dark gray line represents an undoped SnO₂ sensor, operated at 300°C, which is sensitive to NO₂ and, therefore, does not show any significant response upon exposure to CO or methane. The sensor response plotted in black originates from SnO₂ doped with 0.2 wt% palladium, and operated at 300°C, which is sensitive to CO and CH₄. Figure 9.12 displays a different subset of the same measurements and shows the relative resistance changes upon exposure to different concentrations of a single gas. Again, the undoped sensor shows nearly no resistance change, whereas the other two show prototypical responses of SnO₂-based sensors upon exposure to reducing gases (CH₄ and CO): the resistance drops as soon as detectable gas concentrations are applied.

The raw sensor data of the measurement shown in Figure 9.11 feature a rms noise of around 1%, which is slightly depending on the absolute resistance (1.5% at 1.1 MΩ, 1% at 550 kΩ and 0.9% at 200 kΩ). Converting the noise value into gas concentrations and multiplying it by three leads to a first-order approximation of the limit of detection (LOD) of less than 0.5 ppm for CO and approximately 100 ppm for CH₄. Comparing this noise levels to the noise level that an externally connected resistor shows (corrected by a factor of $\sqrt{2}$ to account for the elevated temperature of approximately 300°C of the hotplate), reveals that the chemoresistor shows some substantial additional flicker noise components coming from the semiconducting sensor material.

Table 9.1 and 9.2 show the predicted gas concentrations for mixtures of CO and CH₄, resulting from a partial-least-squares (PLS) regression [Wold, 1982] on the sensor data. Before applying the regression algorithm the data were preprocessed using a differential baseline removal algorithm and by applying a linear fit to the plateau value during gas exposure. To cope with the nonlinearity of the data, the quadratic term of the zero-order coefficient was added to the input as described in [Mitrovics et al., 1995]. A leave-one-out cross validation using Haaland's criterion [Haaland and Thomas, 1988] revealed that the optimum can be achieved using five factors resulting in a standard error of prediction of 0.8 ppm for CO and 105 ppm for CH₄. As the standard error of prediction suggests, the predictions shown in the tables correlate well to the true concentrations.

In a second measurement series the temperature of the hotplates was modulated as a ramp from 25°C to 350°C. Each gas exposure of 30 minutes is followed by 30 minutes purging with pure air. The temperature of the hotplates is kept at room temperature for the first 10 minutes of a cycle. Then, a period of 3 minutes at 350°C followed by another interval of 3 minutes at room temperature precedes the actual measurement, which is a 3 minute ramp from 25°C to 350°C that has been repeated twice. Close-ups of the sensor responses to synthetic air and two

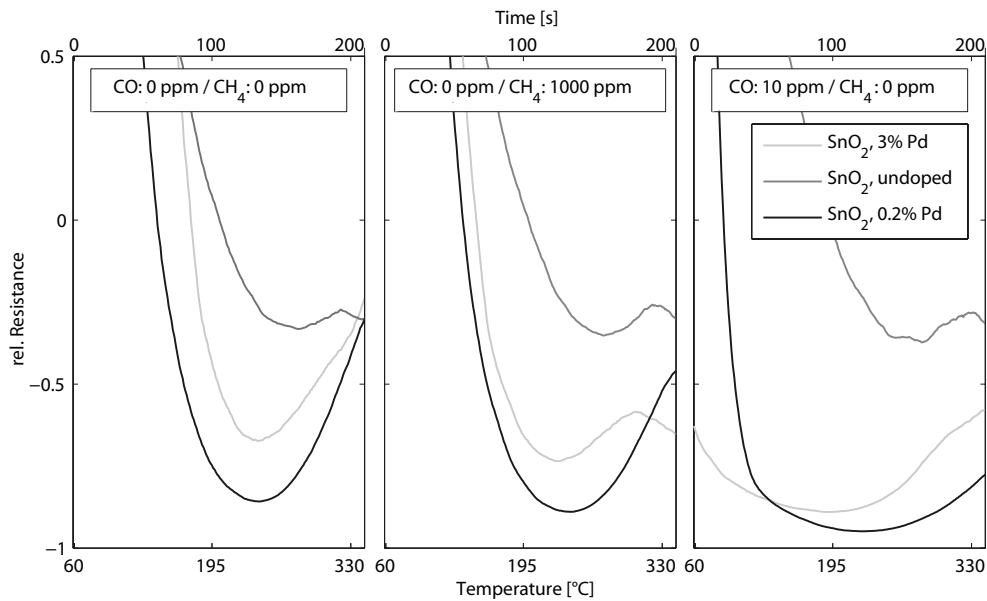


Figure 9.13: Measurements of two different concentrations of CO and CH₄ at 20% relative humidity using a temperature modulation technique.

different gas concentrations recorded during the temperature ramp between 60°C and 340°C are shown in Figure 9.13. The relative resistances with regard to the baseline resistance are plotted versus time. The sensor response of the undoped material plotted in dark gray does not show any significant variation, as this sensor is mostly sensitive to NO₂ and does not respond to carbon monoxide or methane. The two other sensors respond with very distinct patterns, e.g., the local maximum at around 300°C of the highly doped material shown in light gray is very typical for exposure to methane. It can also be seen, that methane produces a strong sensor response primarily at higher temperatures, whereas carbon monoxide already has a strong effect at low temperatures. As the time constant of the chemical reaction with the sensing material is rather large, the applied temperature profile also influences the sensor response. The additional information obtained by dynamic temperature modulations can hence be used to improve analyte classification and quantification in, e.g., mixtures [Gutierrez-Osuna et al., 2003, Heilig et al., 1997, Ionescu et al., 2002, Nakata et al., 2002, Lee and Reedy, 1999]. An accurate temperature control without steady state errors, as it is provided by a PID controller, is mandatory for applying these operation modes.

9.4.3 Summary

The device performance and the measurement results of the gas sensor system are summarized in Table 9.3.

Table 9.3: Performance summary

Technology	0.6 μm 2-P 3-M CMOS
Area	5.5 x 4.5 mm ²
Supply voltage	5.0 V
Clock frequency	1 MHz
Sensor material	SnO ₂ doped with Pd
Hotplate temperature	Room T to 350°C
Thermal time constant	8.1 ms (uncoated)
Thermal efficiency	6°C/mW
PID max. sampling rate	9.3 kSamples/s
ADC INL	± 1.5 LSB
Temperature resolution	$\pm 1^\circ\text{C}$
Measurable range	3 k Ω to 12 M Ω
LOD CO	<1 ppm
LOD CH ₄	~ 100 ppm

9.5 Conclusion

A monolithic gas sensor system was presented that comprises an array of transistor-heated microhotplates, along with digitally implemented temperature controllers, and a standard serial interface. The gas sensor system features a high sampling rate of 9.3 kSamples/s, a temperature resolution of $\pm 1^\circ\text{C}$ and a large measurable resistance range, which results in very accurate gas concentration measurements with a limit of detection of less than 1 ppm for CO and approximately 100 ppm for CH₄. Due to its integrated interface, due to the possibility to apply arbitrary temperature modulation patterns, and due to its low power consumption, the system presented here provides the technology platform for future low-cost, portable gas sensor systems. The chip can also be used for materials science, e.g., for the investigation of the electrical and gas sensing properties of different materials in dependence of the operation temperature.

Acknowledgment

The authors thank Prof. H. Baltes for sharing laboratory resources and for his ongoing stimulating interest in their work. The authors would like to thank AppliedSensor (Reutlingen, Germany), namely Dr. S. Raible and Dr. J. Kappler for coating the microhotplates with SnO₂. Furthermore, Dr. P. Reichel, Dr. N. Barsan and Dr. U. Weimar at the University Tübingen are acknowledged for their support as project partners. This work has been funded in the framework of a European collaboration project by the Swiss Bundesamt für Bildung und Wissenschaft (contract number 00.0591) and the European Union (IST-2000-28452).

Chapter 10

Outlook

The central topic of this second part of the thesis was the integration of microhotplate-based metal-oxide gas sensors and associated circuitry on a single chip. Innovative microhotplate design, dedicated post-CMOS micromachining steps and novel system architectures were developed to meet this goal.

Microhotplate-based chemical sensors start to become commercially available, which indicates the success of the ongoing miniaturization of chemical sensors. The microsensor systems as presented here are the next generation of such devices. The number of possible applications in industrial, environmental and household settings is large. Examples include the integration of sensor chips in mobile systems and distributed networks to monitor concentrations of environmentally relevant gases in cities, the surveillance of domestic air quality, and the air quality control in automotive applications. The challenges on the way to commercial products include a massive cost reduction by avoiding too frequent sensor recalibrations and by increasing the sensor lifetime.

Chapter 11

Microhotplate Bibliography

- M. Y. Afridi, J. S. Suehle, M. E. Zaghoul, D. W. Berning, A. R. Hefner, R. E. Cavicchi, S. Semancik, C. B. Montgomery, and C. J. Taylor. A monolithic CMOS microhotplate-based gas sensor system. *IEEE Sensors Journal*, 2:644–655, 2002.
- D. Barrettino, M. Graf, S. Hafizovic, S. Taschini, C. Hagleitner, A. Hierlemann, and H. Baltes. A single-chip CMOS micro-hotplate array for hazardous-gas detection and material characterization. In *IEEE International Solid-State Circuits Conference: Digest of Technical Papers (ISSCC'04)*, pages 312–313 Vol.1, 2004a.
- D. Barrettino, M. Graf, M. Zimmermann, C. Hagleitner, A. Hierlemann, and H. Baltes. A smart single-chip micro-hotplate-based gas sensor system in CMOS-technology. *Analog Integrated Circuits and Signal Processing*, 39:275–287, 6 2004d.
- S. A. Bota, A. Dieguez, J.L. Merion, R. Casanova, J. Samitier, and C. Cane. A monolithic interface circuit for gas sensor arrays: Control and measurement. *Analog Integrated Circuits and Signal Processing*, 40:175–184, August 2004.
- A. Flammini, D. Marioli, and A. Taroni. A low-cost interface to high-value resistive sensors varying over a wide range. *Instrumentation and Measurement, IEEE Transactions on*, 53:1052–1056, 2004.
- M. Graf, D. Barrettino, S. Taschini, C. Hagleitner, A. Hierlemann, and H. Baltes. Metal oxide-based monolithic complementary metal oxide semiconductor gas sensor microsystem. *Anal. Chem.*, 76(15):4437–4445, 2004a.
- M. Graf, D. Barrettino, M. Zimmermann, A. Hierlemann, H. Baltes, S. Hahn, N. Barsan, and U. Weimar. CMOS monolithic metal-oxide sensor system comprising a microhotplate and associated circuitry. *IEEE Sensors Journal*, 4:9–16, 2004b.
- M. Graf, S. K. Muller, D. Barrettino, and A. Hierlemann. Transistor heater for microhotplate-based metal-oxide microsensors. *IEEE Electron Device Letters*, 26:295–297, 2005b.
- M. Graf, U. Frey, S. Taschini, and A. Hierlemann. Micro hot plate-based sensor array system for the detection of environmentally relevant gases. *Anal. Chem.*, 78(19):6801–6808, 2006.
- M. Grassi, P. Malcovati, and A. Baschiroto. A 0.1integrated gas sensor interface circuit with 13+4 bit digital output. In *Solid-State Circuits Conference, 2005. ESSCIRC 2005. Proceedings of the 31st European*, pages 351–354, 2005.

- R. Gutierrez-Osuna. Pattern analysis for machine olfaction: a review. *Sensors Journal, IEEE*, 2:189–202, 2002.
- R. Gutierrez-Osuna, A. Gutierrez-Galvez, and N. Powar. Transient response analysis for temperature-modulated chemoresistors. *Sens. Actuator B-Chem.*, 93:57–66, 2003.
- D. M. Haaland and E. V. Thomas. Partial least-squares methods for spectral analyses .1. relation to other quantitative calibration methods and the extraction of qualitative information. *Anal. Chem.*, 60:1193–1202, 1988.
- A. Heilig, N. Barsan, U. Weimar, M. Schweizer-Berberich, J. W. Gardner, and W. Gopel. Gas identification by modulating temperatures of SnO₂-based thick film sensors. *Sensors and Actuators B: Chemical*, 43:45–51, 9 1997.
- A. Hierlemann and H. Baltes. Cmos-based chemical microsensors. *Analyst*, 128:15–28, 2003.
- E.L. Hines, P. Boilot, J.W. Gardner, and M.A. Gongora. Pattern Analysis for Electronic Noses. In *Handbook of Machine Olfaction*, pages 133–160. Wiley-VCH, Weinheim, Germany, 2003.
- R. Ionescu, E. Llobet, X. Vilanova, J. Brezmes, J. E. Sueiras, J. Calderer, and X. Correig. Quantitative analysis of no₂ in the presence of co using a single tungsten oxide semiconductor sensor and dynamic signal processing. *Analyst*, 127:1237–1246, 2002.
- J. Janata. *Principles of Chemical Sensors*. Springer, Aug 1989.
- A. P. Lee and B. J. Reedy. Temperature modulation in semiconductor gas sensing. *Sens. Actuator B-Chem.*, 60:35–42, 1999.
- J. Mitrovics, U. Weimar, and W. Gopel. Linearisation in Multicomponent Analysis Based on a Hybrid Sensor-array with 19 Sensor Elements. In *Solid-State Sensors and Actuators, 1995 and Eurosensors IX. Transducers '95. The 8th International Conference on*, volume 1, pages 707–710, 1995.
- S. Nakata, T. Hashimoto, and H. Okunishi. Evaluation of the responses of a semiconductor gas sensor to gaseous mixtures under the application of temperature modulation. *Analyst*, 127:1642–1648, 2002.
- S. Semancik, R. E. Cavicchi, M. C. Wheeler, J. E. Tiffany, G. E. Poirier, R. M. Walton, J. S. Suehle, B. Panchapakesan, and D. L. DeVoe. Microhotplate platforms for chemical sensor research. *Sensors and Actuators B: Chemical*, 77:579–591, 6 2001.
- I. Simon, N. Barsan, M. Bauer, and U. Weimar. Micromachined metal oxide gas sensors: opportunities to improve sensor performance. *Sensors and Actuators B: Chemical*, 73:1–26, 2 2001.
- J. S. Suehle, R. E. Cavicchi, M. Gaitan, and S. Semancik. Tin oxide gas sensor fabricated using cmos micro-hotplates and in-situ processing. *Electron Device Letters, IEEE*, 14:118–120, 1993.
- H. Wold. Soft modeling the basic design and some extensions. In *Systems under Indirect Observation*, II:1–54, 1982.
- J. Wollenstein, J. A. Plaza, C. Cane, Y. Min, H. Bottner, and H. L. Tuller. A novel single chip thin film metal oxide array. *Sensors and Actuators B: Chemical*, 93:350–355, August 2003.

Appendix A

Glossary

Abbreviations

ADC	analog-to-digital converter
AP	action potential
BMP-2	bone morphogenetic protein-2
CMOS	complementary metal oxide semiconductor
CRC	cyclic redundancy check
CSD	current source density (analysis)
DAC	digital-to-analog converter
DIV	days <i>in vitro</i>
DMA	direct memory access
DNL	differential nonlinearity
DRAM	dynamic random access memory
EAP	extracellular action potential
FF	flip-flop
FP	field potential
FPGA	field programmable gate array. Reprogrammable logic device
HD	high density
HD-MEA	high-density microelectrode array
HP	hotplate

HPF	high pass filter
I ² C	inter-IC (bus)
IBI	inter-burst interval
ICA	independent component analysis
ILP	integer linear program
INL	integral nonlinearity
LOD	limit of detection
LPF	low pass filter
LSB	least significant bit
LVDS	low-voltage differential signaling
MEA	microelectrode array
MOS	metal oxide semiconductor
NRC	neonatal rat cardiomyocytes
NRCml	NRC monolayers
NRCmt	NRC microtissues
OPAMP	operational amplifier
PC	Purkinje cells
PC	personal computer
PCB	printed circuit board
PDM	pulse-density modulation
PID	proportional-integral-derivative (controller)
PLS	partial-least-squares (regression)
PROM	programmable read only memory
RMS	root mean square $\sqrt{1/n \sum^n x_i^2}$
SAR	successive-approximation (ADC)
SEM	scanning electron microscope
SNR	signal-to-noise ratio
SRAM	static random access memory

Appendix B

Publications

Journal Papers

1. C. D. Sanchez-Bustamante, **U. Frey**, J. Kelm, A. Hierlemann, and M. Fussenegger, Modulation of Electrical Properties of Cardiomyocytes by Regulated BMP-2 Expression, *Tissue Engineering*, 2008, *in publication*, Chapter 5 on page 51.
2. S. Hafizovic, F. Heer, T. Ugniwenko, **U. Frey**, A. Blau, C. Ziegler, and A. Hierlemann, A CMOS-based microelectrode array for interaction with neuronal cultures, *Journal of Neuroscience Methods*, vol. 164, no. 1, pp. 93–106, 2007.
3. F. Heer, S. Hafizovic, T. Ugniwenko, **U. Frey**, W. Franks, E. Perriard, J. C. Perriard, A. Blau, C. Ziegler, and A. Hierlemann, Single-chip micro-electronic system to interface with living cells, *Biosens. Bioelectron.*, vol. 22, pp. 2546–2553, May 2007.
4. F. Greve, J. Lichtenberg, K.-U. Kirstein, **U. Frey**, J.-C. Perriard, and A. Hierlemann, A perforated CMOS microchip for immobilization and activity monitoring of electrogenic cells, *Journal of Micromechanics and Microengineering*, vol. 17, no. 3, pp. 462–471, 2007.
5. **U. Frey**, M. Graf, S. Taschini, K.-U. Kirstein, and A. Hierlemann, A digital CMOS architecture for a micro-hotplate array, *IEEE J. Solid-State Circuits*, vol. 42, pp. 441–450, 2007, Chapter 9 on page 85.
6. M. Graf, **U. Frey**, S. Taschini, and A. Hierlemann, Micro hot plate-based sensor array system for the detection of environmentally relevant gases, *Anal. Chem.*, vol. 78, no. 19, pp. 6801–6808, 2006.

Journal Papers (in preparation or submitted, at the time of printing)

7. **U. Frey**, J. Sedivy, F. Heer, S. Hafizovic, K.-U. Kirstein, and A. Hierlemann, CMOS High-Density Microelectrode Array, *in preparation*, 2007, Chapter 3 on page 11.
8. **U. Frey**, U. Egert, F. Heer, S. Hafizovic, and A. Hierlemann, Recordings from Acute Cerebellar Slices with a CMOS-based Microelectrode Array, *in preparation*, 2007, Chapter 4 on page 29.

Conference Contributions

1. **U. Frey**, M. Graf, S. Taschini, K.-U. Kirstein, and A. Hierlemann, Digital Systems Architecture to Accommodate Wide Range Resistance Changes of Metal-Oxide Sensors, *in Proceedings of the IEEE Sensors Conference*, Lecce, Italy, 2008.
2. **U. Frey**, C. D. Sanchez Bustamante, J. Sedivy, J. M. Kelm, M. Fussenegger, and A. Hierlemann, CMOS-based Microelectrode Array for Gene-Function Studies, *in Proceedings of Euroensors Conference XXII*, Dresden, Germany, 2008.
3. **U. Frey**, U. Egert, J. Sedivy, F. Heer, S. Hafizovic, and A. Hierlemann, High-Resolution CMOS-based Microelectrode Array and its Application to Acute Slice Preparations, *in Proceedings of the 6th International Meeting on Substrate-Integrated Micro Electrode Arrays*, Reutlingen, Germany, 2008.
4. C. D. Sanchez Bustamante, **U. Frey**, J. M. Kelm, A. Hierlemann, and M. Fussenegger, Modulation of Cardiomyocyte Electrical Properties by Regulated BMP-2 Expression, *in Proceedings of the 6th International Meeting on Substrate-Integrated Micro Electrode Arrays*, Reutlingen, Germany, 2008.
5. A. Hierlemann, **U. Frey**, S. Hafizovic, and F. Heer, CMOS-based Bioelectronics and Microelectrode Arrays, *in Proceedings of the 6th International Meeting on Substrate-Integrated Micro Electrode Arrays*, Reutlingen, Germany, 2008.
6. **U. Frey**, J. Sedivy, F. Heer, S. Hafizovic, and A. Hierlemann, Interfacing with Neurons at High Spatiotemporal Resolution, *in Proceedings of the IEEE Sensors Conference*, Atlanta, USA, 2007.
7. J. Sedivy, **U. Frey**, F. Heer, S. Hafizovic, and A. Hierlemann, Multi-Chip High-Density Microelectrode System for Electrogenic-Cell Recording and Stimulation, *in Proceedings of the IEEE Sensors Conference*, Atlanta, USA, 2007.

8. **U. Frey**, C. Sanchez-Bustamante, T. Ugniwenko, F. Heer, J. Sedivy, S. Hafizovic, B. Roscic, M. Fussenegger, A. Blau, U. Egert, and A. Hierlemann, Cell Recordings with a CMOS High-density Microelectrode Array, in *Proceedings of the 29th Annual International Conference of the IEEE EMBS*, Lyon, France, 2007, pp. 167–170.
9. F. Heer, S. Hafizovic, T. Ugniwenko, **U. Frey**, B. Roscic, A. Blau, and A. Hierlemann, Using microelectronics technology to communicate with living cells, in *Proceedings of the 29th Annual International Conference of the IEEE EMBS*, Lyon, France, 2007, pp. 6081–6084.
10. S. Hafizovic, F. Heer, **U. Frey**, T. Ugniwenko, A. Blau, C. Ziegler, and A. Hierlemann, Bio-microelectronic information processing device consisting of natural neurons on a CMOS microsystem, in *Proceedings of Transducers 2007*, Lyon, France, 2007, pp. 1223–1226.
11. S. Hafizovic, F. Heer, **U. Frey**, T. Ugniwenko, A. Blau, C. Ziegler, and A. Hierlemann, A CMOS-based microelectrode array for information processing with natural neurons, in *Proceedings of the 3rd International IEEE EMBS Conference on Neural Engineering 2007*, Hawaii, USA, 2007, pp. 692–695.
12. S. Hafizovic, F. Heer, **U. Frey**, J. Sedivy, F. Greve, and A. Hierlemann, CMOS-based Microelectrode Arrays for Interacting with Neurons, in *Proceedings of ULIS 2007*, Leuven, Belgium, 2007, pp. 92–95.
13. **U. Frey**, F. Heer, R. Pedron, S. Hafizovic, F. Greve, J. Sedivy, K. U. Kirstein, and A. Hierlemann, An 11k-electrode 126-channel highdensity microelectrode array to interact with electrogenic cells, in *ISSCC 2007*, San Francisco, California, 2007, pp. 158–593.
14. **U. Frey**, F. Heer, R. Pedron, F. Greve, S. Hafizovic, K.-U. Kirstein, and A. Hierlemann, 11 000 electrode-, 126 channel-CMOS microelectrode array for electrogenic cells, in *MEMS 2007*, Kobe, Japan, 2007, pp. 541–544.
15. F. Greve, J. Lichtenberg, K.-U. Kirstein, **U. Frey**, and A. Hierlemann, Perforated CMOS Microchip for Cell Immobilization and Monitoring of their Electric Activity, in *Euroensors 2006*, 2006, pp. 286–287.
16. F. Heer, S. Hafizovic, W. Franks, **U. Frey**, F. Greve, A. Blau, T. Ugniwenko, C. Ziegler, and A. Hierlemann, CMOS Integrated Bidirectional 128-Electrode Array for Electrogenic Cells, in *5th International Meeting on Substrate-Integrated Micro Electrode Arrays*, Reutlingen, Germany, 2006.
17. F. Heer, S. Hafizovic, W. Franks, **U. Frey**, F. Greve, T. Ugniwenko, A. Blau, C. Ziegler, and A. Hierlemann, CMOS Integrated Bidirectional 128-Electrode Array for Electrogenic Cells, in *Abstracts of the EPFL Latsis Symposium*, Lausanne, Switzerland, 2006, pp. 87–88.

18. F. Greve, J. Lichtenberg, K. U. Kirstein, **U. Frey**, and A. Hierlemann, Perforated cmos microchip platform for immobilization and activity monitoring of electrogenic cells, in *Proceedings of Transducers 2005*, Vol 2, pp. 1745–1747.
19. M. Graf, **U. Frey**, P. Reichel, S. Taschini, N. Barsan, U. Weimar, and A. Hierlemann, Monitoring of environmentally monolithic metal-oxide relevant gases by a digital microsensor array, in *Proceedings of IEEE Sensors Conference*, 2004, pp. 776–779 vol.2.
20. **U. Frey**, M. Graf, S. Taschini, K.-U. Kirstein, C. Hagleitner, A. Hierlemann, and H. Baltes, A digital CMOS Micro-Hotplate Array for Analysis of Environmentally Relevant Gases, in *ESSCIRC 2004*, Leuven, Belgium, 2004, pp. 299–302.

Supervised Semester/Diploma/Master Theses

1. Ueli Wahlen, **U. Frey**, and A. Hierlemann, Real-Time Spike Sorting for High-Density Neuronal Recordings, *Master's Thesis, D-PHYS, ETH Zurich*, SS07.
2. David Jaeckel, **U. Frey**, and A. Hierlemann, Unsupervised Spike Sorting for High-Density Neuronal Recordings, *Semester Thesis, D-ITET, ETH Zurich*, WS06/07.
3. Stephan Senn, Stefan Berg, **U. Frey**, and A. Hierlemann, Optimization of a High Density Neurochip, *Semester Thesis, D-ITET, ETH Zurich*, SS06.
4. Urs Muller, **U. Frey**, and A. Hierlemann, Characterisation of a High Density Neurochip, *Semester Thesis, D-ITET, ETH Zurich*, WS05/06.
5. René Pedron, **U. Frey**, and A. Hierlemann, Auslese-Elektronik für High-Density Neurochip, *Diploma's Thesis, D-ITET, ETH Zurich*, WS04/05.

Patents

1. **U. Frey**, A. Hierlemann, Embedded Multiplexer for High Density Sensor Arrays, *provisional US patent, T-06-033* (7.08.2006).

Appendix C

Acknowledgements

I would like to thank Prof. Andreas Hierlemann and Prof. Henry Baltes for giving me the opportunity to pursue my PhD thesis at the Physical Electronics Laboratory (PEL). I am particularly grateful to Prof. Andreas Hierlemann for his supervision and support throughout this work. He provided a very enjoyable and fruitful atmosphere at the laboratory leaving me with a lot of freedom to try out my own ideas and visions. He provided me with many excellent opportunities to present my work and was an incredible help in proofreading my manuscripts. I thank Prof. Henry Baltes for the professional and inspiring environment and the team-oriented atmosphere he created at PEL.

I am indebted to Prof. Christopher Hierold who stepped in as my supervisor when the future of PEL was still unclear. A special thank goes to Prof. Khalil Najafi, for coming the long way from Michigan to Zurich to co-examine this thesis and for the valuable input he provided on the circuitry part of it. I am grateful to Prof. Ulrich Egert for taking the opportunity to try his acute slice preparations with our devices, for his openness in sharing his immense experience in the field of MEAs, and for his input and patience on the way to get the manuscript of Chapter 4 published.

Special thanks go to my outstanding office-mates and friends Flavio Heer and Sadik Hafizović. Without their incredible support this thesis would not have been possible. Not only did they provide me with the INPRO chip, a formidable basis to start with, but they also never got tired in helping me wherever they could. Flavio and Sadik made the last four years very inspiring and enjoyable for me, and this not only in the lab. Together, the HPT-H3 dream team reached quite some milestones and summits.

Two people merit a special thank you for their huge contributions and hard work on the HiDens project. With Jan Šedivý's endless support the realization of the HiDens system became possible. With the Neurolizer system he created the basis for many exciting experiments in the future. With her positive attitude Carlota Diaz was the best beta tester for the HiDens chip one can ever imagine, she never got tired in starting yet another culture on the chips. With her support, she is

not only responsible for what resulted in Chapter 5 of this thesis, but also for the overall success of the system.

I am very thankful to Kay-Uwe Kirstein for his introduction and support in circuit design. He was always there and never lost patience when I was struggling with Cadence or some circuitry that was behaving weird.

Many thanks go to Markus Graf who introduced me to the world of gas sensors. I could profit a lot from his professional approach and his long experience in the field. He always had time for me when I needed help with the mysterious gas measurement setup. I would like to thank Petra Kurzawski, who took over this role once Markus left and for bringing life into the group and many interesting discussions. Stefano Taschini is acknowledged for the design of the ADA chip.

Many thanks go to all the other people at PEL, who helped with, worked on or still work on the HiDens project; Frauke Greve and Donat Scheiwiller for the post-processing of the wafers, the features of which were close to the equipments limitations; Marco Ballini for helping with measurements and coding the scripting language for the Neurolizer system; Francesca Faraci for supporting our collaborators and for developing the chip database; Branka Roščić for help with the biology.

I would like to thank the students, with whom I had the pleasure to work: René Pedron for designing the front-end amplifiers; due to his careful design the first HiDens chip performed that well; Urs Muller, who worked on the characterization of the chip; Stephan Senn and Stefan Berg for their work on the amplifier stages for the redesign of the chip; David Jackel for implementing the test bench for the spike sorter and helping to improve the spike sorter performance; Ueli Wahlen for coding work on the spike sorter and other parts of the Neurolizer system.

There are also a number of people outside of PEL that contributed to this thesis. First of all, I would like to thank Prof. Axel Blau and Tanja Neumann for all their culturing work on our chips. With their long experience of neuronal cells on CMOS devices they made measurements from dissociated hippocampal neurons and from the chicken retina look like an easy task. Lotty Rietschin from Prof. Fritjof Helmchen's group at University Zurich is acknowledged for her first trials with organotypic cultures on the devices. Dominik Langer from the same group is acknowledged for shooting with a 2-photon laser on our devices. Evelyne and Prof. Jean-Claude Perriard from the Institute of Cell Biology provided neonatal cardiomyocytes. Prof. Hiroki Ueda, Rikuhiko Yamada and Genshiro Sunagawa from RIKEN, Japan, performed the first measurements outside Europe. Prof. Christian Grimm and Karina Guziewicz supported initial measurements from the retina. Klaus Marquardt from the EMZ, University of Zurich, prepared the samples for the SEM and took the SEM pictures of the DRG neurons on the HiDens chip. Patrick Reichel from the University of Tübingen, Andreas Krauss from AppliedSensor GmbH, and Javier Las Heras Saunders from Dragados Industrial struggled together with me in the last months of the ADA project to succeed in the final review meeting of this European project.

The team at the Honggerberg workshop fabricated many black boxes and other pieces for the project.

A few others that have not been mentioned so far helped in creating an enjoyable office atmosphere during the last years at Honggerberg: Peter Friedli, Beat Hofstetter, Patrick Nuesch, Jorg Rothe and Roger Ulrich.

I also would like to acknowledge those, who kept the administrative and technical parts of the PEL-machinery running: Erna Hug, Yelena von Allmen, Christoph Kolb and Igor Levak. Thanks to all the other PELers who supported me in one way or the other: Diego Barrettino, Wendy Franks, Nils Godecke, Christoph Hagleitner, Adrian Kummer, Yue Li, Jan Lichtenberg, Tomi Salo, Jurg Schwizer, Wan Ho Song, Ralf Streichan, Robert Sunier, Cyril Vancura, Tobias Vancura, Tormod Volden, and Martin Zimmermann.

This work has been financially supported by the European Union in the framework of the ADA project (IST-2000-28452) and by ETH Zurich (internal grant TH-1-03-1).

Although not directly in the laboratory, the most important support has always come from my family and friends. Thank you Adrian and Samuel for listening, thank you Gerda and Lukas for making this possible, thank you Asako for always being there.

Curriculum Vitae

Urs Frey

Born May 27, 1977, Wetzikon, Switzerland

Swiss Citizen

- Oct. 2007 Defense of the dissertation entitled *High-Density Neural Interface and Microhotplate Gas Sensor in CMOS Technology*.
- 2002 - present Work on Ph.D. thesis and related topics at the Physical Electronics Laboratory, ETH Zurich, under the supervision of Prof. Dr. Andreas Hierlemann.
- March 2003 Degree in Electrical Engineering from ETH Zurich, Switzerland.
- 2002 - 2003 Diploma Thesis at the Laboratory of Computer Engineering TIK, ETH Zurich, entitled *Topology and position estimation in Bluetooth mobile ad-hoc networks*.
- 2001 Internship at Japan Gas Turbine, Kobe, Japan.
- 1998 - 2003 Studies at the *Department of Information Technology and Electrical Engineering*, ETH Zurich, Switzerland.
- 1992 - 1997 Gymnasium KZO Wetzikon, Switzerland, Typus C (Science).